Computational Biomechanics of Acute Myocardial Infarction and its Treatment

Mazin Salaheldin Sirry

Thesis Presented for the Degree of

DOCTOR OF PHILOSOPHY

in the Department of Surgery

UNIVERSITY OF CAPE TOWN

November 2014

Declaration

I, MAZIN SALAHELDIN SIRRY, hereby declare that the work, on which this thesis is based, is my original work (except where acknowledgements indicate otherwise) and that neither the whole work nor any part of it has been, is being or is to be submitted for another degree in this or any other university. I authorise the University to reproduce for the purpose of research either the whole or any portion of the contents in any manner whatsoever.

Signed by candidate

Signature Removed

Signature

26/11/2014

Date

Acknowledgement

"*No! Worship Allah and be among the thankful.*" (Surat az-Zumar; 66)

First and foremost, I would like to thank ALLAH for his endless mercy, blessings and gifts. I thank him for the grace of life and health. I thank ALLAH for the grace of successfully completing this thesis.

My sincere gratitude goes to my supervisors, A/Professor Thomas Franz and A/Professor Neil Davies, for their continuous support, inspiration and involvement. Thank you for the consistent guidance and encouragement throughout my doctoral journey; I was so lucky to have both of you on board.

I own my gratitude to my beloved wife, Sakna, for patience and overwhelming care. This achievement is also yours. It would not have completed without your presence and encouragement. I am also heartily grateful to my dearest parents, Salah and Entisar for their continuous prayers, support and love.

I also thank my colleagues at the Cardiovascular Research Unit; Dr Karen Kadner, Dr Laura Dubuis and Mrs Helen Ilsley for the exceptional help. Many thanks for all what you taught me.

I would like to thank Dr. Jun Liao for giving me the opportunity to visit his lab at Mississippi State University and for his kindness and endless support. I would also extend my sincere gratitude to my colleagues at Mississippi State University; Sourav Patnaik, Bryn Brazile and Robbin Bertucci, for their unlimited help and support. Thanks for making my stay in Starkville an unforgettable experience. I also extend my appreciation to the great team at the College of Veterinary Medicine; Dr Ryan Butler, Dr Andrew Claude, Dr Ron McLaughlin, Mrs. Nancy Pounds and Mrs. Jamie Walker, for their great assistance.

My sincere appreciation goes to the University of Medical Sciences and Technology, Khartoum, Sudan, my home institute. Thanks for your support.

This thesis was financially supported through the CSIR Centre for High Performance Computing, the South African National Research Foundation, and the South African Medical Research Council.

Abstract

The intramyocardial injection of biomaterials is an emerging therapy for myocardial infarction. Computational methods can help to study the mechanical effects of biomaterial injectates on the infarcted hearts and can contribute to advance and optimise the concept of this therapy.

The distribution of polyethylene glycol hydrogel injectate delivered immediately after the infarct induction was studied using rat infarct model. A micro-structural three-dimensional geometrical model of the entire injectate was reconstructed from histological micrographs. The model provides a realistic representation of biomaterial injectates in computational models at macroscopic and microscopic level.

Biaxial and compression mechanical testing was conducted for healing rat myocardial infarcted tissue at immediate (0 day), 7, 14 and 28 days after infarction onset. Infarcts were found to be mechanically anisotropic with the tissue being stiffer in circumferential direction than in longitudinal direction. The 0, 7, 14 and 28 days infarcts showed 443, 670, 857 and 1218 kPa circumferential tensile moduli. The 28 day infarct group showed a significantly higher compressive modulus compared to the other infarct groups ($p= 0.0055$, 0.028, and 0.018 for 0, 7 and 14 days groups). The biaxial mechanical data were utilized to establish material constitutive models of rat healing infarcts. Finite element models and genetic algorithms were employed to identify the parameters of Fung orthotropic hyperelastic strain energy function for the healing infarcts. The provided infarct mechanical data and the identified constitutive parameters offer a platform for investigations of mechanical aspects of myocardial infarction and therapies in the rat, an experimental model extensively used in the development of infarct therapies.

Micro-structurally detailed finite element model of a hydrogel injectate in an infarct was developed to provide an insight into the micromechanics of a hydrogel injectate and infarct during the diastolic filling. The injectate caused the end-diastolic fibre stresses in the infarct zone to decrease from 22.1 to 7.7 kPa in the 7 day infarct and from 35.7 to 9.7 kPa in the 28 day infarct. This stress

reduction effect declined as the stiffness of the biomaterial increased. It is suggested that the gel works as a force attenuating system through micromechanical mechanisms reducing the force acting on tissue layers during the passive diastolic dilation of the left ventricle and thus reducing the stress induced in these tissue layers.

Contents

List of Figures

List of tables

Nomenclature

AHA	American Heart Association
ANOVA	Analysis of variances
AV	Atrioventricular
b_{ijkl}	Dimensionless symmetric fourth-order tensor of Fung material parameters
C3D20H	Quadratic hexahedral full-integration hybrid elements
C3D20RH	Quadratic hexahedral reduced-integration hybrid elements
C3D4H	Linear tetrahedral reduced-integration hybrid elements
C3D8H	Linear hexahedral full-integration hybrid elements
C3D8RH	Linear hexahedral reduced-integration hybrid elements
CMR	Cardiac magnetic resonance imaging
Const-1	Constraint 1
Const-2	Constraint 2
CPU	Central processing unit
CVD	Cardiovascular diseases
c	Stress scaling factor
c_{10}	Neo-Hookean material parameter
d	Day
DMSO	Dimethyl sulfoxide
DTT	Dithiothreitol
E	Element
ECG	Electrocardiogram
ED	End-diastolic
EDPVR	End-diastolic pressure volume relationship
Eq.	Equation
ES	End-systolic
ESPVR	End-systolic pressure volume relationship
$\bar{\varepsilon}_{ij}^{G}$, $\bar{\varepsilon}_{kl}^{G}$	Modified Green strain tensor
E_{xx}	Nodal circumferential strain (Chapter 5)
E_{xx}	Block circumferential strain (Chapter 6)
E_{xy}	Block circumferential-radial shear strain
E_{xz}	Block circumferential-longitudinal shear strain
E_{yx}	Block radial-circumferential shear strain

E_{yy}	Nodal longitudinal strain (Chapter 5)
E_{yy}	Block radial strain (Chapter 6)
E_{yz}	Block radial-longitudinal shear strain
E_{zx}	Block longitudinal-circumferential shear strain
E_{zy}	Block longitudinal-radial shear strain
E_{zz}	Block longitudinal strain
F	Fibre layer
FE	Finite element
f_x	Circumferential force
f_y	Longitudinal force
G	Gel
G03	Soft gel
G20	Stiff gel
GA	Genetic algorithm
HIV	Human immunodeficiency virus
I	Infarct
iPBS	Iso-osmotic phosphate buffered saline
$\bar{I}_1$	First invariant of the left Cauchy-Green deformation tensor
k_G	Gel stiffness
k_I	Infarct stiffness
l	Sample length
LAD	Left anterior descending coronary artery
LCx	Left circumflex coronary artery
LSD	Least square deviation
LV	Left ventricle
M3060	30:60 N/m biaxial tension model
M6030	60:30 N/m biaxial tension model
M6060	60:60 N/m biaxial tension model
MAPE	Mean absolute percentage error
MI	Myocardial infarction
MRI	Magnetic resonance imaging
n	Total numbr
OBJ	Objective function
p	Statistical significance
PBS	Phosphate buffered saline
PCI	Percutaneous coronary intervention
PEG	Polyethylene glycol
SD	Standard deviation
S_{cmp}	Computational stresses
S_{exp}	Experimental stress
S_{xx}	Circumferential stress
S_{yy}	Longitudinal stress
TB	Tuberculosis

T	Sample thickness
t	Data point
V_{Inject}	Volume of the reconstructed injectate geometry
VS	Vinyl sulfone
V_{Wall}	Wall volume of original cardiac geometry
$V_{Wall,adj}$	Wall volume of the adjusted cardiac geometry
W	Strain energy function
Δu	Change in nodal circumferential displacement
Δv	Change in nodal longitudinal displacement
Δx	Change in nodal circumferential coordinates (Chapter 5)
Δx	Block circumferential surface displacement (Chapter 6)
Δy	Change in nodal longitudinal coordinates (Chapter 5)
Δy	Block radial surface displacement (Chapter 6)
Δz	Block longitudinal surface displacement
0d	Zero day, immediate
14d	14 days
7d	7 days
28d	28 days
2D	Two-dimensional
3D	Three-dimensional

1 Introduction

1.1 Problem identification

Cardiovascular diseases (CVD) will become the leading cause of death by 2020 superseding infectious diseases such as HIV, TB, and Malaria. Worldwide and particularly in Africa, the improvement of economic and social level has been ranked to be a major cause of increasing the risk of CVD (Steyn et al. 2005). Myocardial infarction (MI) is the most common cause of heart failure (AHA 2008; Rosamond et al. 2008). Despite the currently available therapies, the mortality from heart failure is still large (McMurray and Pfeffer 2005). This condition demands urgent alternative therapies.

The only efficacious treatment currently available is heart transplantation, which however suffers from a chronic shortage of organ donations. Considerable investigations have been dedicated towards developing new treatments with an emphasis on cell delivery approaches (Fuchs et al. 2001; Mangi et al. 2003; Zisch et al. 2003). These studies showed promising outcomes, yet the best cell type for myocardium repair is still debatable. Furthermore, the factors causing the improvement of the left ventricle (LV) pumping function after cell delivery treatments are still not clear. It is not well understood whether this beneficial effect of cell delivery treatment has been a result of a) cellular signalling, causing myocardial regeneration, neovascularisation (Fuchs et al. 2001) or decreased apoptosis (Mangi et al. 2003), b) the mechanical consequence of increasing the LV wall thickness (Grossman et al. 1975; Wall et al. 2006), or c) a combination of both cellular and mechanical mechanisms. It has been recently shown that injectable non-contractile biomaterials may be required for long-term beneficial effects on limiting infarct expansion and preventing heart remodelling (Christman and Lee 2006; Dobner et al. 2009; Ifkovits et al. 2010). These research findings emphasized acellular biomaterial injectates as a potential therapy for MI. However, more investigations are demanded to understand the impact of these injectates on the heart mechanics aiming at therapy optimization.

The effects of particular mechanical properties of the infarct zone on the ventricular performance are different during systole and diastole: a compliant infarct zone impairs systolic ejection as it is stretched during systole thereby dissipating work of the non-infarcted myocardium and reducing the ventricular pump function (Laird and Vellekoop 1977; Bogen et al. 1980). In contrast, a very stiff infarct region may impair the diastolic filling process, by increasing the overall ventricular stiffness (Smith et al. 1974), but has little adverse effects on systolic function (Bogen et al. 1980). These mechanisms also apply when a biomaterial is injected into the infarcted myocardium. The infarct zone is mechanically supported and the structural stiffness of the infarct zone is increased by the additional material and the increased wall thickness. The increased wall thickness will lead to a beneficial reduction of wall stress and the increased stiffness of infarct zone will not adversely affect the systolic ventricular function. The increased infarct stiffness may, however, impair diastolic filling and have a counteractive effect on the desired improvement of ventricular performance.

1.2 Aim and objectives

The aim of this research is the contribution to the understanding and advancement of the emerging therapies for acute MI based on the injection of biomaterials into the ischemic myocardium, by way of studying the biomechanical mechanisms associated with this treatment.

The main objectives of this study are:

1) To establish adequate computational models to simulate myocardial and ventricular mechanics.
2) To investigate the in vivo intramyocardial three-dimensional (3D) microstructural spatial distribution of polymeric biomaterial injectate and utilize this geometric information in computational models.
3) To establish constitutive models for infarcted myocardial tissue through biaxial mechanical testing.
4) To computationally simulate the regional micromechanics of myocardium with interlaced polymeric biomaterial with particular reference to the infarct zone.
5) To computationally investigate novel concepts for material-injection based MI therapy and preventive interventions for heart failure with regard to the biomechanical effects of biomaterial injection, and predict their influence on treatment outcomes.

1.3 Chapters overview

The following chapters of this thesis comprise the following:

Chapter 2 explores the relevant literature in the area of MI biomechanics. Basic cardiac mechanical and electrophysiological characteristics are addressed focusing on MI and injectable therapeutic biomaterials. Insights into mechanical characterization and computational modelling of myocardium are also presented. The chapter concludes with an overview of the established animal models for MI studies.

Chapter 3 presents the approach used to develop a geometrical heart model incorporating the in vivo intramyocardial microscopic 3D hydrogel injectate. The 3D model of the hydrogel injectate was developed from histological micrographs of an explanted rat heart. A biventricular rat heart model was developed from cardiac magnetic resonance imaging data. The two models were combined providing realistic geometries for multiscale computational studies.

Chapter 4 describes the investigation of the passive mechanical properties of infarcted tissue under biaxial compression and shear loadings. MI was induced in rat hearts and followed by mechanical testing at different time points after infarct induction. Histological analysis was performed to confirm the infarcts and to quantify their sizes. Biaxial, shear and compression results were presented and analysed. The variation in the mechanical properties of infarcts at different time points was discussed.

Chapter 5 describes the inverse modelling technique and the developed optimisation loops used to identify the constants of Fung-orthotropic constitutive model for different infarcts groups. A computational model of the biaxial test was developed and verified. Computational results were fitted to experimental biaxial data described in Chapter 4. Genetic Algorithms were utilized to optimise and search for the best fit.

Chapter 6 covers the investigation of the micromechanics of the hydrogel injectate in the infarct zone utilizing a microscopic geometry of the hydrogel (developed using the method presented in Chapter 3) and the infarct material models identified in Chapter 5. An end-systolic LV model was developed and used to simulate passive filling of a healthy LV. The mechanics of a small anterior wall volume, referred to as block, containing composites of infarcted myocardium and hydrogel injectate was captured and analysed. Results were analysed and the mutual mechanical impact between infarct and gel of varying stiffness was discussed.

Chapter 7 describes the overall findings and conclusions. Recommendations for future work were presented.

1.4 Publications originating from this PhD research

Chapter 3 represents an extended edition of the following journal paper:

- **Sirry MS**, NH Davies, K Kadner, L Dubuis, MG Saleh, EM Meintjes, BS Spottiswoode, P Zilla, T Franz. Micro-structurally detailed model of a therapeutic hydrogel injectate in a rat biventricular cardiac geometry for computational simulations. Computer Methods in Biomechanics and Biomedical Engineering, 2015. 18(3): p. 325-31.

The following peer-reviewed abstracts are also direct outcomes of this thesis and have been presented at local and international conferences:

- **Sirry MS**, Davies NH, Kadner K, Saleh MG, Spottiswoode BS, Meintjes EM, Masithulela F, Zilla P, Franz T. Geometrical Modeling of Myocardial Biomaterial Injectate in a Rat Heart Utilizing Magnetic Resonance Imaging and Histology, in 8th South African Conference on Computational and Applied Mechanics (SACAM). 3rd-5th September 2012: Johannesburg, South Africa.
- **Sirry MS**, Butler JR, Patnaik SS, Brazile B, Bertucci R, Claude A, McLaughlin R, Davies NH, Liao J, Franz T. Post-infarct Mechanical Behaviour of Rat Myocardial Tissue under Biaxial Tension, Compression and Shear Loads, in 7th World Congress of Biomechanics. 6th-11th July 2014: Boston, MA, USA.

2 Literature review

2.1 Anatomy and physiology of the heart

The heart is a hollow muscular organ specialized in pumping the blood throughout the body. It lies in the chest between the lungs. Anteriorly, the heart is supported by the ribs and sternum. The thoracic vertebrae and the diaphragm represent the posterior and inferior boundaries, respectively, of the heart. The aorta, pulmonary trunk and superior vena cava maintain the heart superiorly (Moses et al. 2005).

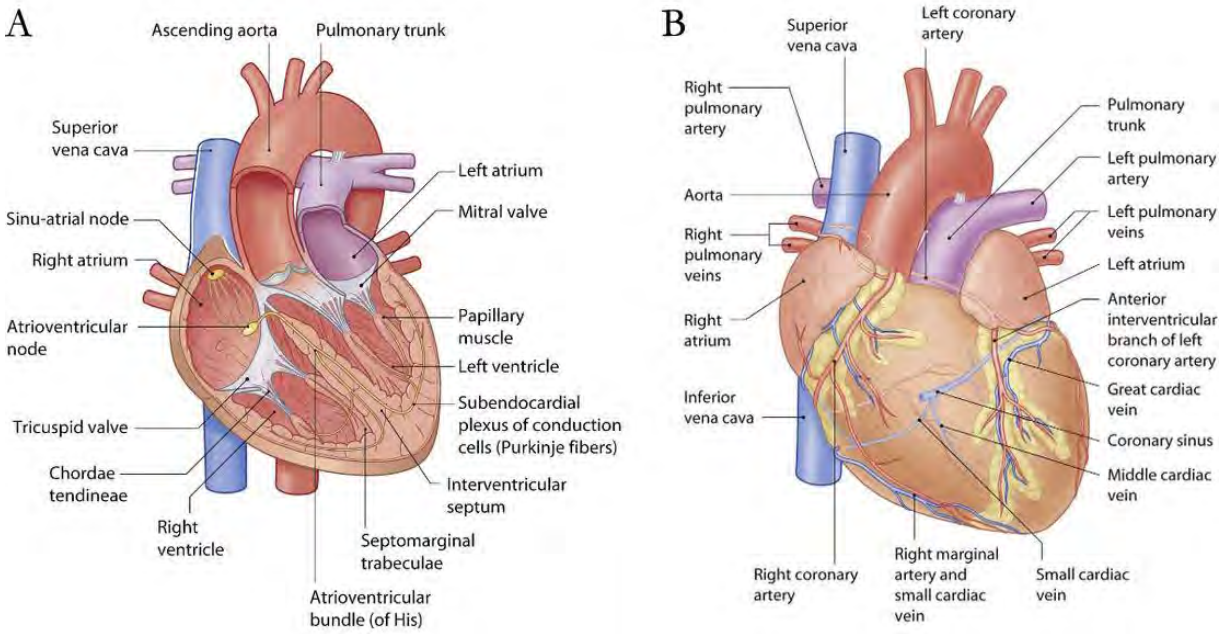

Figure 2.1: Anatomy of the heart. (a) The four chambers of the heart and the great vessels. (b) Coronary arteries and veins. (modified from Moses et al. (2005))

Internally, the heart contains four chambers as illustrated in Figure 2.1 (a). During ventricular resting state (diastole), the right atrium collects the deoxygenated blood from the body via the superior and inferior vena cava while the left atrium collects the oxygenated blood from the lungs. From the atria, the blood flows into the ventricles via two atrioventricular valves; the mitral and

tricuspid valves. During ventricular contraction (systole) the blood is pumped from the right and left ventricles to the lungs and entire body, respectively.

The cardiac tissue is supplied by blood through a set of small arteries called the coronary arteries, Figure 2.1 (b). The left and right coronary arteries originate from the left and right coronary sinuses of the aorta, respectively. The left coronary artery divides into the anterior interventricular branch, widely known as the left anterior descending (LAD), and the circumflex branch. The LAD supplies the anterior wall and the apex of the heart and the anterior two-thirds of the septum (Moses et al. 2005).

The heart wall consists of three major layers; the pericardium (outer layer), the myocardium (middle layer) and the endocardium (inner layer) as shown in Figure 2.2. The myocardium is a thick layer that contains the contracting cardiac muscle tissue and is thus considered to be the functional layer of the heart wall. The thickness of this layer varies in the heart depending on the required blood ejecting power. Therefore, the left ventricle (LV) comprises the thickest myocardium since it pumps the blood to the entire body (Van De Graaff 2001).

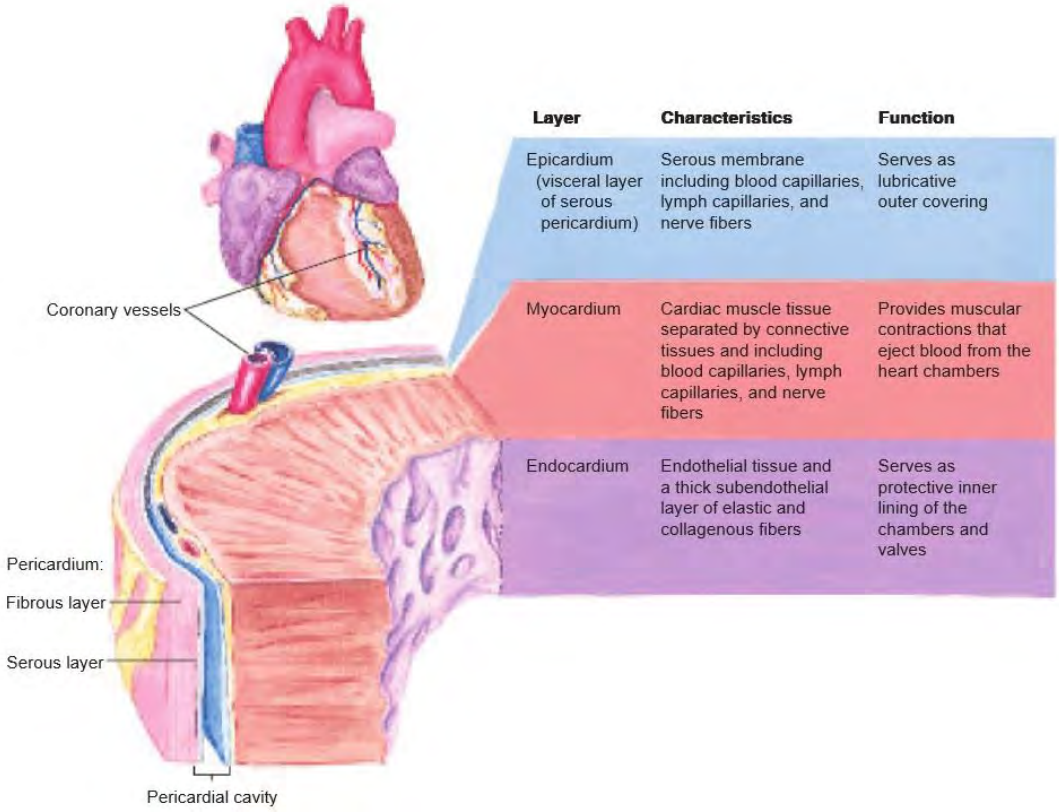

Figure 2.2: Layers of the heart wall (Van De Graaff 2001).

The cardiac muscle cells (myocytes) and fibres (myofibres) interconnect in parallel and series in a unique fashion unlike other skeletal muscle fibres. This interconnection improves the distribution efficiency of the action potential throughout the heart (Guyton and Hall 2006).

The cardiac myofibres have a very complex orientation. The fibres exhibit a global helical orientation, Figure 2.3 (a). Moreover, the fibres are arranged in sheets of different fibre orientation across the heart wall, Figure 2.3 (b). This complex orientation of fibres is believed to play an important role in the pumping function of the heart by reducing the energy required for pumping (Grosberg et al. 2009).

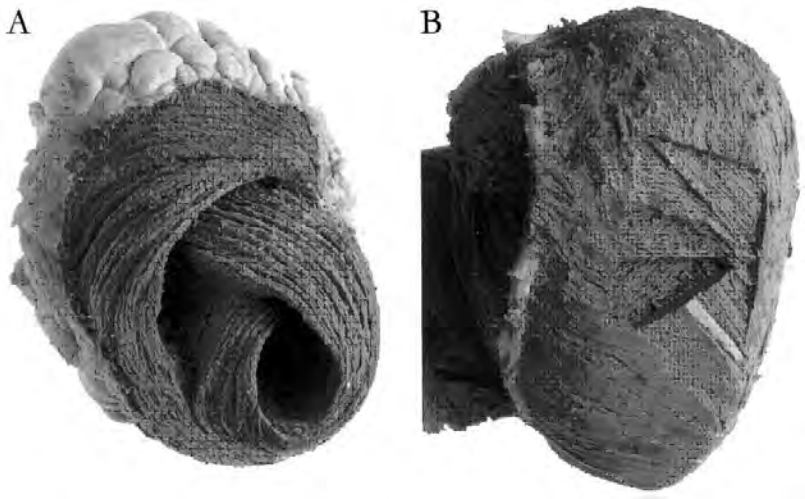

Figure 2.3: Cardiac muscle fibres. (a) Biventricular muscle fibres seen from the apex after removal of the most apical parts of the myocardial mass. (b) Free wall of the left ventricle partially fenestrated to show the continuous turn of muscle sheets. (modified from Schmid et al. (1997))

The cardiac muscle can be divided into three types: atrial muscle, ventricular muscle and specialized excitatory and conductive muscle fibres. The atrial and ventricular muscle fibres contract in similar way as the skeletal muscle except for their relatively longer contraction duration. The excitatory and conductive muscle fibres have a week contraction; however, they exhibit automatic induction/conduction of action potentials controlling the rhythmical beating of the heart (Guyton and Hall 2006).

The cardiac cycle consists of two major phases: a muscle relaxation phase called diastole and a muscle contraction phase called systole. In a cardiac cycle, a spontaneous action potential is generated at the sinus node at the lateral wall of the right atrium. The action potential is propagated over the atria inducing atrial contraction. It travels through the specialized conductive fibres, the atrioventricular (AV) bundle, to the ventricles inducing ventricle contraction. A delay of 0.1 second is presented between the atrial and ventricular contractions. This delay allows the atria to contract first and pump the blood into the ventricles which, in turn, pump the blood to the vascular system

(Guyton and Hall 2006). As a result of these cardiac events, the pressure and volume change continuously during a cardiac cycle. Figure 2.4 illustrates the cardiac cycle and the accompanying cardiac events.

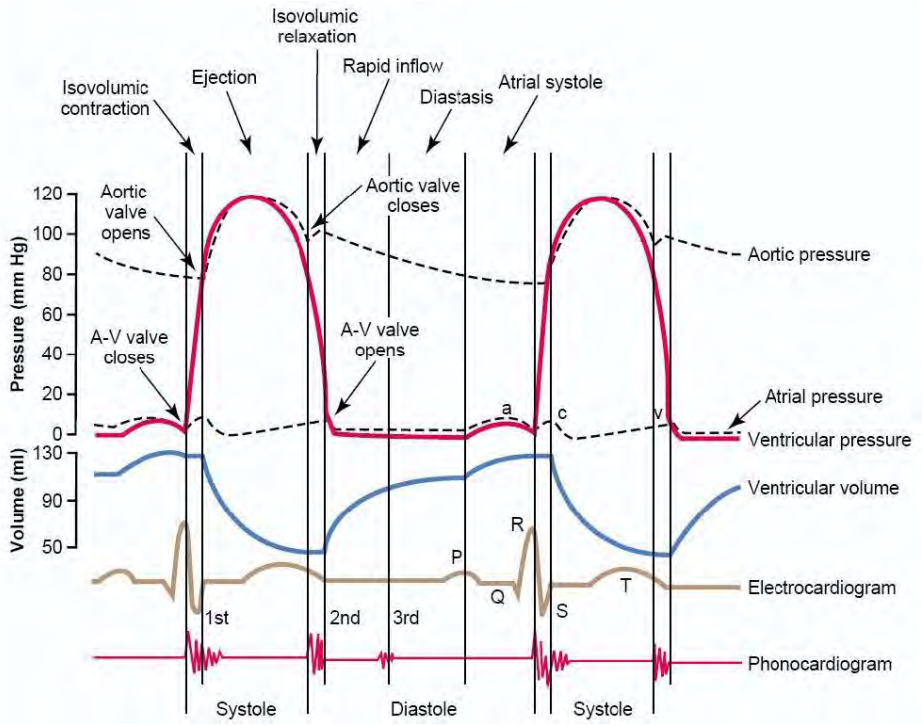

Figure 2.4: The cardiac cycle for the left ventricle (Guyton and Hall 2006).

The continuous loop of blood filling (diastole) and ejection (systole) by the LV is often represented by plotting an instantaneous pressure-volume relationship. A typical LV pressure-volume loop is shown in Figure 2.5. Following the ejection of the blood, the intraventricular pressure drops instantaneously as the ventricle relaxes (isovolumetric relaxation) until it reaches a level where the atrial pressure becomes higher. This pressure difference causes the atrioventricular valve to open allowing the blood to flow from the atrium to the ventricle (filling). The ventricular filling is associated with the increase in the ventricular volume. The ventricle then contracts and the intraventricular pressure increases instantaneously (isovolumetric contraction) causing the aortic valve to open. After that, the ventricle volume decreases as the blood is pumped into the aorta (ejection) (Burkhoff et al. 2005; Guyton and Hall 2006).

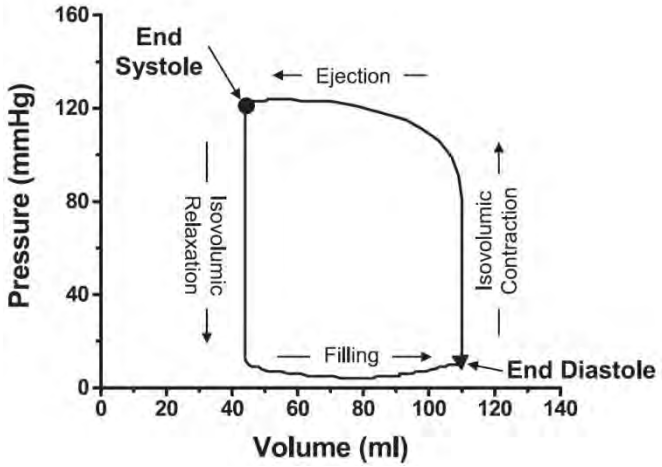

Figure 2.5: Pressure-volume loop in left ventricle (Burkhoff et al. 2005).

2.2 Pathophysiology of myocardial infarction

Myocardial infarction (MI), commonly known as "heart attack" is defined as the "complete occlusion (blockage) of coronary artery that deprives the myocardium of oxygen and causes death (infarction) of the tissue" (Moses et al. 2005). Occlusion can occur in any of the three major channels of the coronary artery or their branches. The size of the blocked vessel and the position of occlusion determines the severity of the MI from mild, moderate or severe. Obstruction of the left coronary artery before it branches is considered to cause the most serious MI since it affects the anterior, left side and a considerable portion of the posterior wall of the heart. The blockage of the LAD, which comes second in severity, damages the anterior wall of the heart as shown in Figure 2.6.

The complete or partial occlusion of coronary artery occurs by blood clots. Atherosclerosis is a known arterial disease causing hardening of the artery due to plaques (cholesterol deposits) formation in the vessel wall. The sudden rupture of the covering of the plaques trigger platelet aggregation which, in turn, leads to the formation of blood clots. As a consequence, these blood clots obstruct the lumen of the artery inducing acute MI. The main risk factors for atherosclerosis and MI include the blood lipid abnormalities (cholesterol and triglycerides), smoking and hypertension. The presence of these three factors together in one person increases the risk of having MI by tenfold. Other risk factors include family history of atherosclerosis or blood lipid abnormalities, male gender, women's postmenopausal state, diabetes, excess weight, physical inactivity, age and insulin resistance (Fuster et al. 2011).

Possible short-term consequences of MI (Turner 2008) include ventricular fibrillation, cardiogenic shock and heart block. Ventricular fibrillation occurs when the infarcted muscle interrupts the

propagation of the electrical signal causing a disorganization of the heart rhythm. This can impair the heart ability to pump the blood. Cardiogenic shock is the condition when the infarct is so massive that the remaining cardiac muscle is not able to pump the blood. The LV is prone to pump failure once the area of infarct zone reaches 40% of the LV myocardium (Page et al. 1971; Alonso et al. 1973). Heart block occurs when the damaged muscle is in the channel that carries the heartbeat signal resulting in impairing the rhythmical beating of the ventricles.

The infarcted myocardium heals by formation of scar tissue which in turn expands with time. As the heart continues to pump, the non-contractile scar tissue stretches passively. The LV wall tends to undergo structural changes that lead to dilation, Figure 2.6, and increase in ventricular volume and pressure. This long term consequence is called ventricular remodelling, a condition that can lead to a heart failure (Turner 2008). More details on remodelling are presented in the following section.

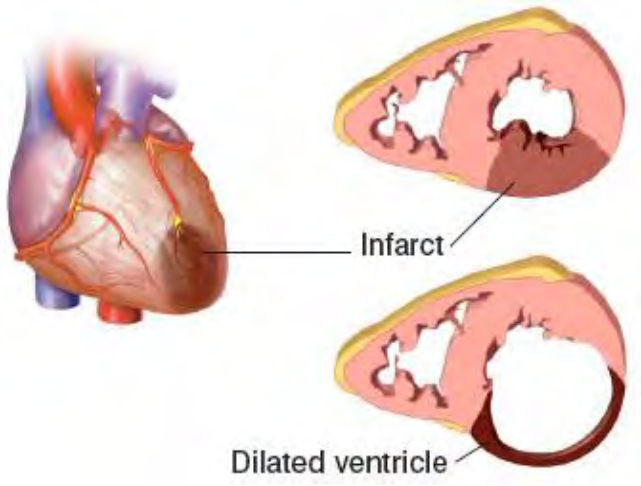

Figure 2.6: Left ventricle remodelling. © 2007 Terese Winslow

2.3 Biomechanics of myocardial infarction and ventricular remodelling

Healing and ventricular remodelling after MI are dynamic and concurrent processes (Jugdutt et al. 1996). During the first hours after myocyte necrosis in the ischemic myocardium, oedema and inflammation are limited to the infarct region (Pfeffer and Braunwald 1990). This is followed by scar formation i.e. fibroblast proliferation and collagen deposition; a process completed after weeks to months depending on the species, e.g. 3 weeks in rat (Hochman and Bulkley 1982; Roberts et al. 1983; Pfeffer et al. 1991) and 6 weeks in dog (Jugdutt and Amy 1986). During this period, the infarcted myocardium can thin and elongate - the process of infarct expansion (Hutchins and Bulkley 1978) - which occurs typically prior to the extensive deposition of collagen

with an associated increase in tensile stiffness. Thinning of the myocardium is a result of slippage between myofibre bundles (Weisman and Healy 1987). The disrupted muscle bundles are subsequently connected by connective tissue forming within the vacated myocyte compartments, thereby reducing further expansion (Vracko et al. 1989).

With the aim of providing a basis to the systematic development of MI therapies based on the understanding of the mechanical mechanisms involved, Holmes and colleagues presented a description of the mechanics of healing myocardial infarcts (Holmes et al. 2005) and distinguished four stages of myocardial infarction: i) Acute ischemia (first minutes to hours after infarction), ii) Necrotic phase (hours to 5-7 days after infarction), iii) Fibrotic phase (5-7 days to 14-28 days after infarction), and iv) Remodelling phase (14-28 days to 28-56 days after infarction). Figure 2.7 illustrates the variation in the time points of these stages between species.

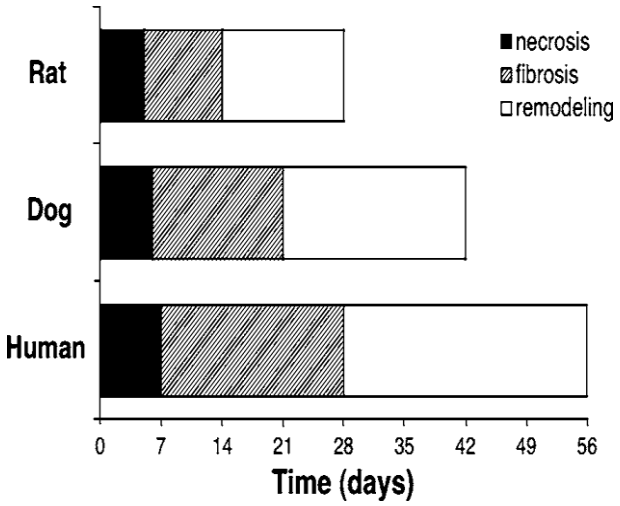

Figure 2.7: Temporal span of the phases of healing of myocardial infarction in species (Holmes et al. 2005).

The principal effects of the mechanical properties of infarcted myocardium on the LV function are the following (Holmes et al. 2005):

- **Rupture of infarcted myocardium:** Infarct rupture presents the most catastrophic failure associated with MI and accounts for 15-30% of deaths during the first post-infarction week (Birnbaum et al. 2003; Wehrens and Doevendans 2004). The mechanical properties related with infarct rupture are not fully understood (Holmes et al. 2005).
- **Stretching and bulging of the infarct zone dissipates energy generated by the non-infarcted myocardium:** The LV is prone to pump failure once the area of infarct zone reaches 40% of the LV myocardium (Page et al. 1971; Alonso et al. 1973). This has been attributed not only to a reduction of contractile myocardium that contributes to ejection

but also to a systolic impairment related to the compliance of the infarcted zone. While a stiff infarct has little adverse effects on systolic ejection(Bogen et al. 1980), systolic dysfunction is prominent for compliant infarct zones that are stretched during systole thereby dissipating work of the remaining non-infarcted myocardium and reducing the ventricular pump function (Laird and Vellekoop 1977; Bogen et al. 1980).

- **Increased stiffness of infarcted myocardium may limit the function of non-infarcted myocardium during diastole:** A very stiff infarct region is reported to impair a) the diastolic filling process by increasing the overall ventricular stiffness (Smith et al. 1974) and b) the utilization of the Frank-Starling mechanism by the non-infarcted myocardium to adjust the ventricular output (Janz and Waldron 1978). Frank-Starling mechanism is the mechanism by which the heart increases its stroke volume (blood volume pumped from ventricles in a beat) through rising the contraction energy as a result to the increase in the end-diastolic volume (Levick 2010).
- **Expansion of infarct zone and dilation of ventricular cavity leads to elevated wall stress throughout the ventricle:** The expansion, and associated thinning, of the infarcted myocardium has a two-fold effect. The thinning leads to an increase of stress in the infarcted wall at any given ventricular pressure. The increase in the ventricular volume due to infarct expansion results in an additional increase in wall stress not only in the infarct zone but also in the non-infarcted myocardium which is required to generate higher wall stresses to maintain the ventricular pump function (Weisman and Healy 1987; Bogaert et al. 2000).
- **Increased infarct stiffness limits the deformation of the functional border zone:** In the description of mechanical effects of an infarct above, distinctions with respect to myocardial regions and mechanical properties have been binary between: a) infarcted and non-infarcted myocardium and b) stiff and compliant infarcted myocardium. As to structural properties, healing infarcted myocardium exhibits mechanical anisotropy (Gupta et al. 1994; Holmes et al. 1997). On a smaller spatial scale of the infarcted LV, the distinction of myocardial regions need to be extended by introducing a so-called "functional border zone" at the junction of infarcted and non-infarcted myocardium. The functional border zone is characterized by impaired deformation despite normal perfusion (Gallagher et al. 1986; Holmes et al. 1997).
- **Infarcted myocardium may initiate ventricular hypertrophy:** Over a longer period, MI has been described to cause, by way of ventricular remodelling, volume-overload hypertrophy in the non-infarcted myocardium characterized by wall elongation and

thinning causing a global ventricle dilation (Pfeffer and Braunwald 1990). The triggering parameters of volume-overload hypertrophy have not been fully understood (Holmes 2004) but it is assumed that the material properties of the healing infarct play a dominant role in this late process which may ultimately lead to dilated heart failure (Holmes et al. 2005).

2.4 Current and proposed therapies for acute myocardial infarction

2.4.1 Diagnosis of myocardial infarction

The immediate diagnosis of acute MI is done by electrocardiogram (ECG). ECG readings can reflect whether the entire thickness of the heart wall was damaged or only partial thickness. Pathological Q waves and ST elevation or depression are indications of MI (AHA 2005). Blood tests are performed, typically measuring levels of troponin in the blood (Antman et al. 2000), to determine the severity of the damage in the heart muscle. Other diagnostic tools include coronary angiography, computerized tomography scanning, magnetic resonance imaging and echocardiography (Turner 2008).

2.4.2 Drug therapy

Acute MI requires quick intervention since time is an essential factor in successfully preserving the cardiac muscle (Maroko et al. 1971; Turner 2008). The first line treatment for acute MI includes the administration of antiplatelet agents that dissolve blood clots (thrombolysis). Antiplatelet drugs, such as aspirin, are recommended within 30 minutes after the onset of the MI symptoms (Lassen et al. 2013). Mortality rate was found to be dramatically reduced when thrombolytic treatments were given within the first two hours (Weaver et al. 1993; Boersma et al. 1996).

Other drugs for the long-term management of MI may include nitroglycerin and beta-blockers (AHA 2005). Nitroglycerin reduces the heart stress preventing LV dilation and infarct expansion (Mahmarian et al. 1998) while beta-blockers inhibit the effect of the sympathetic nervous system reducing heart rate and blood pressure (Bates 2007) therefore reducing the cardiac workload. Angiotensin-converting enzyme inhibitors are also commonly used treatments that attenuate the LV dilation and filling pressure and thus reduce the work load (Pfeffer 1991).

2.4.3 Percutaneous coronary intervention

Percutaneous coronary intervention (PCI), or coronary angioplasty, is a common and preferred treatment for acute MI (Bates and Menees 2012). This non-surgical procedure involves

subcutaneous insertion of a deflated balloon catheter in the arterial system and guided it with x-ray to the occluded coronary artery. The balloon is inflated causing dilation of the occluded artery and restoration of the blood flow as illustrated in Figure 2.8 (a).

Balloon angioplasty is more often associated with simultaneous placement of an endovascular stent, Figure 2.8 (b), to support the artery and maintain its patency (Schmitz et al. 1996). PCI can prevent the death of the cardiac muscle if performed in a timely manner. Delayed PCI, however, can still be useful for preventing future coronary artery occlusion (Turner 2008).

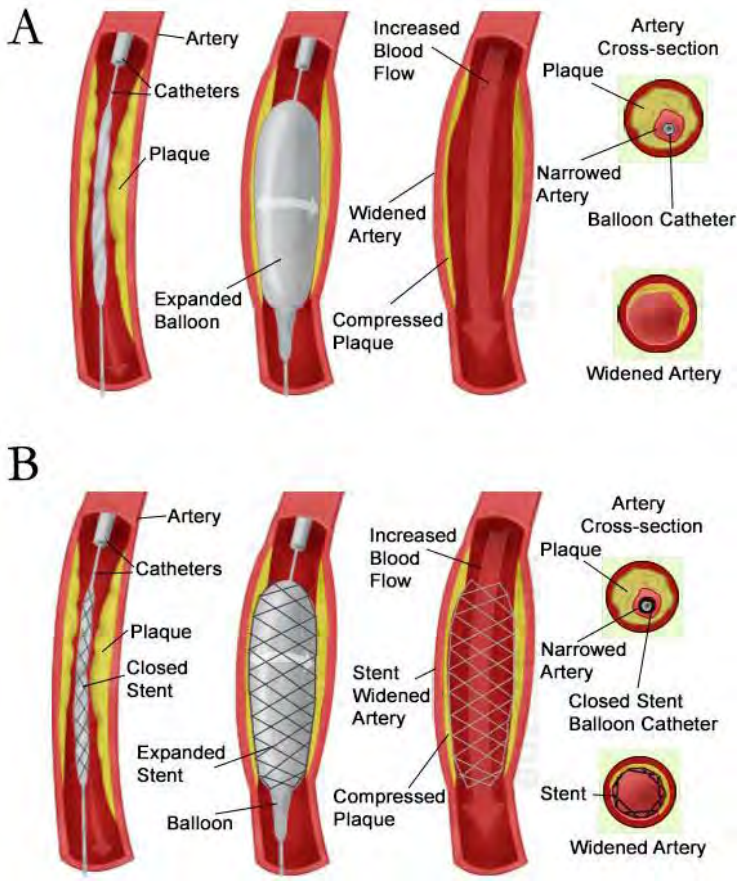

Figure 2.8: Coronary artery angioplasty. (a) Balloon angioplasty. (b) Stent angioplasty. (modified from Borade (2013))

2.4.4 Bypass surgery

Coronary artery bypass surgery is another option for managing acute MI and the atherosclerotic artery. Native veins or arteries are obtained from the patient body and utilized as grafts to bypass the diseased artery restoring the blood supply to the cardiac muscle downstream. Although bypass surgery has a great instantaneous outcome, postoperative complications are often experienced such as graft failure (Turner 2008).

2.4.5 Mechanical support devices

Late therapeutic intervention, typically greater than three hours, following acute MI may result in a complete muscle loss in the affected muscle. In this case the first line interventions are of limited benefits (Turner 2008). However, therapies are still in need to prevent or supress the complications and consequences of MI in the long term.

As mentioned earlier in this chapter, LV remodelling is one of the possible complications that can lead to a heart failure. Special devices, as shown in Figure 2.9, are utilized to provide mechanical support to the heart following MI. The reinforcement exerted by these devices is either biventricular; e.g. Acorn and Paracor devices, or applied to the LV only; e.g. Myocor myosplint. Use of these devices improves the cardiac performance and suppresses the LV remodelling. However, the supporting devices restrain the entire ventricle rather than the infarct zone only. This can interfere with the contractile tissue which can affect the pumping function of the heart (Clarke et al. 2014).

As an alternative to the whole ventricle restraints, cardiac patches were utilized to provide local support to the infarct zone. Synthetic and tissue-engineered cardiac patches (Liu et al. 2004; Rane and Christman 2011) were widely tested as local infarct restraints. In spite of the reported positive outcome, cardiac patches have the limitation of interfering with the contractile tissue at the functional border zone which influence the motion and contraction in that area (Clarke et al. 2014).

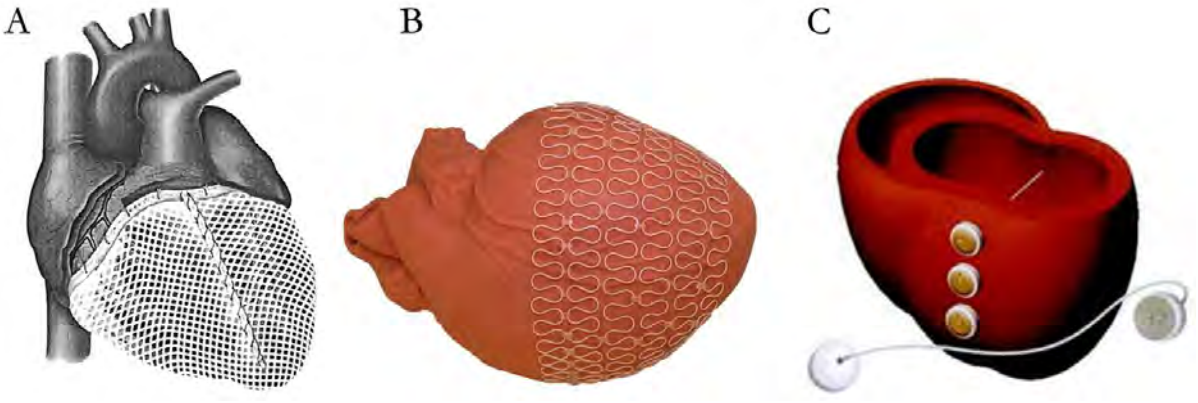

Figure 2.9: Devices used to mechanically support the heart. (a) Acorn device (Saavedra et al. 2002). (b) Paracor device (modified from Klodell Jr et al. (2008)). (c) Myocor myosplint left ventricle device (Raman 2008).

2.4.6 Cardiac transplantation

Cardiac transplantation is presently the only cure for patients with severe heart failure. However, cardiac transplantation is limited by the availability of donors, the high cost, the limited capacity of the specialized clinics and lifelong immunosuppression (Struck et al. 1985).

2.4.7 New proposed therapies

Despite the available therapies, the incidence of heart failure after MI is still high strongly indicating the need for new therapies. Aiming at restoring the contractility in the damaged tissue, pre-clinical research has been devoted to develop new treatments based on cell delivery approaches (Fuchs et al. 2001; Mangi et al. 2003; Zisch et al. 2003; Lutolf and Hubbell 2005). In general, cell therapy studies showed encouraging outcomes. However, there is uncertainty about the best cell type for myocardium repair and whether the improved LV pumping function is purely caused by the injected cell. It has been argued that such improved outcome is due to the mechanical consequence of increasing the LV wall thickness (Grossman et al. 1975; Wall et al. 2006). It has been recently shown that injectable non-contractile biomaterials may be required for long-term beneficial effects on limiting infarct expansion and preventing heart remodelling (Christman and Lee 2006; Dobner et al. 2009; Ifkovits et al. 2010). These research findings emphasized acellular biomaterial injectates as a potential therapy for MI. One major advantage of biomaterial injection therapy over restraint devices and cardiac patches is that it is less invasive and can be applied thoracoscopically or intravascularly (Nelson et al. 2011). As such, biomaterial injection is considered to be a promising new therapeutic approach for MI.

2.5 Research in biomaterials injection therapies for myocardial infarction

Biomaterial injection therapy is an emerging approach for the treatment of MI. The procedure involves injecting a biocompatible material (biomaterial) into the infarcted zone of the heart wall. The injectate provides the required mechanical reinforcement to the infarcted tissue. In addition to the mechanical support, the biomaterial injectate can achieve biological improvements when it is used as a carrier to deliver stem cells or drugs (Nelson et al. 2011). Theoretically, the biomaterial injectate can play a two-fold role in improving the heart function: (1) mechanically supporting the damaged tissue preventing remodelling, while (2) delivering growth factors and stem cells that can repair the damaged myocardium.

The early investigations of injection therapy utilized biological materials such as collagen (Dai et al. 2005), chitosan (Lu et al. 2009), fibrin (Christman et al. 2004) and alginate (Landa et al. 2008).

Synthetic materials, such as synthetic hydrogels (Dobner et al. 2009; Jiang et al. 2009), were also investigated. The advantage of using the synthetic over the biological materials is the ability to control the material properties to meet a specific requirement; e.g. biodegradability and stiffness. However, the biocompatibility of synthetic materials is challenging (Nelson et al. 2011).

Cell therapy for MI (Atkins et al. 1999; Strauer et al. 2002; Tomita et al. 2002; Kawamoto et al. 2003) has shown small but beneficial improvements in the mechanical function of the LV, in most cases independent of the cell type used. It has been hypothesized that the introduction of additional material into the infarcted myocardium exhibits beneficial effects on ventricular performance based on passive mechanical support and irrespective of cellular and/or electromechanical activity. In conjunction with the potential advantages of acellular MI therapies over cell therapy, e.g. reduced immune rejection, greater safety, reduced costs, it has been suggested that biomaterials on its own may be of great importance for future MI therapy approaches and cardiac therapy in general (Gaudette and Cohen 2006). A study of the short-term mechanisms responsible for LV post-infarct improvement after biomaterial injections into the heart was presented by Wall et al. (2006). Three different injection modes, namely single injection into anterior border zone, multiple border zone injections and single injection into the infarct zone, were investigated with various injections volumes and a range of mechanical properties of the injectable biomaterial. A three-dimensional (3D) finite element (FE) method for large elastic deformation of ventricular myocardium (Costa et al. 1996) and a constitutive model representing the passive and contractile anisotropic mechanical properties of healthy and impaired myocardium (Guccione et al. 1995) were implemented in a validated FE model previously proposed for an ovine heart by Walker et al. (2005). Biomaterial injection was represented by regional adjustment of the FE mesh to simulate local bulging and active contractility of the simulated injection site was reduced to account for non-contractility of the injected volume. The latter was only required for injections in the functional border zone whereas the infarct zone did not exhibit active contractility. The effects of the injected material on the LV mechanics was assessed by means of predictions of myocardial fibre stress and cardiac performance metrics such as end-systolic and end-diastolic pressure volume relationships (ESPVR, EDPVR), ejection fraction, stroke volume end-diastolic pressure relationship, and stroke volume end-diastolic volume relationship. This study has shown a number of important findings for acellular and cellular MI therapy approaches:

- Small amounts of injected biomaterial (0.5-5.0% of total myocardial volume) can alter cardiac mechanics, reduce wall stress and affect cardiac performance measures.

- Improvement in long-term ventricular mechanics may be achieved by passive reduction in local stress instead of adding contractile elements in the infarct zone
- Improvement of cardiac performance metrics may be superficial, due to geometrical changes associated with material injection, without a true improvement of global pump function. This is an important finding also with regard to cell therapy studies reporting on improvement of cardiac performance. Volumes injected during cell therapies have exceeded those simulated from Wall et al. (2006) and cardiac performance improvements reported may only be due to change in local ventricular geometry rather than the cell therapy. Here it is important that the performance metrics are selected, e.g. ESPVR, so as to adequately consider changes in ventricular geometry.

2.6 Myocardial infarction in animal models

Preclinical investigation of new treatments for human often involves animal models. Researchers have been using different animal models in MI and heart failure studies. Since the human is the target subject of these investigations, it is very important to select animal models whose pathophysiology is similar to human. Concurrently, economical and time consumption considerations might influence the selection of an animal model.

Large animals such as pigs have been ranked superior to small animals such as rats because of size and weight similarities between the human and pig heart particularly in extrapolating results from animal models to human (Pérez de Prado et al. 2009). However, rat heart follows the anatomy and pathophysiology of the human heart (Goldman and Raya 1995). Rats also require less laborious and surgical facilities, they are much cheaper and one can easily obtain histology samples from their relatively small hearts (Fishbein et al. 1978). Therefore many investigators have shown a great interest in using rat models for MI studies with the LAD coronary occlusion being the preferable technique to induce infarction (Fishbein et al. 1978; Zimmer et al. 1990; Goldman and Raya 1995; Crowley 1997; Wise et al. 1999; Abarbanell et al. 2010).

In connection with biomechanics, the mammalian cardiac geometry has been studied most extensively in dogs (Nielsen et al. 1991; Pao and Ritman 1998) but has also been described for other animal species such as sheep (Guccione et al. 2001; Moustakidis et al.), rabbit (Vetter and McCulloch 1998; Vetter and McCulloch 2000), and rat (Crowley 1997; Wise et al. 1999).

2.7 Computational cardiac biomechanics and electrophysiology

The primary function of the heart, pumping blood through the circulatory system, is fundamentally mechanic. The pumping cycle of the heart consists of passive (resting) and active (contracting) processes the mechanics of which is dissimilar. The cardiac biomechanics of the normal heart, and the computational methods such as the FE method, have been described at various levels from laying out the principles of continuum mechanics and electrophysiology and approaches of approximation and discretization of the underlying FE method (Usyk and McCulloch 2003; McCulloch and Paternostro 2005) to the application of these computational methods to pre-clinical and clinical questions (Vetter and McCulloch 1998; Vetter and McCulloch 2000; Bettendorff-Bakman et al. 2006; Dorri et al. 2006; Tendulkar and Harken 2006; Delhaas et al. 2008; Kroon and Holzapfel 2008). The stresses and strains in the myocardial wall play a central role in the cardiac mechanics as they affect many physiological factors such as pumping performance, myocardial oxygen demand, and coronary blood flow. The main determinants of myocardial stresses and strains are:

- The cardiac geometry, most importantly the ventricular geometry.
- The structure of myocardial tissue.
- The loading conditions (e.g. filling pressure, arterial pressure, and ventricular volume).
- The constraints or boundary conditions (e.g. pericardial and thoracic environment).
- The material properties of the myocardium (passive properties, active properties).

Loading conditions of the heart, and most importantly the LV, have been defined with circulatory models of varying complexity. The basic parameters in cardiac mechanics are blood pressure, volume and flow rate in the major cardiac chambers. From the point of myocardial wall stress and strain, ventricular pressure is most relevant. Typically, the pressure in the LV is presented either in association with the aortic pressure (constituting the LV afterload) or as ventricular pressure-volume relationship. Afterload models have often been considered in cardiac mechanics computations (Usyk et al. 2001; Usyk et al. 2002; Kerckhoffs et al. 2003; Watanabe et al. 2004). The best-known models for LV afterload are two- and three-element Windkessel models (Frank 1899; Broemser and Ranke 1930; Westerhof et al. 1973; Stergiopulos et al. 1999). The LV preload, i.e. the ventricular filling pressure, has received less attention with regards to model representations (Kerckhoffs et al. 2006) and the incorporation in computational models of cardiac mechanics (Watanabe et al. 2004).

Quantitative information on the external constraints of the heart, such as the surrounding pericardium and its attachment and effects of inspiration and expiration, are not widely reported and appropriate estimations have been employed in computational studies (Dorri et al. 2006).

Resting myocardium is often modelled as transverse-isotropic (Humphrey et al. 1990a; Humphrey et al. 1990b) finite elastic material using a hyperelastic pseudo-strain function (Fung 1993) and the assumption of incompressibility (Usyk and McCulloch 2003). Extension of transverse isotropy to material orthotropy has been reported (Usyk and McCulloch 2003). The assumption of incompressibility is reasonable for isolated myocardium but may not be sufficient for the intact heart that can exhibit considerable redistribution of myocardial tissue volume under physiological conditions associated with phasic changes in regional coronary blood supply (McCulloch 2005). For active (contractile) properties of the cardiac muscle, a number of models have been suggested which include variable elastance formulating the active cardiac force as a function of muscle length and time (Suga et al. 1973; Arts et al. 1979; Chadwick 1982; Suga 1990; Taber 1991; Kerckhoffs et al. 2007), Hill-type models in which the active fibre stress varies with shortening or lengthening (Arts et al. 1982; Nevo and Lanir 1989) and fully history-dependent models generally based on Huxley's cross-bridge theory (Panerai 1980; Landesberg and Sideman 1994a; Landesberg and Sideman 1994b; Landesberg et al. 1996). An alternative history-dependent approach is the fading memory model (Hunter et al. 1998) which exhibits less biophysical complexity than the cross-bridge models.

Comprehensive reviews of computational strategies for cardiac electrophysiology as a framework for modelling the cardiac function have been presented by Belik et al. (2004) and Kerckhoffs et al. (2006). Structurally and functionally integrated models of cardiac electromechanical functions, combining cellular system models and anatomical multiscale simulations, have received particular attention in these reviews. At cellular level, the action potential has been modelled phenomenologically, e.g. with the FitzHugh-Nagumo equations (FitzHugh 1961; Nagumo et al. 1962), or biophysically deriving from change in transmembrane ionic currents (Noble and Rudy 2001; Belik et al. 2004) most of which are based on the formulation by Hodgkin and Huxley (1952). Advanced models (Luo and Rudy 1994a; Luo and Rudy 1994b; Jafri et al. 1998; Viswanathan and Rudy 1999; Pandit et al. 2001; ten Tusscher et al. 2004; Healy and McCulloch 2005), developed for various species including rat (Pandit et al. 2001), consider transmural heterogeneity in electrophysiological properties and represent the mechanisms more realistically than Hodgkin-Huxley formulations which however comes at a larger computational expense. Tissue models of cardiac electrophysiology integrate cellular formulations into larger scale models and either treat

cells as discrete units (van Capelle and Durrer 1980; Leon and Horacek 1991) or as syncytium (Geselowitz and Miller 1983; Henriquez 1993) in mono-domain and bi-domain models; the latter of which distinguish between intracellular and extracellular space. Tissue models have been employed to study ischemia (Pandit et al. 2001). FE based implementation of the mono- and bi-domain models has not been able to capture the discontinuous nature of cardiac propagation which has been overcome using a finite volume implementation (Trew et al. 2005). Bi- and mono-domain models have been used to simulate electrophysiology at organ level, i.e. in the whole heart. Typically, simplified representations of ionic/cellular phenomena were used in whole heart models due to excessive computational demand at organ level. Rosolen et al. (2006) proposed different numerical strategies of cardiac electrophysiology based on the FE method to describe the 3D electrical propagation in realistic ventricular geometries. They utilized the FitzHugh-Nagumo model (FitzHugh 1961; Nagumo et al. 1962) and a bi-domain model. Limitations of the solutions were encountered with respect to the prediction of physiological un-realistic isotropic propagation patterns but were ascribed to the use of isotropic diffusion tensors. An integrated computational model combining electrical excitation and propagation of the myocardium with fluid-structure interaction models of the myocardium and the blood volume has been presented by Watanabe et al. (2004). Here, the FitzHugh-Nagumo model was used with a mono-domain propagation model (Hodgkin and Huxley 1990). Electrophysiology in the context of ischemia has also been investigated at organ level (Rodriguez et al. 2004).

2.8 Computational modelling of myocardial infarction and ventricular remodelling

Mazhari et al. (Mazhari et al. 1998; Mazhari and McCulloch 2000; Mazhari et al. 2000) presented a FE model to simulate LV filling and ejection and associated wall stresses in presence of myocardial infarction due to LAD and left circumflex (LCx) coronary occlusion. The geometry and myofibre orientation of the model were based on comprehensive measurements with a 3D digitizing probe on an entire explanted canine heart (Nielsen et al. 1991; Mazhari et al. 1998). The myocardial constitutive model used was based on bi-axial test data (Lin and Yin 1998). To model ischemia in the infarcted region, the intercellular calcium concentration was decreased so as to result in 50% maximum activation (Hunter et al. 1998). A stepwise transition was employed at the perfusion boundary. The numerical predicted differences in end-systolic strains and the border zone width between LAD and LCx occlusion infarcts compared well with their experimental observations (Mazhari et al. 2000).

Moustakidis et al. (2002) and Guccione et al. (2001) conducted FE simulations to study the local mechanics of the functional border zone in the infarcted LV of a sheep 10 weeks post-infarct. Geometric information of the LV shape and location of the border zone were obtained using magnetic resonance imaging (MRI) and used two-dimensionally (Moustakidis et al. 2002) and in conjunction with 3D reconstruction (Guccione et al. 2001). Moustakidis et al. (2002) measured the intracavity pressure using intraventricular Millar® catheter and utilized the measurements as loading. A nearly incompressible, linear elastic and isotropic myocardial material model was utilized. The border zone was distinguished from healthy myocardium anatomically (through varying the wall thickness) rather than functionally. The simple material model, owing to the lack of access to more refined data, was stated by the authors as a main limitation of this computational work. Guccione et al. (2001) used more advanced constitutive models distinguishing between passive (transverse isotropic strain energy potential) and active myocardial properties (cellular electrophysiological constitutive equation and time-varying elastance) and utilized the latter to simulate loading by ventricular contraction. They represented the infarction by omitting contractile tissue properties in the ischemic zone and scaled contractility from 0 to 100% in the functional border zone from infarct to non-infarcted myocardium. Comparing three different cases: a) normal border zone contractility and infarct material properties, b) reduced border zone contractility and infarct material properties, and c) reduced border zone contractility and stiffened infarct, it was concluded that the mechanical impairment of the LV infarct border zone is predominantly caused by contractile dysfunction of the myocardium rather than increased wall stresses.

A similar approach followed by Walker et al. (2005) to investigate the LV aneurisms in a sheep 22 weeks post-infarct. LV geometry and myofibre orientation were analysed with tagged MRI (with concurrent Millar® catheter intra-LV pressure measurement). The passive and contractile mechanical properties of the myocardium were modelled in a similar fashion as to Guccione et al. (2001). End-systolic and end-diastolic pressure measured intraventricularly was used to load the model after offset of the minimum LV pressure. Material properties were determined with a semi-inverse approach applying the loading to the FE model with initial material properties which were subsequently adjusted to match resulting configuration of the model with those recorded experimentally. Increases of 24% in fibre stress and 115% in cross-fibre stress in the border zone compared to remote myocardial regions were demonstrated. It was concluded that active cross-fibre stress is an integral part of the LV systolic mechanics that needs to be included in FE analyses.

Aikawa et al. (2001) presented a FE study of post-infarct LV remodelling in association with an echocardiographic clinical trial. Patient-specific (n = 64) LV geometries were pseudo-reconstructed from orthogonal echocardiographic views obtained 14 days after the myocardial infarction. For the simulations, LV end-systolic pressure loading was approximated with systolic pressure values recorded during echocardiography. Similar to the study of Moustakidis et al. (2002), myocardial material properties were represented in a very simplified fashion as homogenous, isotropic, and incompressible. It was concluded from the numerical predication that the apical LV wall stress at day 14 post-infarct can serve as predictor for LV dilation during the subsequent 11 weeks. However, the combination of the simplified 3D representation of the LV and the simplified material properties constitute the major short-coming of this study.

Wenk et al. (2011a) extended a nonlinear optimization method (Sun et al. 2009) to computationally investigate the LV contractility and the associated stress distribution in a sheep model with posterobasal MI. The LV geometry was developed from short- and long-axis tagged MRI data. The systolic circumferential strain which was calculated from the MRI images was used to determine the infarct region and approximate the border zone. Optimization of active material parameters for different regions was performed by comparing the model-predicted results to the experimentally measured values and minimizing the errors.

3 Micro-structurally detailed model of a therapeutic hydrogel injectate in a rat biventricular cardiac geometry

3.1 Introduction

In attempts to improve the understanding of the underlying mechanisms, computational models have been utilized to study the mechanical effects of injecting biomaterials into the heart. Wall et al. (2006) investigated injections into infarct zone and border zone with various injection volumes (0.5-5% of total myocardial volume) and a range of mechanical properties of the injectable biomaterial. The injectates were represented by local adjustment of the finite element mesh. This study showed that small amounts of injected biomaterial can alter cardiac mechanics, reduce wall stress and affect cardiac performance. Wenk et al. (2009) developed a method to optimize the pattern of multiple injection of a polymeric biomaterial. The results indicated an intuitive injection pattern with the greatest number of inclusions when aiming at minimising the mean end-diastolic (ED) and end-systolic (ES) myofibre stress but ignoring the LV stroke volume. A non-intuitive pattern was, however, found as optimum when both myofibre stress and stroke volume were considered. Wenk et al. (2011b) investigated the treatment of an LV infarct with the injection of a calcium hydroxyapatite-based tissue filler and demonstrated an increase of ejection fraction and a reduction of ED and ES fibre stress in the remote and infarct regions for the treated case compared to the untreated case.

These three studies demonstrated benefits that can be derived from computational models for the improvement of MI therapies utilizing myocardial injections. However, the biomaterial injectates were simulated either in a 'smearing' approach by adjusting wall thickness and constitutive properties of the region of injection but without geometrically representing the injectate (Wall et al. 2006; Wenk et al. 2011b) or in injectate patterns difficult to be achieved in vivo (Wenk et al.

2009). Kortsmit et al. (2013) implemented the discrete layer-wise configurations of the myocardial injectate in computational models to emulate, also still simplified, striated injectate distributions observed in vivo (Dobner et al. 2009; Ifkovits et al. 2010; Kadner et al. 2012).

In this chapter, the distribution of polyethylene glycol (PEG) gel injections in infarcted myocardium was investigated in a rat model. The three-dimensional (3D) geometry of the hydrogel injectate in the infarcted myocardial region of the LV was obtained using histological methods, microscopic imaging and 3D image reconstruction. Particular emphasis was placed on a high spatial resolution of the injectate to enable a realistic representation in computational models both at macroscopic and microscopic level. A rat biventricular cardiac geometry was reconstructed from cardiac magnetic resonance (CMR) image data. A combined 3D model of a rat heart with an LV biomaterial injectate was developed.

3.2 Materials and methods

3.2.1 PEG hydrogel preparation and labelling

Vinyl sulfone (VS) functionalized PEG gels (20kDa, 8arm) were manufactured as described by Dobner et al. (2009). Per gel, 1 µl of 10mg/ml Alexa Fluor® 660 C2 maleimide (Invitrogen Molecular Probes, Eugene, Oregon, USA) in dimethyl sulfoxide (DMSO, Sigma-Aldrich Chemie GmbH, Steinheim, Germany) was added to 1 µl of 15.4 mg/10 ml dithiothreitol (DTT, Sigma-Aldrich Chemie GmbH, Steinheim, Germany) in iso-osmotic phosphate buffered saline (iPBS, 0.15M, pH 7.5) and reacted for 30 min at 37ºC. Gels of 10% (m/v) nominal concentration were prepared by dissolving 10 mg of 20 PEG-8VS in 25 µl iPBS and adding 1 µl of the above Alexa/DTT solution. The pre-polymer was cross-linked with 3.45 mg MMP-1 degradable peptide (GenScript USA Inc., Piscataway, NJ, USA) in 75µl iPBS, then aspirated into a syringe and injected into the myocardium before the components were able to polymerize.

3.2.2 Induction of myocardial infarct and injection of PEG hydrogel

The animal experiments were approved by the Institutional Review Board of the University of Cape Town and performed in accordance with the National Institutes of Health (NIH, Bethesda, MD, USA) guidelines. Surgical procedures were performed according to Huang et al. (2006). In brief, male Wistar rats (180-220 g) were anaesthetized with a mix of oxygen and 5.0% Isoflurane (Safeline Pharmaceuticals (Pty) Ltd., Johannesburg, South Africa), intubated with a 16G intravenous catheter (B. Braun Melsungen AG, Melsungen, Germany) and placed onto a heated operating board (Braintree Scientific, Inc., Braintree, MA, USA). Throughout surgery the animals

were ventilated (112 breaths/min) while anaesthesia was maintained with a mix of oxygen/2.0% isoflurane. The heart was exposed via left thoracotomy performed along the 4th intercostal space. After pericardiotomy, myocardial infarction was induced by permanent ligation of the left anterior descending coronary artery with a 6-0 non-absorbable polypropylene ligature (Ethicon Inc., Somerville, NJ, USA) 3 mm distal the auricular appendix. Discolouration of the anterior ventricular wall and reduced contractility were hallmarks of a successful occlusion of the artery. Immediately after infarct induction, animals received 100 µl 20PEG-8VS cross-linked with MMP1-degradable peptide via injection into the infarcted area of the myocardium. After allowing for dispersion and in situ polymerization of the PEG gel for 30 min, animals were humanely killed. The hearts were carefully harvested and thoroughly rinsed with saline (Adcock Ingram Critical Care, Johannesburg, South Africa).

3.2.3 Tissue processing, sectioning and histological image acquisition

The hearts were mounted onto chucks and snap frozen in liquid nitrogen (Air Liquide (Pty) Ltd, Germiston, South Africa). Sectioning was performed on a cryostat (Microm, Heidelberg, Germany) from the apex towards the base of the heart, taking two adjacent 30µm sections at 20 levels with an inter-level distance of 200µm. Sections were dipped into phosphate buffered saline and mounted using DAPI mount (Vector Laboratories, Burlingame, CA, USA). Microscopic images were acquired with an Eclipse 90i Fluorescent Microscope with digital camera DXM-1200C and fluorescein isothiocyanate filter (all Nikon Corporation, Tokyo, Japan) at 3.2x magnification and stitched (NIS Elements BR 3.0, Nikon, Corporation, Tokyo, Japan) to obtain composite images of the entire short-axis cross section of the heart at each level.

3.2.4 Geometrical reconstruction of myocardial injectate

Histological images of the heart closest representing the observation in previous studies (Dobner et al. 2009; Kadner et al. 2012) were utilised for the reconstruction. Short-axis cross section composite images of 20 histological sections in cardiac longitudinal direction were imported in Adobe Photoshop CS3 (Adobe Systems Inc, San Jose, CA, USA), stacked and aligned to represent the in vivo configuration. The region containing the PEG gel was cropped in each image and the resulting image stack was imported in Simpleware (Simpleware Ltd., Exeter, UK). The appropriate in plane resolution and the section-to-section distance were defined by setting the x, y and z spacing parameters to 0.002, 0.002 and 0.245 mm, respectively. The x and y spacing values were acquired from a calibration scale image captured at 3.2x magnification whereas the z spacing value was obtained from the level distance of the cryo-sectioning process. Image noise and artefacts

were reduced using bilateral filters (width= 3 pixels in each direction, sigma range= 120). Two-dimensional (2D) spatial segmentation masks were developed for the gel injectate in the individual images using region-growing segmentation algorithms (Simpleware 2014). Through stacking of these 2D masks, a 3D geometric model of the PEG gel was developed.

3.2.5 Reconstruction of biventricular cardiac geometry

CMR image data from a healthy rat were utilized to reconstruct a 3D biventricular geometry of a rat heart. The image data was obtained in a related study (Saleh et al. 2012) using a custom built transmit-receive small-animal bird cage coil with 70 mm diameter in a 3.0T Magnetic Resonance Imaging (MRI) system (Allegra, Siemens Healthcare, Erlangen, Germany). An ED short-axis image stack was imported in Simpleware utilising the spatial parameters encoded in the CMR images. Gradient anisotropic diffusion and gradient magnitude filters were employed to reduce image noise and enhance the appearance of endocardial and epicardial edges. 2D spatial masks of the myocardium were developed using a combination of intensity thresholding and region growing segmentation algorithms. The 2D masks were stacked and the 3D biventricular end-diastolic geometry was reconstructed.

3.2.6 Combining cardiac and injectate geometries

The anterior wall of the LV of the reconstructed cardiac geometry required adjustment to simulate local wall thickening associated with the hydrogel injection. The wall thickness was increased locally by adjusting the 2D masks at the epicardium and endocardium of the LV. The overall adjusted cardiac geometry fulfilled the assumption:

$$V_{Wall,adj} \approx V_{Wall} + V_{Inject}$$

where $V_{Wall,adj}$ is the wall volume of the adjusted cardiac geometry, V_{Wall} is the wall volume of the original cardiac geometry and V_{Inject} is the volume of the reconstructed injectate geometry. Subsequently, the reconstructed injectate geometry was embedded at the predefined injection site in the anterior LV wall of the adjusted cardiac geometry.

3.3 Results

Figure 3.1 (a) shows one histological image of the cross-sectional region of the LV wall with the hydrogel injectate. Image filtering reduced artefacts and noise in the original acquired histological

micrographs, Figure 3.1 (b) and the application of the 2D spatial masks enhanced the striations of the gel injectate as shown in Figure 3.1 (c).

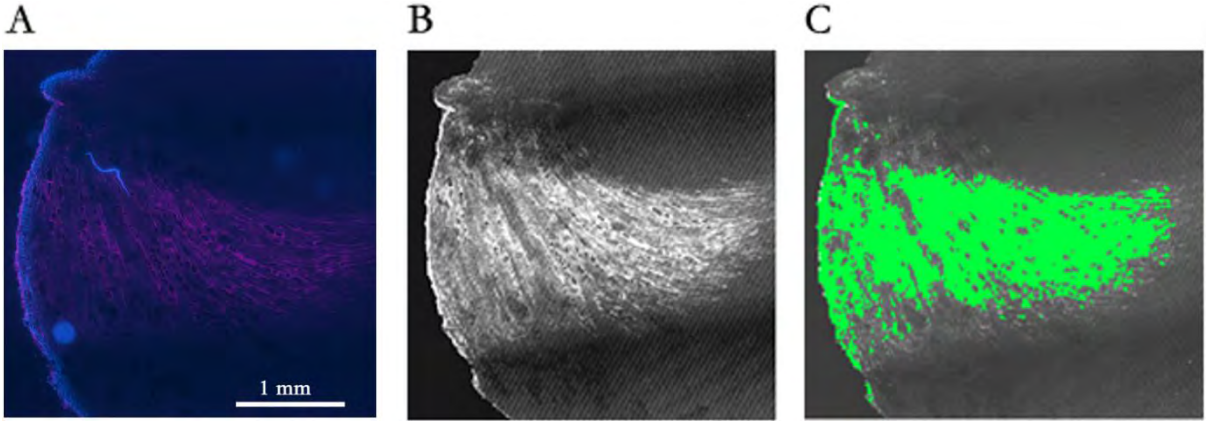

Figure 3.1: (a) Fluorescent image of the cross-sectional region of the LV wall injected with Alexa Fluor® 660 labelled hydrogel. Nuclei appear blue and hydrogel appears pink. (b) Histology image after conversion to greyscale and image filtering to reduce artefacts and noise. The hydrogel appears white. (c) Selection of the hydrogel and enhancement of the striations by means of a spatial masks appearing in green.

The injectate geometry reconstructed from a set of 20 micrographs is illustrated in Figure 3.2 (a). The microscopic structure obtained from the reconstructed geometry, Figure 3.2 (b), closely resembled the striated micro-structure of the gel injectate observed histologically in Figure 3.2 (c).

Figure 3.3 (a) shows the set of CMR images at ED time point with contour lines drawn at the epi- and endocardial surfaces of the left (green and red) and right (aqua and violet) ventricles. The stages of image processing of each short-axis CMR slice for the 3D reconstruction of the cardiac geometry are illustrated in Figure 3.3 (B-D): The original acquired CMR image, Figure 3.3 (b), underwent filtering, Figure 3.3 (c), after which a 2D spatial mask was applied, Figure 3.3 (d).

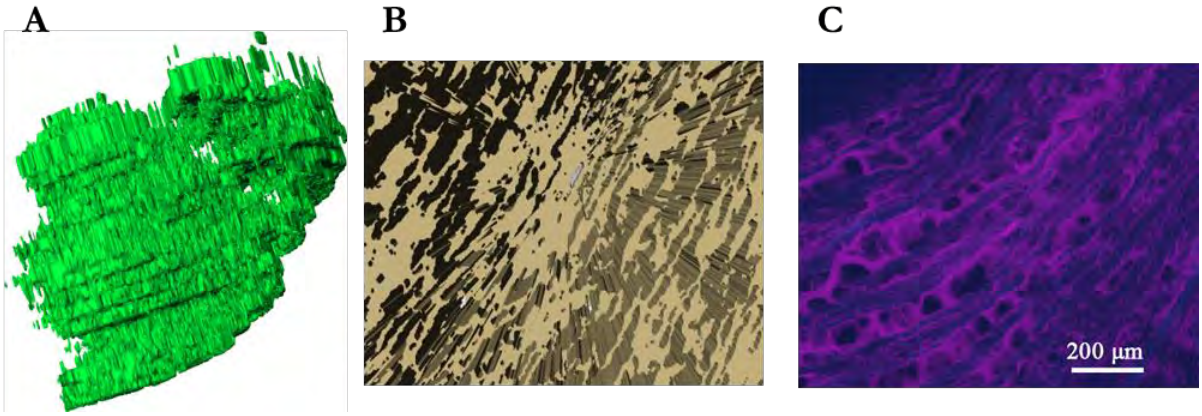

Figure 3.2: The three-dimensional reconstructed injectate geometry (a). A close-up of the injectate geometry (b) reveals that it was feasible to represent the in situ micro-structural striations of the hydrogel (c) during the reconstruction process.

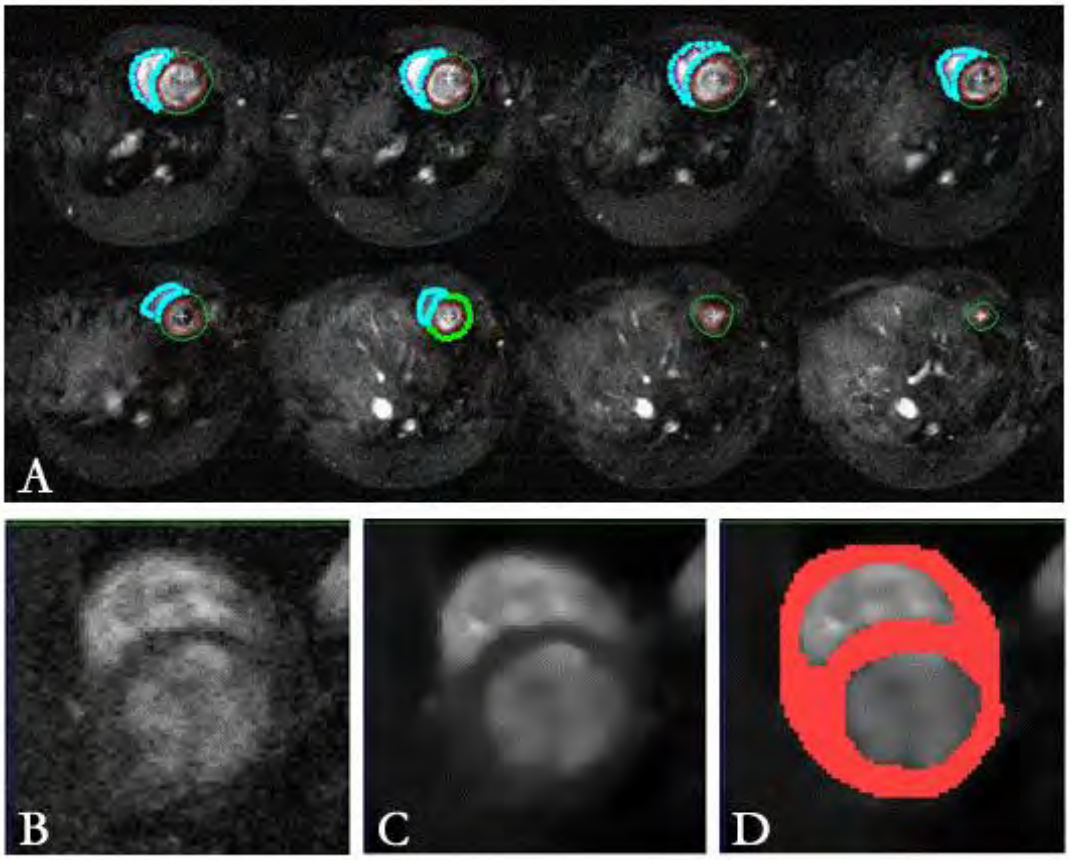

Figure 3.3: Set of eight CMR images of a rat showing short-axis views of the heart at ED time point. The epi- and endo-cardial contours are delineated in green and red, respectively, for the left ventricle and in aqua and violet, respectively, for the right ventricle (a). Close-up short-axis views of the rat heart: Original image (b), image after filtering for reduction of noise (c) and filtered image with spatial mask identifying the cardiac tissue (d).

The implementation of the LV anterior wall thickening at the site of the gel injection is illustrated in Figure 3.4. Using a 2D mask for the LV, the heart wall was adjusted locally on the epicardial and endocardial sides (see bottom part of Figure 3.4) over a distance of 5 mm along the longitudinal axis of the heart. This extension matched the in situ height of the injectate of 4.9 mm representing approximately 40% of the distance between apex and base of the rat heart.

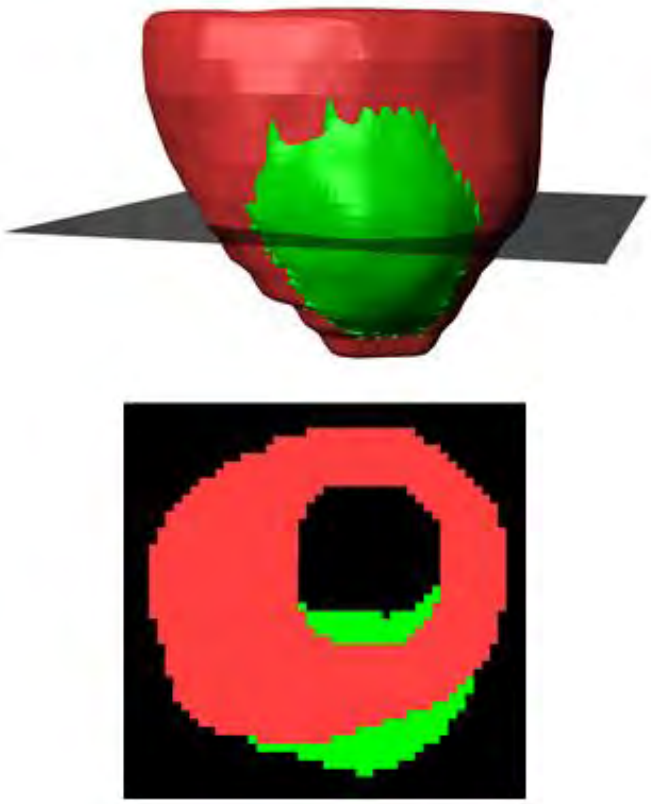

Figure 3.4: Illustration of the adjustments (in green) of the anterior wall of the reconstructed cardiac geometry (in red) to account for the myocardial injectate: The 2D spatial masks were appended locally at epicardial and endocardial sides to generate a local wall thickening.

The biventricular cardiac geometry as reconstructed from the CMR image data at ED time point is illustrated in Figure 3.5 (a). The reconstructed geometry exhibited a myocardial wall volume of 544 mm^3. The result of the local adjustments of the anterior LV wall thickness, i.e. bulging at the predefined injection site of the PEG gel, can be observed in Figure 3.5 (b). The wall thickness adjustment increased the total wall volume in the biventricular geometry to 579 mm^3. The combined model with the PEG gel geometry embedded in the cardiac geometry at the injection site is illustrated in Figure 3.5 (c).

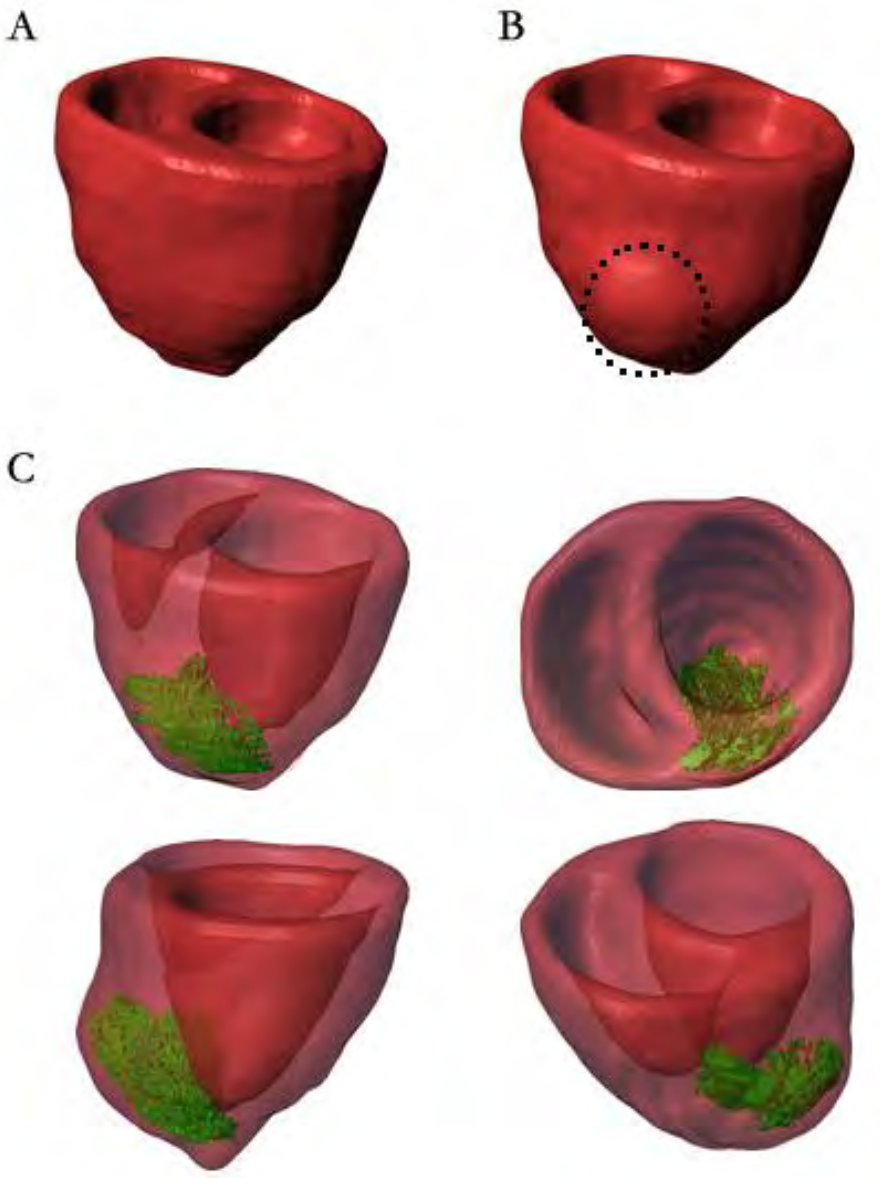

Figure 3.5: (a) 3D biventricular geometry of the rat heart reconstructed from CMR image data. (b) Biventricular cardiac geometry with local wall thickening (dotted circle) to account for the therapeutic myocardial hydrogel injectate. (c) Different views of the adjusted biventricular cardiac geometry combined with reconstructed hydrogel injectate geometry. The cardiac geometry is displayed partially translucent to for illustration purposes.

3.4 Discussion

A biventricular cardiac model of a rat heart was developed with a micro-structurally detailed geometry of a therapeutic PEG hydrogel injectate. This was achieved through combining histological analysis, CMR imaging and image-based geometrical reconstruction. The developed geometry of the PEG gel injectate captured the striated distribution of the hydrogel within the myocardium as observed in vivo in preclinical studies when the biomaterial was administered immediately after the infarction (Dobner et al. 2009; Ifkovits et al. 2010; Kadner et al. 2012). With

the simplified representation of the therapeutic myocardial injectates in previous computational studies, e.g. by homogenisation (Wall et al. 2006; Wenk et al. 2011b) and in coarse layers (Kortsmit et al. 2013), the injectate geometry reconstructed in the current study provides the basis for a more realistic implementation of intramyocardial injectates in computational models.

Due to its micro-structural details, the injectate geometry is particularly suited for the investigation of micro-mechanical interactions between injectate and myocardial tissue. At this microscopic scale, the injectate model may also offer potential for studying the mechanobiology in MI cell therapies for which the injectate provides the physical environment of the injected cells. A macroscopic model of the injectate with less micro-structural details can be obtained from the existing geometry, e.g. to study global mechanics of the heart at reduced computational expense. As such, the models can facilitate multi-scale computational studies of injectate-based MI therapies.

The infarcted rat heart from which the injectate model was developed was explanted minutes after infarct induction. Since geometrical changes were not expected in the cardiac wall during this short period of time, the geometry of the infarcted heart was assumed to be similar to that of a healthy heart. Accordingly, the biventricular cardiac geometry was developed from CMR image data obtained from a healthy rat. A local heart wall thickening (increase in wall volume) was assumed as a result of the additional injectate volume. Three-dimensional echocardiography-based models of sheep hearts demonstrated an increase in the heart wall thickness as a result of injecting hydroxyapatite-based tissue filler (Wenk et al. 2011b). For the PEG gel, it can be argued that the in vivo layered dispersion of the PEG gel will result in a volume change smaller than what was modelled in the current study. Nevertheless, local increase of the wall thickness at the epicardial and endocardial sides has been a common modelling procedure to account for the injectate volume (Kortsmit et al. 2013; Miller et al. 2013).

For the development of computational models, e.g. for finite element analysis, cardiac and injectate geometries need to be complemented with additional structural and constitutive data. Such data can be obtained from literature, such as the distribution of myofibre alignment and constitutive properties of the rat heart (Omens et al. 1991), or experimentally. The gel model is generically valid to study the mechanics associated with injecting the gel immediately after the infarction induction since it has been shown that the gel could take a different in situ distribution when injected one week after the infarction (Kadner et al. 2012). Nevertheless, the approach of developing the model could be applied to obtain a realistic geometry of the injectate under different conditions, e.g. different injection timing.

4 Mechanical characterization of infarct tissue

4.1 Introduction

The functioning of a heart following a myocardial infarction (MI) is strongly influenced by the mechanics of the infarcted tissue. Understanding the passive mechanical properties of infarcted tissue at different infarct stages is essential for improving the emerging biomaterial injection treatments for MI. Additionally, capturing the mechanical properties of infarcted tissue allows the development of constitutive models for computational studies.

The orientation of myocardial fibres causes the myocardial material to exhibit mechanical anisotropy (Bovendeerd et al. 1992). As such, uniaxial tensile testing is not sufficient in capturing the 3D constitutive behaviour of cardiac tissue even when applied individually in the principal material directions (Usyk and McCulloch 2003). Biaxial tensile testing has been commonly utilized in characterization of soft tissues; such as myocardium (Demer and Yin 1983), valve leaflets (Billiar and Sacks 2000; Grashow et al. 2006) and pericardium (Chew et al. 1986).

Demer and Yin (1983) performed biaxial and uniaxial tensile tests on left ventricle (LV) tissue of canine hearts demonstrating the anisotropy, non-linear elasticity and viscoelasticity of the passive myocardium. Anisotropy was found to be regionally dependant in this study. Novak et al. (1994) observed similar anisotropy on different regions of LV and, however, different strain-energy levels when canine heart specimens were subjected to identical biaxial loading. Sacks and Chuong (1993a; 1993b) investigated the biaxial mechanical properties of right ventricle (RV) and compared the results to those of LV. They concluded qualitative similarities and quantitative differences between the mechanics of right and left ventricles.

One of the earliest attempt to investigate the biaxial mechanical properties of infarcted myocardium was presented by Gupta et al. (1994). They induced anterioapical MI in sheep hearts

by ligating the left anterior descending (LAD) and second diagonal coronary arteries. Hearts were harvested at 4 hours, 1, 2 and 6 weeks after coronary ligation and biaxial tensile load was applied along the cardiac circumferential and longitudinal directions. Gundiah et al. (2004) also studied the biaxial mechanical properties of healing MI in sheep hearts, however, they tested the infarcts at 2 and 8 months following the infarction onset.

Rats have been widely used as animal models in research of MI biomaterial injection therapy (Landa et al. 2008; Dobner et al. 2009; Kadner et al. 2012). Yet there is only one study in literature that quantifies the passive mechanical properties of infarcted myocardial tissue of a rat heart (Fomovsky and Holmes 2010). This emphasizes the need to conduct additional studies to establish and strengthen a baseline for assessing the mechanical properties of the infarcted tissue in the context of biomaterial injection treatment.

Therefore, in this chapter the passive mechanical properties of the healing infarcts in rat hearts was investigated using multiple loading protocols. Anterioapical MI was experimentally induced through LAD coronary ligation. Infarct samples were obtained at different post-infarct time points and tested under planar biaxial tension and uniaxial compression respectively. In addition to improve the understanding of the mechanical behaviour of infarcted rat myocardium, this study aimed at providing sufficient data to develop material constants for infarcts at different healing stages.

4.2 Materials and methods

4.2.1 Myocardial infarction induction

The animal experiments were approved by the Mississippi State University Institutional Review Board and Institutional Animal Care and Use Committee and were performed in accordance with the National Institutes of Health (NIH, Bethesda, MD, USA) guidelines. Surgical procedures were performed according to Huang et al. (2006). Male Wistar rats (215-280g) were anaesthetized with a mixture of oxygen and 5.0% Isoflurane and intubated with a 16G intravenous catheter. Body temperature was maintained by placing rats on a heated operating pad. Positive-pressure ventilation was established and anaesthesia was maintained with a mix of oxygen/2.0% Isoflurane. A left thoracotomy was performed at the 4th intercostal space and ribs were retracted followed by a pericardiotomy. MI was induced by permanent ligation of LAD coronary artery with a 6-0 silk ligature 2-3 mm distal to the auricular appendix. The effectiveness of MI induction was assessed by the extent of paleness and fibrillation (uncoordinated contraction) of the myocardial tissue on

the anterior ventricular wall. Animals were euthanized by arresting the heart via intracardiac injection of saturated potassium chloride solution and hearts were harvested and fixed in 10% phosphate buffered saline (PBS).

Infarcted hearts were harvested immediately (0 day), 7, 14 and 28 days after infarct induction (n= 5, 9, 9 and 9 respectively) representing several healing stages. For the animals of 7d, 14d and 28d groups, the chest was orderly closed and the animal was given subcutaneous buprenorphine injection for postoperative pain management.

4.2.2 Heart dissection and testing sample preparation

The harvested hearts were dissected to prepare testing samples. The atria, pulmonary trunk and the free wall of the right ventricle were cut away. A longitudinal cut was made through the posterior wall of the LV from the base to apex. The LV was unfolded and a full transmural square sample (~10×10 mm) was dissected from the anterioapical region of the LV wall. All mechanical tests were carried out within 7 hours after harvesting the hearts. Samples were always kept moisturized during manipulation by continuously applying 10% PBS.

4.2.3 Biaxial tensile test

The biaxial mechanical properties of myocardial tissue samples were captured using a biaxial testing system (Grashow et al. 2006) shown in Figure 4.1 (a). The length, width and thickness of samples were measured using a Vernier calliper and recorded prior to testing. For a single sample, 3 thickness measurements were made and the average was taken. Four optical markers were glued to the epicardial surface of the sample marking a ~ 4×4 mm area in the centre. Two evenly spaced suture needles were placed on each side of the sample ~2 mm away from the edge, Figure 4.1 (b and c).

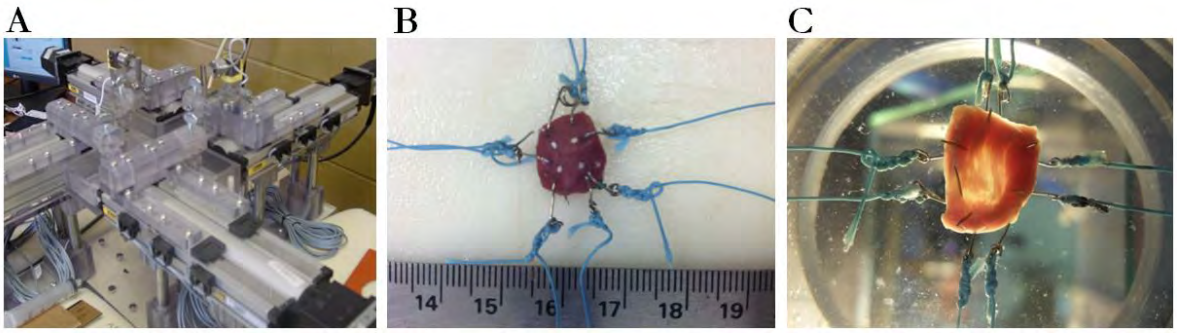

Figure 4.1: (a) Biaxial testing rig. (b) Tissue sample with four optical markers glued to the epicardial surface. Eight suture needles were placed in the sample. (c) Tissue sample mounted in the biaxial during testing.

All biaxial tests were performed with tissue samples completely submerged in 37°c 10% PBS. Biaxial tensile load was applied along the cardiac circumferential and longitudinal directions of the sample at 0.5 mm/s. Following 10 preconditioning cycles of 30 N/m (force per unit length of the sample) equibiaxial tension, three loading protocols were applied (circumferential:longitudinal N/m) as illustrated in Figure 4.2:

- Equibiaxial tension: 60:60 N/m (Protocol 1).
- Non-equibiaxial tension: 30:60 N/m (Protocol 2).
- Non-equibiaxial tension: 60:30 N/m (Protocol 3).

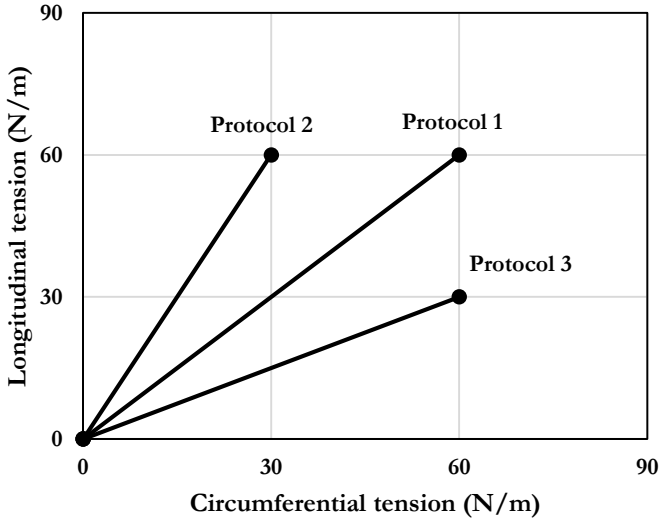

Figure 4.2: Biaxial loading protocols applied for testing of infarct samples.

Mean stress-strain graphs in the circumferential and longitudinal directions were presented for different infarct groups. To quantify the tensile stiffness in the two material axes, circumferential and longitudinal tensile moduli were calculated from the equibiaxial stress-strain data of each

sample. This was achieved by calculating the maximum slope of the stress-strain curve at the region bounded by 15 and 20 kPa of stress.

The non-equibiaxial loadings (i.e. Protocol 2 and 3) were introduced to examine the in-plane mechanical coupling between the circumferential and longitudinal axes and to provide the sufficient amount of data for the constitutive modelling. The mechanical coupling was examined by assessing the effect of increasing the tension in one axis on the extensibility of the other axis (Billiar and Sacks 2000; Ghaemi et al. 2009).

4.2.4 Uniaxial compression test

Following the biaxial test, tissue samples underwent transmural compression testing, up to 30% of the sample thickness, using a uniaxial testing System (Mach-1, Biosyntech, MN, USA). Samples were secured in place using a small amount of cyanoacrylate ester adhesive. The compression was applied at the 4 locations of optical markers using a plate indenter of ~2.7 mm diameter while sample submerged in 10% PBS as illustrated in Figure 4.3. As such, 4 compression measurements were obtained from a single sample. Each marker spot was preloaded to 2 g, preconditioned for 10 cycles of 5% compression and then loaded to 30% compression. Compression load was applied at rate of $\frac{T}{10}$ mm/s, where T is the sample thickness. This is equivalent to strain rate of 0.1/s.

Compressive stress-strain data was obtained for the different infarct groups. The compressive moduli were calculated from the slope of the stress-strain curve at the region bounded by 25% and 30% of compressive strain.

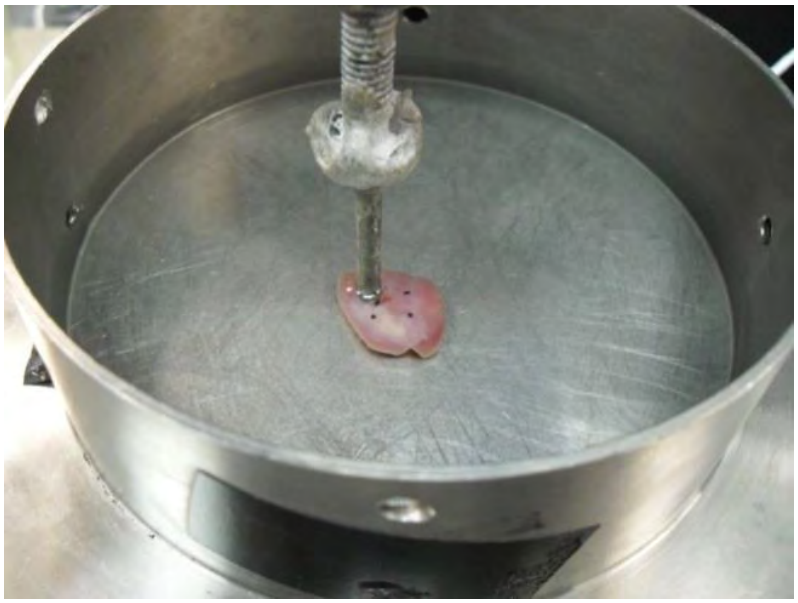

Figure 4.3: Compression test of infarcted tissue samples.

4.2.5 Histology

Following mechanical testing, the infarcted tissue samples of the 7, 14 and 28 day groups were fixed in 4% paraformaldehyde for 48 hours and then in 70% ethanol. Histology analysis was performed to confirm and quantify the infarction in each sample.

The freehand diagram in Figure 4.4 illustrates sample dissection and marking for histology analysis. The tissue portion above the ligation site was cut away since it has no significance in the infarct analysis. The sample was then cut into 4 equal circumferentially-adjacent blocks differentiated with different colours on the lateral surface so that section were obtained from the medial surface. The blocks were processed through graded alcohols (Illovo Sugar Ltd., Durban, South Africa) xylene (Saarchem, Gauteng, South Africa) and infiltrated with paraffin wax using the Tissue-Tek Rotary Tissue Processor (Sakura Finetek, Tokyo, Japan). After that, tissue blocks were embedded in paraffin wax (Merck KGaA, Darmstadt, Germany) and 2 sections of 4 μm were cut from the medial surface of each block , i.e. 8 sections per sample, at 0 and 120 μm using a Rotary Microtome HM360 (Microm, Waldorf,Germany). Sections were picked up on glass slides (Marienfeld GmbH & Co. KG, Lauda-Königshofen, Germany) and baked on a hot plate at 60 °C (Kunz Instruments AB, Nynäshamn, Sweden) for 30 minutes before being dewaxed in xylene and hydrated through graded alcohols down to water.

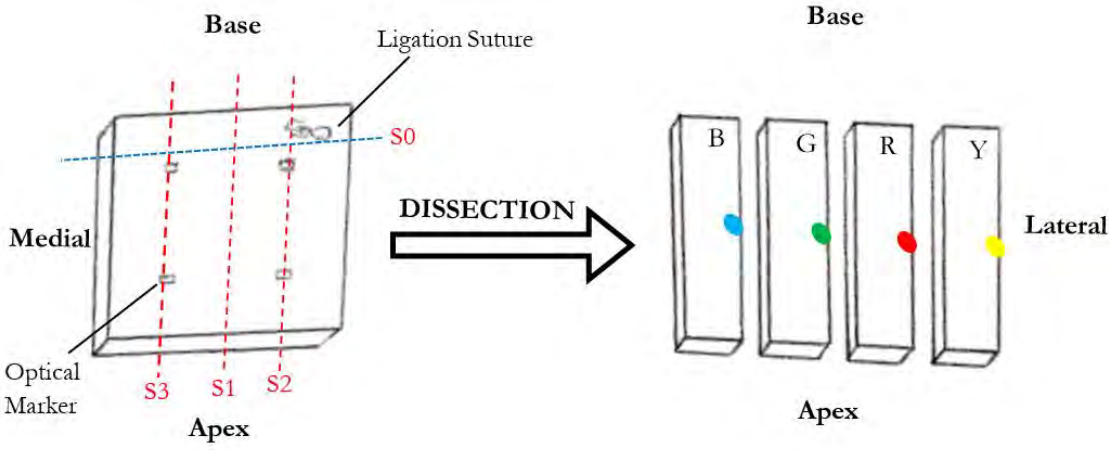

Figure 4.4: Schematic of tissue sample dissection and marking.

Tissue sections were then stained using Masson's trichrome to distinguish the collagen fibres from myocytes in the tissue. A 0.5% Acid Fuchsin solution (Merck KGaA, Darmstadt, Germany) was applied for 5min and rinsed in tap water. Excess Acid Fuchsin was removed by applying 1% Phosphomolybdic acid solution (SigmaeAldrich Chemie GmbH, Steinheim, Germany) for 5min. The slides were then washed in water and counterstained for 2 min with 2% Light Green SF Yellowish (Sigma Aldrich Chemie GmbH, Steinheim, Germany) before they were dehydrated

through alcohol, cleared with xylene and mounted with Entellan (Merck KGaA, Darmstadt, Germany).

4.2.6 Infarct quantification

Images of histology sections were acquired using Eclipse 90i microscope with DXM-1200C digital camera (Nikon Corporation, Tokyo, Japan) at 2 × magnification and stitched (NIS Elements BR 3.0, Nikon Corporation). Digital images of tissue sections were imported in Visiopharm Integrator System (Visiopharm, Hørsholm, Denmark) for analysis. The infarct and intact areas, characterized by the presence of collagen and cardiomyocyte respectively as demonstrated in Figure 4.6 (a), were measured in each section using an unsupervised image analysis in which infarct and intact regions were segmented using coloured masks, Figure 4.6 (b). The percentages of the infarct and intact areas in the individual sections were calculated. The overall infarct size of a sample was estimated by normalizing the sum of infarct areas in the 8 sections by the sum of the entire section areas. Samples that exhibited less than 40% infarction were excluded from the study (will be discussed later).

4.2.7 Statistical analysis

The experimental data were presented as mean ± standard deviation (SD). The statistical analysis was performed using one-way analysis of variances (ANOVA) followed by Fisher least square deviation (LSD) multiple comparison post-hoc test between groups (STATISTICA 12, StatSoft, Inc., Tulsa, USA). The differences were considered statistically significant when $p<0.05$.

4.3 Results

4.3.1 Visual inspection of harvested hearts

By visual inspection of the harvested hearts, the 0d infarct hearts did not show noticeable changes and thus distinguishing the infarct zone was not applicable. However, the infarct zone was clearly visible on the hearts of 7, 14 and 28d groups as shown in Figure 4.5. The infarct zone extended distal to the ligation site. The damaged tissue appeared in a pale colour which was distinguishable from the red/brown colour of the surrounding intact myocardium. A loss in the muscle tone and wall thinning were also remarkable characteristics of the infarcted tissue in contrast to the intact myocardium.

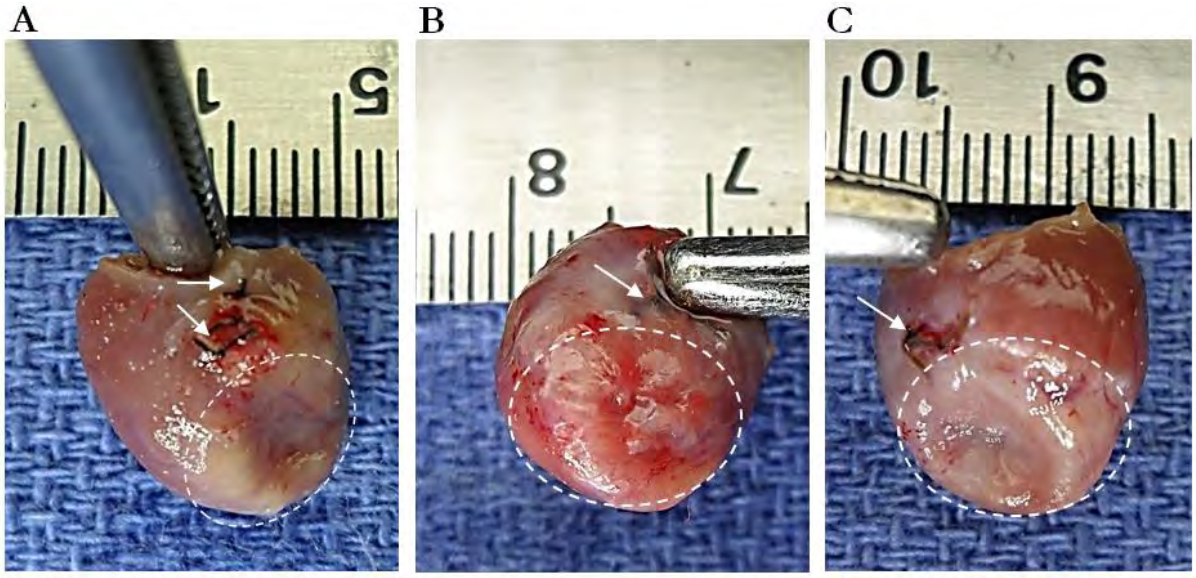

Figure 4.5: Harvested infarcted hearts at 7 (a), 14 (b) and 28 days (c) after coronary artery ligation showing the infarcted tissue (dotted circle) and locations of ligating sutures (arrow).

4.3.2 Histology-based infarct size estimation

Staining the tissue sections of the infarcted samples with Masson's trichrome distinguished the collagen fibres from myocytes. The collagen appeared blue while myocytes appeared red as illustrated in Figure 4.6 (a). As a result of segmentation in Visiopharm, Figure 4.6 (b), the collagen and myocytes were covered with blue and green masks, respectively. As such, the area of these masks represented the areas of the infarct and intact tissue in a section. Holes and gaps in the tissue (background) were masked using grey colour and were not included in the analysis.

The histogram in Figure 4.7 shows a quantification of infarct in the individual sections of samples for different groups. The infarcted area was presented as percentage of the entire section area. For illustration purposes, the samples in each group were numbered from 1 to 9 while sections were numbered from 1 to 8. Some samples were fully intact, i.e. without any infarcted tissue, indicating an unsuccessful MI induction, e.g. Sample 2 at 7d, Sample 7 at 14d and Sample 1 at 28d. No sample showed infarction in all of the 8 sections; the maximum was 7 sections. The estimated infarct size in samples is shown in Figure 4.8. The overall average infarct size for the 7d, 14d and 28d infarct groups was found to be 50%, 49% and 53%, respectively.

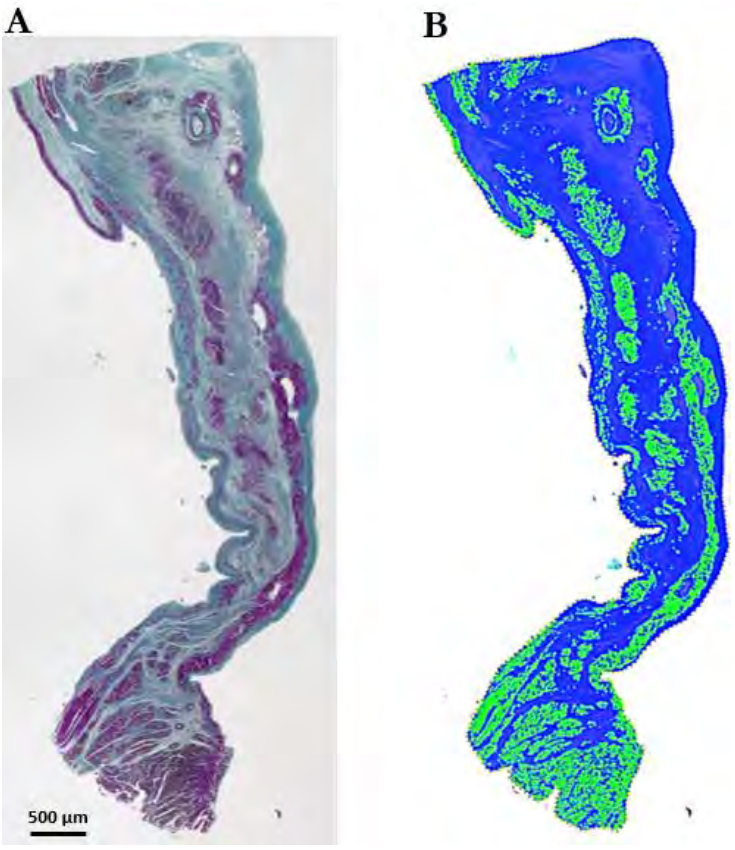

Figure 4.6: (a) Histological micrograph of an infarcted tissue section stained with Masson's trichrome. Collagen appears blue and myocytes appears red. (b) Image after being segmented in Visiopharm. Blue and green masks represent collagen and myocytes respectively.

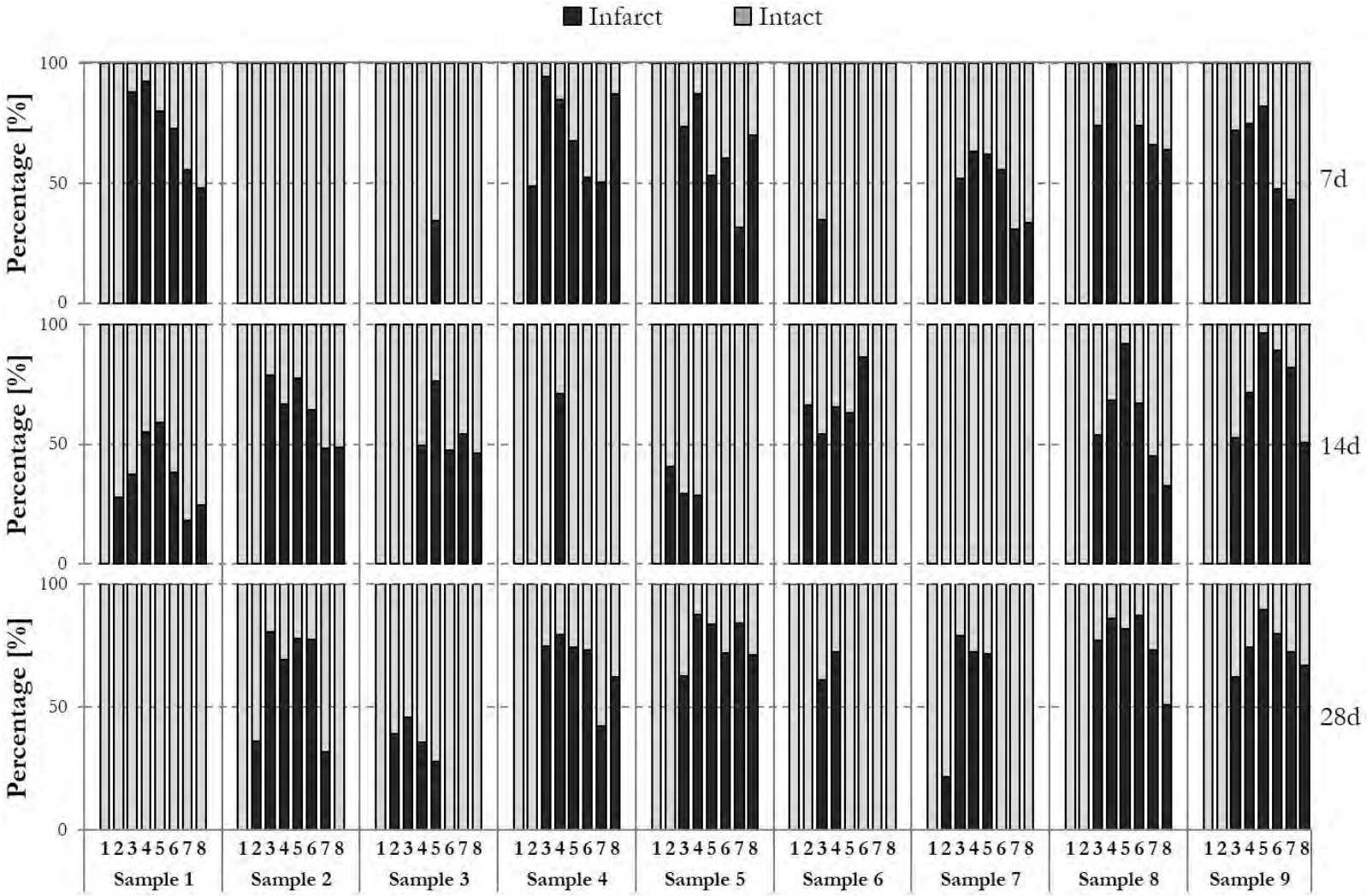

Figure 4.7: Histogram of the percentage of infarcted area in individual sections of tissue samples for 7, 14 and 28d groups.

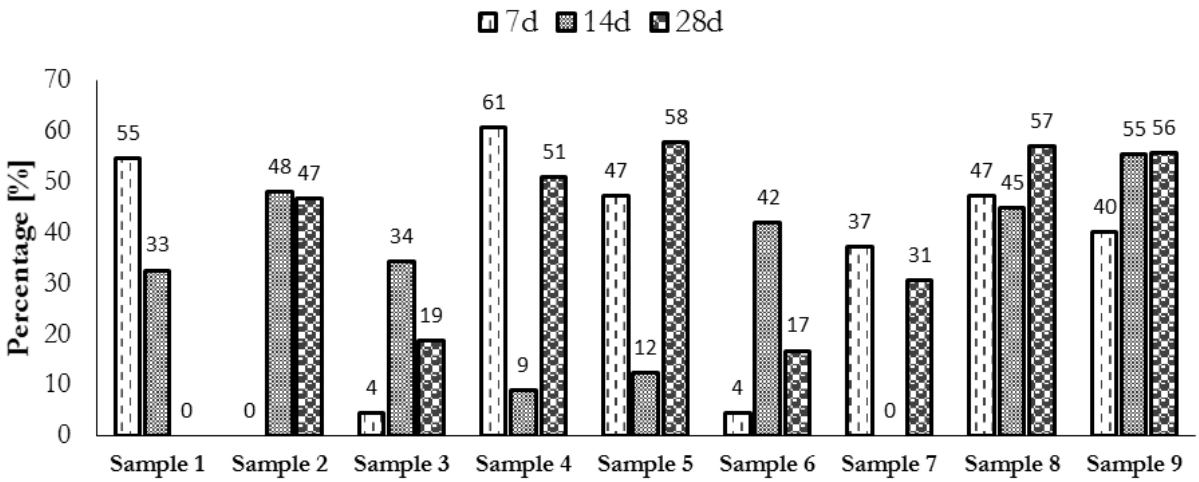

Figure 4.8: Estimated infarct size in tissue samples of 7, 14 and 28 day infarct groups.

4.3.3 Equibiaxial tension

The biaxial testing of some samples failed due to technical issues producing incomplete mechanical data. These samples were excluded from the study. Table 4.1 summarizes the final number of samples from each infarct group for all protocols of biaxial testing.

Table 4.1: Total number (n) of samples that underwent biaxial testing.

Infarct group	0d	7d	14d	28d
n	5	5	3	4

The stress-strain relationship of the equibiaxial test for different infarct groups is shown in Figure 4.9. In general, all infarct groups exhibited an anisotropic nonlinear behaviour in which the circumferential direction was stiffer than the longitudinal direction. However, a significant difference was observed between the maximum circumferential and longitudinal strains (i.e. at 20 kPa of stress) in the 0d, 14d and 28d infarct groups ($p=0.0098$, 0.0056 and 0.045 respectively). The 0 and 7d groups, Figure 4.9 (a) and (b) respectively, showed an isotropic behaviour at lower strain (up to ~0.07 for 0d and ~0.05 for 7d). The anisotropy in the 14d infarct group, Figure 4.9 (c), was more pronounced than in other groups.

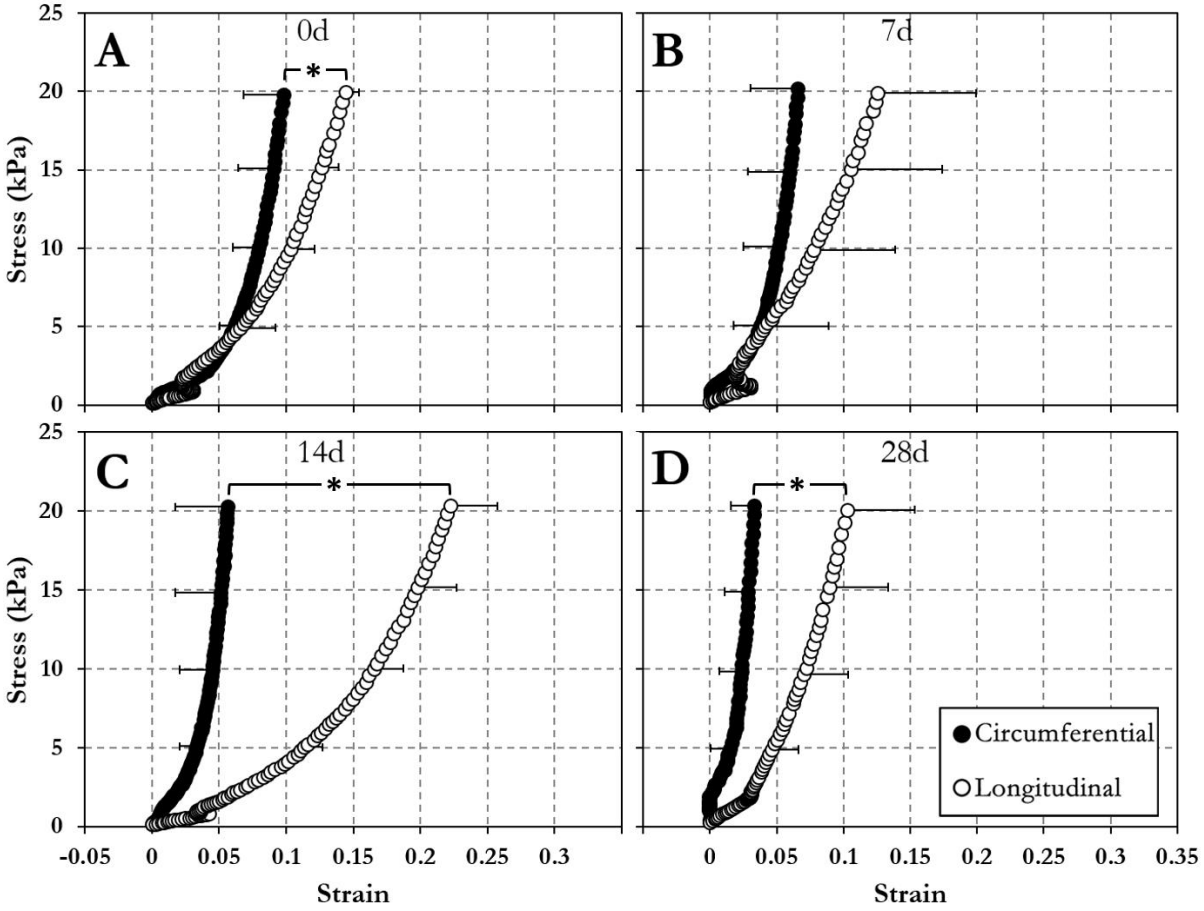

Figure 4.9: Mean stress-strain relationship from the 60:60 N/m biaxial test for 0 (a), 7 (b), 14 (c) and 28 day (d) infarct group. Error bars represent SD and were partially presented for illustration purposes. * $p<0.05$.

The tensile modulus, shown in in Figure 4.10, was calculated for the different infarct groups as an indication for infarct stiffness. In the circumferential direction, Figure 4.10 (a), the moduli for 0d, 7d, 14d and 28d groups was found to be 443, 670, 857 and 1218 kPa, respectively. The stiffness increased in proportion to the increasing time after coronary ligation. The modulus of the 28d infarct was significantly higher compared to the 0d ($p=0.0098$) and 7d ($p=0.048$) infarcts. In the longitudinal direction, Figure 4.10 (b), the infarcts at 0, 7 and 14 days exhibited moduli of 247, 250 and 212 kPa, respectively. At 28 day an increase in the stiffness was observed (487 kPa), yet insignificant.

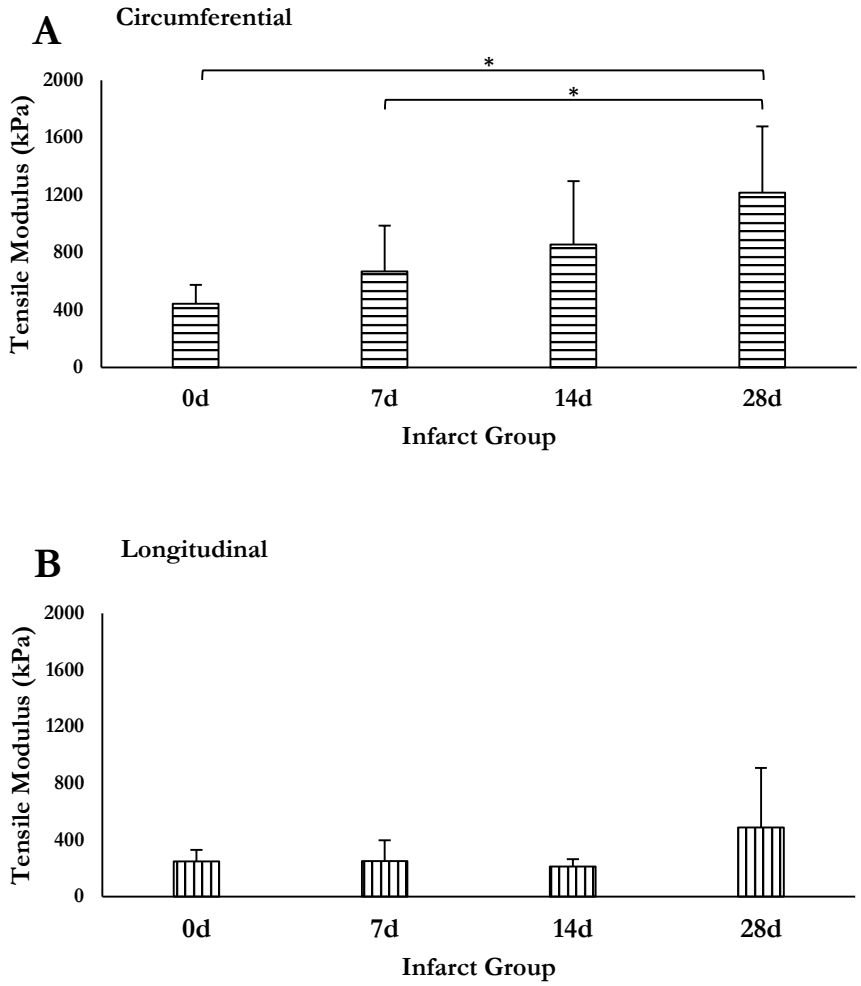

Figure 4.10: Mean circumferential (a) and longitudinal (b) tensile modulus calculated for different infarct groups. Error bars represent SD. * $p<0.05$.

4.3.4 Non-equibiaxial tension

The stress-strain relationship of the 30:60 biaxial test for different infarct groups is shown in Figure 4.11. All infarct groups exhibited negative circumferential strain due to the in-plane mechanical coupling between the two axes. The variation in the circumferential extensibility between infarct groups was very limited compared to the longitudinal extensibility. The stress-strain graphs from the 60:30 loading protocol are shown in Figure 4.12. Negative longitudinal strains were observed in the 0 and 7d groups only.

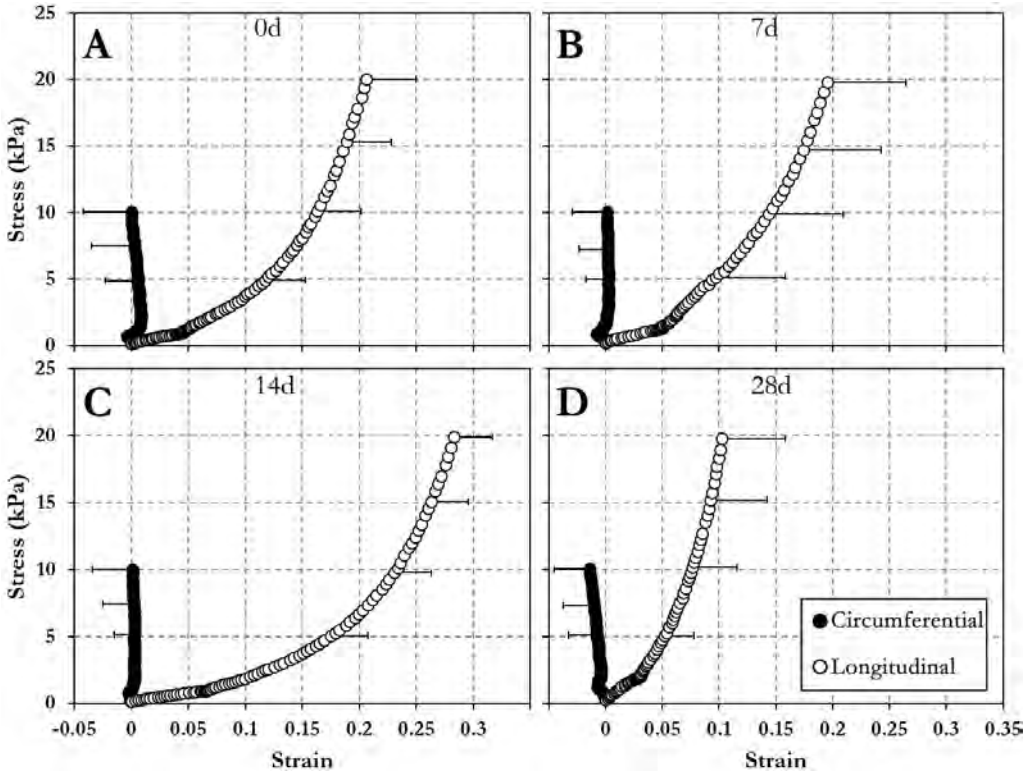

Figure 4.11: Mean stress-strain relationship from 30:60 N/m biaxial test for 0 (a), 7 (b), 14 (c) and 28 day (d) infarct group.

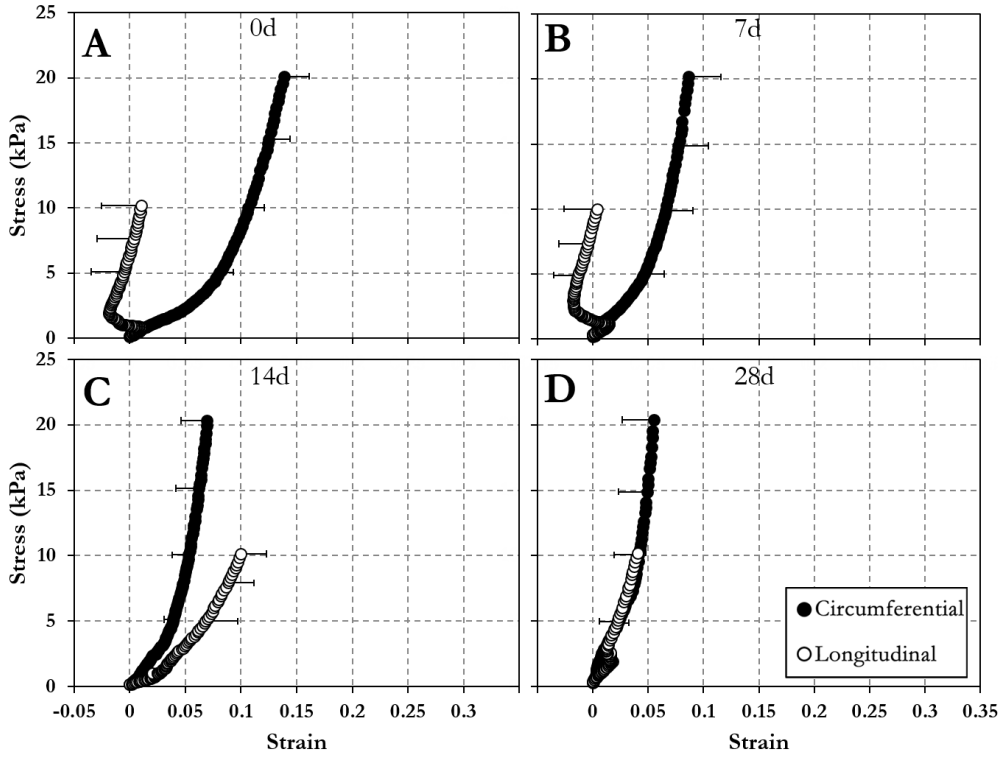

Figure 4.12: Mean stress-strain relationship from 60:30 N/m biaxial test for 0 (a), 7 (b), 14 (c) and 28 day (d) infarct group.

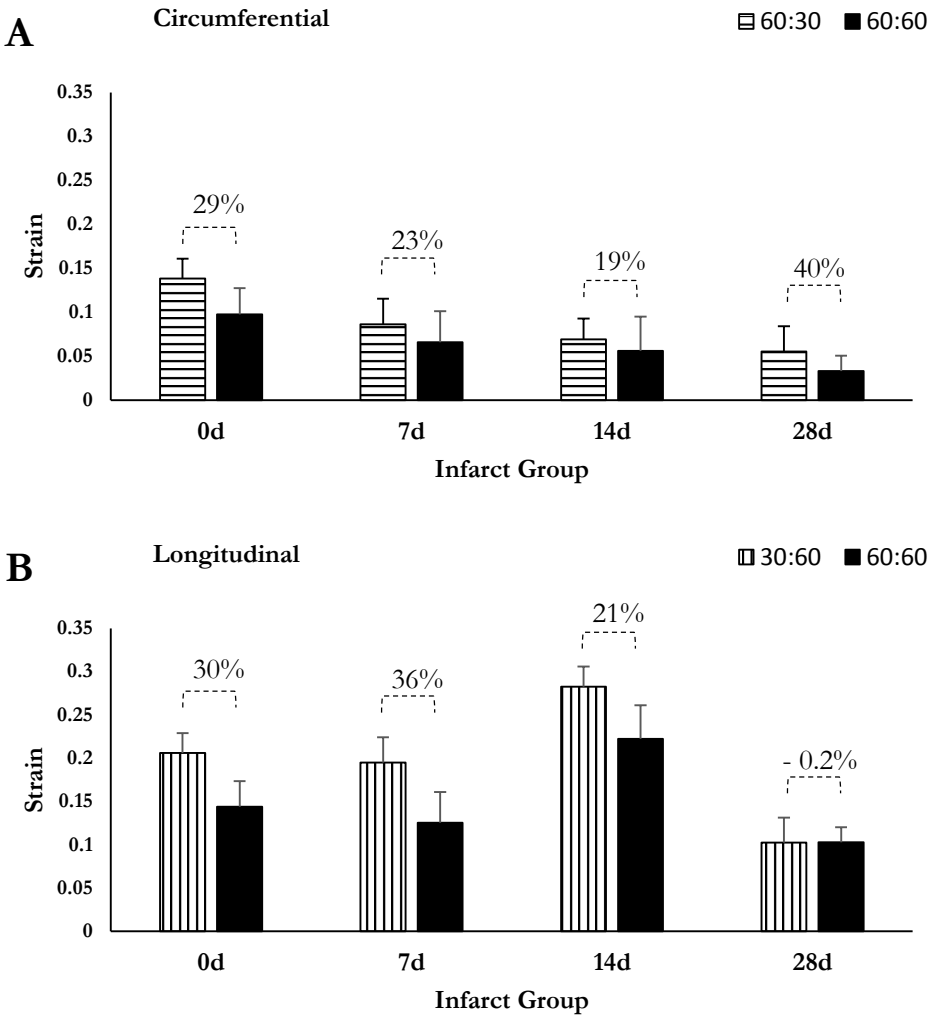

Figure 4.13: Peak circumferential (a) and longitudinal (b) strain obtained from different loading protocols demonstrating the effect of mechanical coupling. The percentage change in strain between loading protocols is indicated for each infarct group. Data are presented in mean and error bars represent SD.

The in-plane mechanical coupling between the circumferential and longitudinal direction of infarcts was assessed by comparing the change in extensibility in one direction as the load increases in the other direction. Figure 4.13 illustrates the change in peak strain in one direction as the tension changes in the other direction. For example, the 7d infarct exhibited 23% decrease in the circumferential strain when the longitudinal tension was increased from 30 (in the 60:30 protocol) to 60 N/m (in the 60:60 protocol) as shown in Figure 4.13 (a). However, the longitudinal strain of the same group decreased by 36% when the circumferential tension was increased from 30 (in the 30:60 protocol) to 60 N/m (in the 60:60 protocol). The mechanical coupling in 0 and 14d groups was nearly symmetric, i.e. equal change in directional strain, whereas asymmetric mechanical coupling was observed for 7 and 28d groups. The strongest mechanical coupling (40%) was observed in the circumferential direction of the 28d group with negligible change in the

longitudinal strain. This indicates that the longitudinal axis had a stronger mechanical effect on the circumferential axis in the 28d infarct.

4.3.5 Compression

Erratic compression measurements from some samples were excluded from the study. Several compression measurements were obtained from a single sample. Table 4.2 illustrates the total number of measurements obtained for each infarct group.

Table 4.2: Total number (n) of compression measurements obtained for different infarct groups.

Infarct group	0d	7d	14d	28d
n	5	6	8	6

Figure 4.14 illustrates the compressive mechanical properties of the infarcted myocardium. All infarct groups exhibited a non-linear compressive stress-strain behaviour as shown in Figure 4.14 (a). Up to 10% of compressive strain, a similar linear stress-strain behaviour was observed. Variation between groups became more pronounce as the strain exceeded 20%.

The compressive moduli, shown in Figure 4.14 (b), was found to be 145, 242, 247 and 522 kPa for 0d, 7d, 14d and 28d infarct groups. The 28d infarct group showed a significantly higher compressive modulus compared to other infarct groups ($p = 0.0055$, 0.028, and 0.018 for 0, 7 and 14d groups respectively).

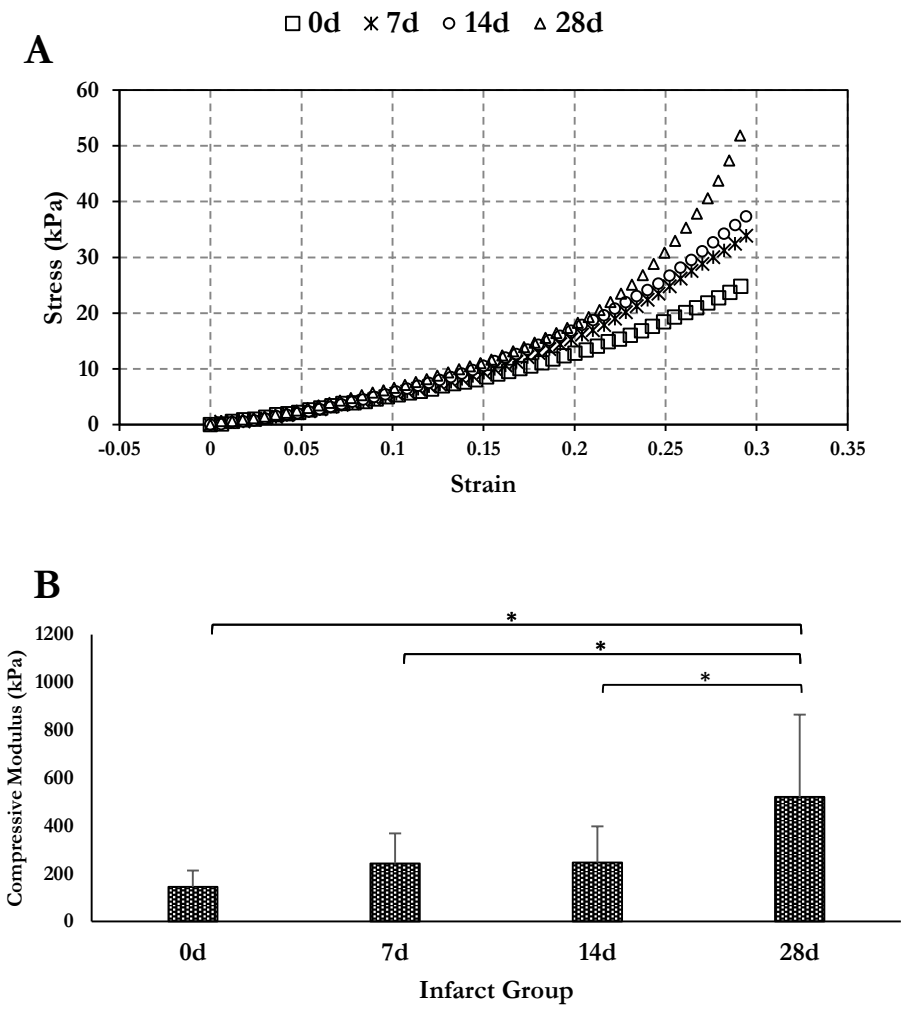

Figure 4.14: Compressive mechanical properties of infarcted myocardium. (a) Mean compressive stress-strain relationship for different infarct groups. (b) Mean compressive modulus calculated for different infarct groups. Error bars represent SD. * $p<0.05$.

4.4 Discussion

This study investigated the mechanical behaviour of rat infarcted myocardium under different loading conditions taking into account the temporal change in mechanical properties of healing infarcts. The infarcted hearts were explanted immediately, 7, 14 and 28 days after LAD coronary artery ligation. Infarct samples underwent planar equibiaxial and non-equibiaxial tensile tests followed by wall compression test. Infarcts maintained anisotropy and the nonlinear biaxial and compressive mechanical behaviour throughout the healing phases. At low strain range, infarcts could exhibit isotropy during the first week after the infarct onset. Mechanical coupling was observed between the two axes in all infarct groups. Infarcts were stiffer in the circumferential direction compared to the longitudinal. With progression of infarct healing, the increase in the

circumferential and compressive stiffness was more significant than the increase in longitudinal stiffness.

4.4.1 Induction of myocardial infarction

In vivo MI induction in rats is a challenging procedure due to some commonly known factors. These include the small size of a rat heart, the small exposure site and the difficulty in maintaining a consistent infarct size. The latter is a crucial factor when aiming at mechanically testing the infarct. Ideally, the testing sample should be 100% infarcted to precisely capture the mechanical properties of the infarct.

In the current experiments, the aim was to induce as large infarcts as possible. One way to achieve this was by using multiple ligation sites (Figure 4.5 (a)) instead of a single site. Another utilized technique was to increase the size of the occluded region as proposed by Huang et al. (2006). Yet no samples from the 7, 14 or 28 day groups was 100% infarcted. Furthermore, MI induction was completely unsuccessful in some samples yielding 0% infarct size (Figure 4.8) and produced relatively small infarct sizes such as 4, 9 and 12% in other samples. This highlights the difficulty to control the infarct size or maintain its consistency among infarct groups.

4.4.2 Area-based quantification of infarcts

The histology analysis was performed following mechanical testing to examine the consistency of the induced infarcts. In order to provide an adequate estimate of the infarcted wall in a sample, histology-based measurement of the infarcted area was applied in 8 equidistant parallel sections of the testing sample.

MI studies that involve experimental infarcts in rodent models usually followed two common histology-based approaches to estimate the infarct size in the LV: (1) measuring the area of the infarcted region (Piot et al. 1997; Liu et al. 2002; Park et al. 2004) or (2) measuring the arc length of the infarcted region (Pfeffer et al. 1979; Kadner et al. 2012). The area-based method is often used with early stage infarcts. However, the wall thinning associated with the late stage infarcts makes the length-based method more suitable (Takagawa et al. 2007).

Although the current experiments involved chronic infarcts, the area-based method was utilized. Unlike other studies in which infarct size was measured in the entire LV, the infarct size in this study was measured in the sample only. The sample represented a small portion of the LV where the infarct would most likely lie. As such, even though a sample experienced wall thinning, the thickness was uniform in the whole sample. Furthermore, the area-based method was more

accurate and limited the subjectivity. Applying this method at 8 equally spaced sections provided an adequate estimate of the infarct size on a sample.

4.4.3 Infarct size threshold

Following the histological analysis of infarct samples, an infarct size threshold of 40% was determined. A sample of infarct size below 40% was considered poorly infarcted and excluded from the study. The motivation for obtaining this threshold originated from the fact that no sample from the chronic infarct groups (i.e. 7, 14 and 28 day) was 100% infarcted (Figure 4.8). As such, it was necessary to ensure that the entire central target region of the biaxial testing samples (Sacks 2000) contained as much properly infarcted tissue as possible.

The histogram of the infarcted area in individual sections (Figure 4.7) provides information on the distribution of the infarct both circumferentially and longitudinally. All samples were cut at the ligation site prior to histology analysis. Therefore, a single bar in the histogram demonstrates how far the infarct in that particular section extends in the longitudinal direction. The 8 bars of a sample represent equally spaced longitudinal sections and thus together illustrate how far the infarct extends circumferentially. Examining the histology images and the in-plane extension of the infarct, 40% was found to be the minimum infarct size required to ensure a transmural and adequate circumferential and longitudinal extend of the infarct.

By eliminating samples that exhibited less than 40%, the chance that the mechanical properties were captured from properly infarcted target region was considerably increased. This was also confirmed for the compression data since compressive loads were applied at the optical markers which were located in the target region. It is important, however, to note that the 40% value was obtained based on the analysis of the sets of infarcted hearts presented in this study and is not necessary suitable for other studies.

4.4.4 Infarct quantification in the immediate infarct group

The infarct size in the immediate (i.e. 0d) group was not quantified in this study. Collagen starts accumulating in infarcted tissue at 2 days after infarction onset (Cleutjens et al. 1999). Therefore, Masson's trichrome staining was not suitable for this group since the infarcted hearts were harvested few minutes after coronary ligation. Triphenyltetrazolium chloride (TTC) staining is a macroscopic approach widely used to identify early phase post-mortem infarcted myocardial tissue (Fishbein et al. 1981; Khalil et al. 2006). In a pilot study on the 0d infarcts, TTC staining did not

identify the infarcts after biaxial testing although successfully did so on samples that did not undergo biaxial testing. The major causes of this observation are not yet fully understood.

Nevertheless, all hearts from the 0d group were assumed to be properly infarcted and thus included in the study. This assumption was based on a key argument. Since the heart was to be harvested immediately, a lengthy thoracotomy was made during operation and the heart was openly exposed allowing comfortable access to the LAD coronary artery. As such, the MI in this group was induced with high certainty providing a consistent mechanical properties as illustrated by the relatively small standard deviation in this group (Figure 4.9 (a)).

4.4.5 Mechanical properties of infarcts

Our study showed that infarcts maintain the non-linear anisotropic mechanical behaviour throughout the different healing stages with varying degree of anisotropy (Figure 4.9). However, during the first 7 days after coronary ligation, infarcts showed an isotropic behaviour under low strain. Anisotropic behaviour of the infarcted tissue under equibiaxial tension was also observed in previous studies on sheep models (Gupta et al. 1994; Gundiah et al. 2004). One exception was the study by Fomovsky and Holmes (2010) who suggested that healing rat infarcts were isotropic.

These studies and others (Cleutjens et al. 1995; Fomovsky et al. 2010) demonstrate that collagen is the major determinant of the mechanical properties of the infarcted myocardium. In particular, the degree of anisotropy is primarily determined by the alignment of the collagen fibres although isolated muscle fibres may have an effect (Gupta et al. 1994). A previous study on rat infarcts (Fomovsky et al. 2012) showed that the alignment of collagen fibres varies with the location in the LV as illustrated in the histograms in Figure 4.15. For example, collagen in a mid-ventricle infarct was aligned mostly in the circumferential direction (0°) while collagen fibres were randomly oriented in an apical infarct. As such, the discrepancy between the findings of the current and Fomovsky's studies with regard to categorizing the mechanical behaviour of the infarct can be attributed to the different location of the examined infarcts. Highly oriented collagen fibres, observed in a mid-ventricle infarct, induces anisotropy while a random collagen orientation, observed in an apical infarct, will yield an isotropic behaviour. In the current study, the infarct samples contained a considerable portion of the anterior wall of the LV. Therefore, they showed mechanical anisotropy with the circumferential direction being stiffer than the longitudinal due to the circumferentially oriented collagen.

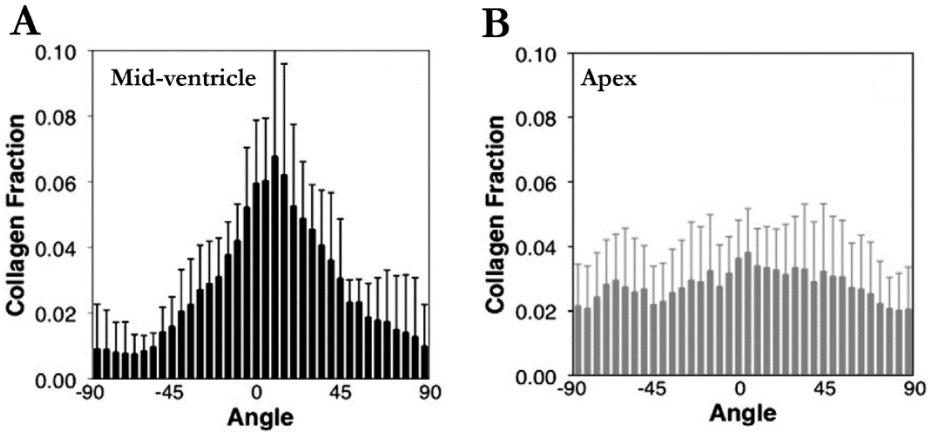

Figure 4.15: Histograms of collagen content and orientation in rat infarcts at 3 weeks after infarction. (a) Infarct located at the mid-ventricle region. (b) Apical infarct. (modified from Fomovsky et al. (2012))

The orientation of collagen and the degree of cross-linking is believed to play a major role in the mechanical coupling (Figure 4.13) observed between material axes when infarcts are subjected to non-equibiaxial tension. Mechanical coupling has been reported for several biological soft tissues such as; myocardium (Yin et al. 1987; Ghaemi et al. 2009), pericardium (Sacks and Chuong 1998), valve leaflet (Billiar and Sacks 2000) and urinary bladder (Gilbert et al. 2008). The exact underlying mechanism which causes this phenomena is not clear although some hypothesis attributed it to the dynamic change of collagen orientation in response to the unequal biaxial loading (Yin et al. 1986; Billiar and Sacks 2000). Nevertheless, the non-equibiaxial experiment presented in this study provides the data required to identify material parameters for different infarcts.

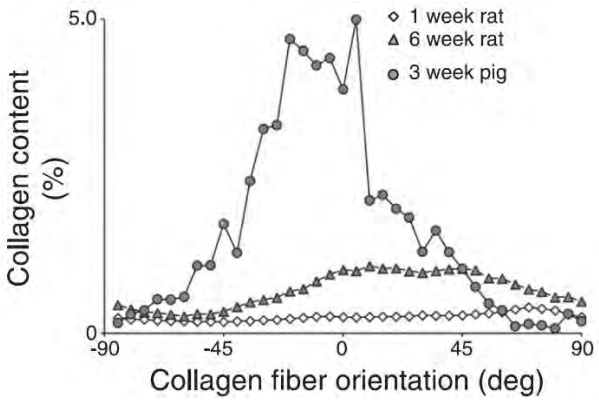

Figure 4.16: Histograms of collagen content and orientation in infarcts from rat and pig models at different time points after infarction. (modified from Fomovsky and Holmes (2010))

The increase in the circumferential (Figure 4.10 (a)) and compressive (Figure 4.14) stiffness of the healing infarcts with time is attributed to the accompanying increase in collagen deposition and cross-linking (Vivaldi et al. 1987; Cleutjens et al. 1995). While the compressive stiffness is related to the content of collagen, the directional stiffness is predominantly controlled by the orientation of the deposited collagen. For example, the change in the longitudinal stiffness (Figure 4.10 (b))

with increasing healing time, though not statistically significant, could be attributed to the circumferential orientation of the accumulated collagen. These arguments agree with the findings from a previous study (Fomovsky and Holmes 2010) as shown in the histogram Figure 4.16. The histogram shows the collagen content and orientation in rat infarcts at 1 and 6 weeks after infarction. The increase in collagen content at 6 weeks compared to 1 week is noticeable. However, the increase in the content of the longitudinal collagen is very small compared to that of the circumferential collagen. In the current study, the circumferential stiffness of the infarct at 28 days was significantly higher compared to 7 days, whereas the difference in longitudinal stiffness between 7 and 28 days was not statistically significant.

5 Identification of material model parameters of infarct tissue

5.1 Introduction

Computational biomechanics has been effectively utilized for disease investigation and therapy optimisation providing answers to many clinical questions. In the cardiovascular area, finite element (FE) models have been established for studying the mechanical aspects of myocardial infarction (MI) (Wenk et al. 2011a) and its emerging intramyocardial injection treatment (Kortsmit et al. 2013; Miller et al. 2013).

The passive constitutive behaviour of myocardium has been modelled as transverse-isotropic (Humphrey et al. 1990b; Guccione et al. 1991) or orthotropic (Costa et al. 2001; Holzapfel and Ogden 2009) incompressible finite elastic material using hyperelastic pseudo-strain energy functions. Inverse methods are utilized for estimating the parameters of these constitutive models by fitting FE models solution to experimental data. Such experimental data are obtained either from mechanical testing of isolated heart samples, e.g. stress-strain relationship from biaxial testing, or by measuring regional deformation from the whole heart in vivo or in vitro, e.g. local myocardial strain using ultrasound imaging, (Usyk and McCulloch 2003).

Omens et al.(1993) inflated a left ventricle of an isolated rat heart using balloon and measured the two-dimensional strain. FE model was developed to optimise the parameters of a transversely isotropic strain energy function by fitting solutions to the measured experimental strain. Gupta et al. (1994) utilized orthotropic model to fit biaxial data of sheep infarcted myocardium. Fomovsky and Holmes (2010) used the least-squares method to fit isotropic constitutive model to biaxial stress-strain data of infarcted rat heart. Lee et al. (2011) developed a FE model of an infarcted left ventricle of a sheep heart. They optimised active parameters in a transversely isotropic material model to fit in vivo end-systolic strains and cavity volume measured from tagged magnetic

resonance images (MRI). A similar approach was used by Wenk et al. (2012), however, passive and active parameters of the material model were optimized by fitting FE solutions to patient-specific measurements from tagged MRI.

Genetic algorithm (GA) is a global search method based on the concept of biological evolution. Treating sets of solutions in optimization problems as "chromosomes", GA applies genetic operations, such as crossover and mutation, to form an improved chromosomes in the newly developed generations. GA has been employed for problem optimization in the medical field. Wang et al. (2006) used GA to optimise parameters of Fung strain energy function for pig coronary arteries. GA were combined with FE modelling and employed in elasticity reconstruction of atherosclerotic arterial plaque (Khalil et al. 2006). GA and FE modelling were also utilized by Yeoman et al. (2009) and Kichula et al. (2014) to optimize material parameters for vascular graft and myocardial tissue, respectively.

In this chapter, the aim was to identify the parameters of an orthotropic constitutive model for the different healing stages of rat heart infarcts utilizing the biaxial mechanical data presented in Chapter 4. A biaxial tension FE model was developed mimicking the setup of the experimental biaxial test. The model underwent verification tests to optimize the model attributes. GA was employed to minimize the error between the predicted and experimental data.

5.2 Materials and methods

5.2.1 Biaxial tension finite element model

Abaqus CAE 6.12-2 (Dassault Systèmes, Providence, RI, USA) was employed to build and run the biaxial tension FE model. A three-dimensional (3D) model of the tissue sample was generated by extruding a square area of length (l) by depth (T) as illustrated in Figure 5.1. The endocardial and epicardial surfaces were represented by x-y planes at z=0 and z= T respectively. As a result, the x and y axes of the model represented the circumferential and longitudinal axes respectively. The eight suture needles (C1 to C8) used in the experiment were modelled using cylindrical transmural partitions of 0.4 mm diameter (the physical diameter of the needles). The two adjacent cylinders on each side were separated by l/3 while all cylinders were positioned 2 mm away from the edge. Four reference points (RP1 to RP4) were defined at the central area of the epicardial surface of the model representing the four optical markers used in the experiment. A tie constraint was defined to couple the movement of the four reference points (slave) to the local movement of the epicardial surface (master).

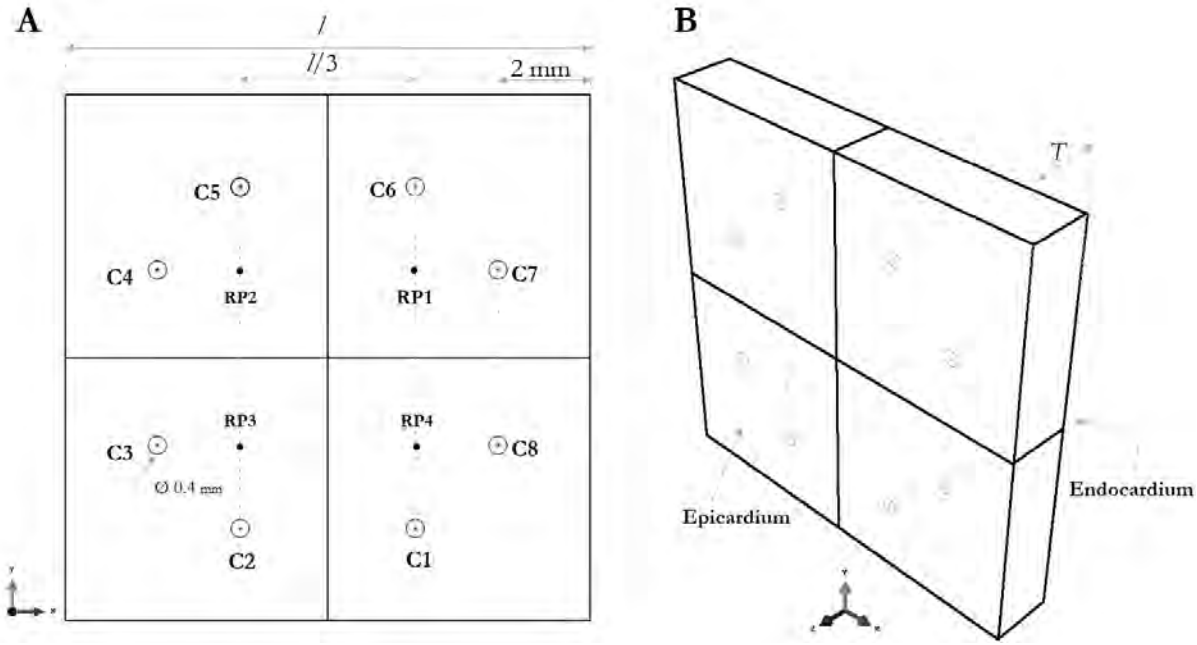

Figure 5.1: (a) Two-dimensional sketch of the FE model showing the positions of suture needles (C1-8) and reference points (RP1-4). (b) Extruded geometry of the specimen showing epicardial and endocardial surfaces.

Four models were developed representing the four infarct groups, i.e. immediate (0 day), 7, 14 and 28 days. The models were assigned the mean length (l) and thickness (T) measured from individual samples in each infarct group. Table 5.1 shows the dimensions assigned to the four models.

Table 5.1: The dimensions of the biaxial tension model for different infarct groups.

Model	l [mm]	T [mm]
0 day infarct (0d)	12.09	3.04
7 day infarct (7d)	11.72	2.42
14 day infarct (14d)	11.81	3.07
28 day infarct (28d)	11.41	1.80

The model was discretized using linear hexahedral reduced-integration hybrid elements (C3D8RH). The mesh contained 1896 elements. The orientation of myocardial fibres was incorporated in the model by a user-defined material orientation (ORIENT) subroutine. The subroutine was utilized to define fibre orientation in the specimen model through 14 transmural layers of fibre angles. The fibre angles ranged linearly from -50° at the epicardial layer to 80° at the endocardial layer (Chen et al. 2003).

The mesh density, element type and number of transmural layers of fibres were determined from a series of verification tests as will be discussed later in detail.

5.2.2 Boundary and loading conditions

Displacement boundary conditions were applied to the cylinders to restrain the model (C1 to C4) and to apply the tensile loads (C5 to C8) as illustrated in Figure 5.2. The translational movement of C1 and C2 was constrained in the y-axis while the translational movement of C3 and C4 was constrained in the x-axis. All cylinders were allowed to rotate freely. Circumferential tensile load was applied by displacing C7 and C8 in the x-axis while longitudinal tensile load was applied by displacing C5 and C6 in the y-axis.

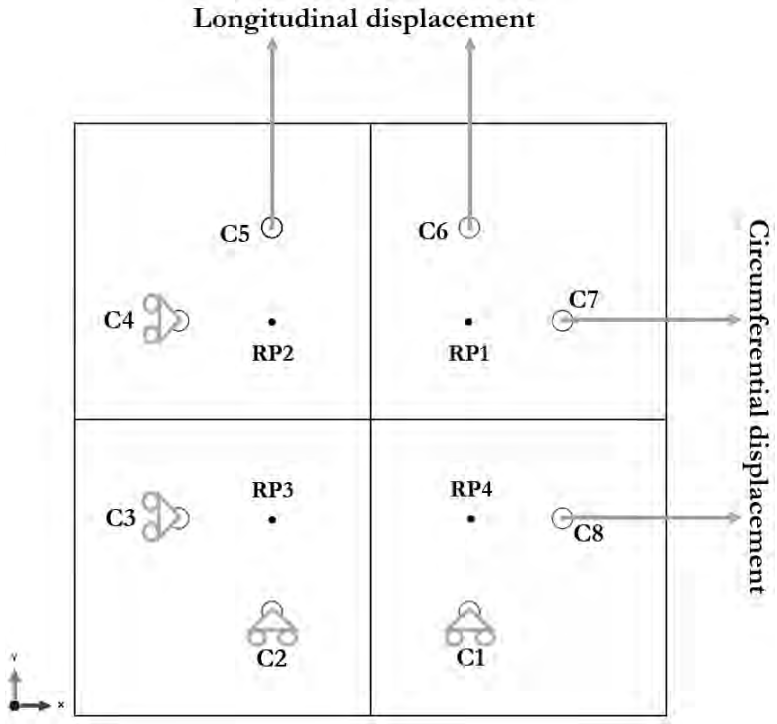

Figure 5.2: Illustration of the boundary conditions defined in the model.

5.2.3 Constitutive model

From a number of anisotropic hyperelastic constitutive models available in Abaqus, the orthotropic case of the generalized Fung model was utilized to model the material properties of the infarct. The generalized Fung strain energy potential is based on the exponential form suggested by Fung et al. (1979) appropriately generalized to arbitrary 3D states following Humphrey (1995). The generalized Fung strain energy function (W) has the following form (Abaqus 2012):

$$W = \frac{c}{2}(e^{Q} - 1) \quad 5\text{-}1$$

where c is the stress scaling factor and Q is given by

$$Q = \bar{\varepsilon}^{G} : b : \bar{\varepsilon}^{G} = \bar{\varepsilon}^{G}_{ij} b_{ijkl} \bar{\varepsilon}^{G}_{kl} \quad 5\text{-}2$$

where b_{ijkl} is a dimensionless symmetric fourth-order tensor of anisotropic material parameters and $\bar{\varepsilon}^{G}_{ij}$ and $\bar{\varepsilon}^{G}_{kl}$ are the modified Green strain tensor. For the orthotropic case of the generalized Fung model, 9 material parameters must be specified.

As explained by Sun and Sacks (2005), in the unloaded configuration matrix Dshould be positive definite in order to obtain numerical stability. Matrix D is given by:

$$D = \frac{c}{2}\begin{bmatrix} b_{1111} & b_{1122} & b_{1133} & 0 & 0 & 0 \\ b_{1122} & b_{2222} & b_{2233} & 0 & 0 & 0 \\ b_{1133} & b_{2233} & b_{3333} & 0 & 0 & 0 \\ 0 & 0 & 0 & b_{1212} & 0 & 0 \\ 0 & 0 & 0 & 0 & b_{1313} & 0 \\ 0 & 0 & 0 & 0 & 0 & b_{2323} \end{bmatrix} \quad 5\text{-}3$$

The positive definiteness implies the following parameter constraints:

- Constraint 1:

$$b_{1111}\, b_{2222} - b_{1122}^{2} > 0, \quad 5\text{-}4$$

- Constraint 2:

$$(b_{1111}b_{2222} - b_{1122}^{2})b_{3333} - b_{1111}b_{2233}^{2} + 2b_{1122}b_{2233}b_{1133} - b_{2222}b_{1133}^{2} > 0 \quad 5\text{-}5$$

- Constraint 3 to Constraint 9:

$$c > 0,\ b_{1111} > 0,\ b_{2222} > 0,\ b_{3333} > 0,\ b_{1212} > 0,\ b_{1313} > 0,\ b_{2323} > 0 \quad 5\text{-}6$$

These constraints were applied during the optimisation process of the material parameters, as will be described in the following section.

5.2.4 Optimization of material parameters

The aim was to optimize the material parameters of Fung-orthotropic model to fit the FE model solution to the experimental stress-strain data for up to 5% of biaxial strain; the average physiological range of infarct deformation (Fomovsky and Holmes 2010). Displacement-controlled FE simulations were run and the computed stress data were compared to the experimental data. The objective function (OBJ) utilized in the optimization was developed so that

it returns the mean absolute percentage error (MAPE). The GA toolbox in SCILAB 5.4 (Scilab Enterprises S.A.S, Versailles, France) was utilized to minimize the objective function. For each infarct model, the FE stress data were obtained from three simulations: M6060, M3060 and M6030, representing the three biaxial testing protocols of equibiaxial and non-equibiaxial loading described in Chapter 4; 60:60, 30:60 and 60:30 N/m. These simulations were displacement-controlled wherein the driving longitudinal and circumferential displacements were determined from the experimental strains.

The objective function is given by:

$$\text{OBJ} = \text{MAPE} = \frac{1}{n}\sum_{t=1}^{n}\left|\frac{S_{exp,t} - S_{cmp,t}}{S_{exp,t}}\right| \qquad 5\text{-}7$$

where S_{exp} and S_{cmp} are the experimental and computational stresses, respectively, t denotes the data point and n is the total number of fitted data points. In the optimization process, $n = 32$ data points were utilized; 6 equidistant points in each direction from three loading protocols. Upper and lower bounds were set for the material parameters as illustrated in Table 5.2. These bounds enforced the constraints described in Eq. 5-6, i.e. Constraint 3 to 9.

Table 5.2: Bounds of material parameters applied in the optimization process.

Material parameter	Lower	Upper
b_{1111}	0.01	200
b_{1122}	-100	100
b_{2222}	0.01	200
b_{1133}	-100	100
b_{2233}	-100	100
b_{3333}	0.01	200
b_{1212}	0.01	200
b_{1313}	0.01	200
b_{2323}	0.01	200
c (kPa)	0.02	5

The flow chart of the optimization loops is shown in Figure 5.3. Initially, several sets of parameters (population) were defined. The set (member) contained an array of 10 values representing the material parameters. The member then underwent a series of tests to evaluate the violation of Constraint 1 (Eq.

5-4) and Constraint 2 (Eq. 5-5). If a violation was detected, the member was penalized by assigning an OBJ value according to the severity of the violation. Otherwise, the parameters values would be assigned to Fung material model in Abaqus to start the FE simulations.

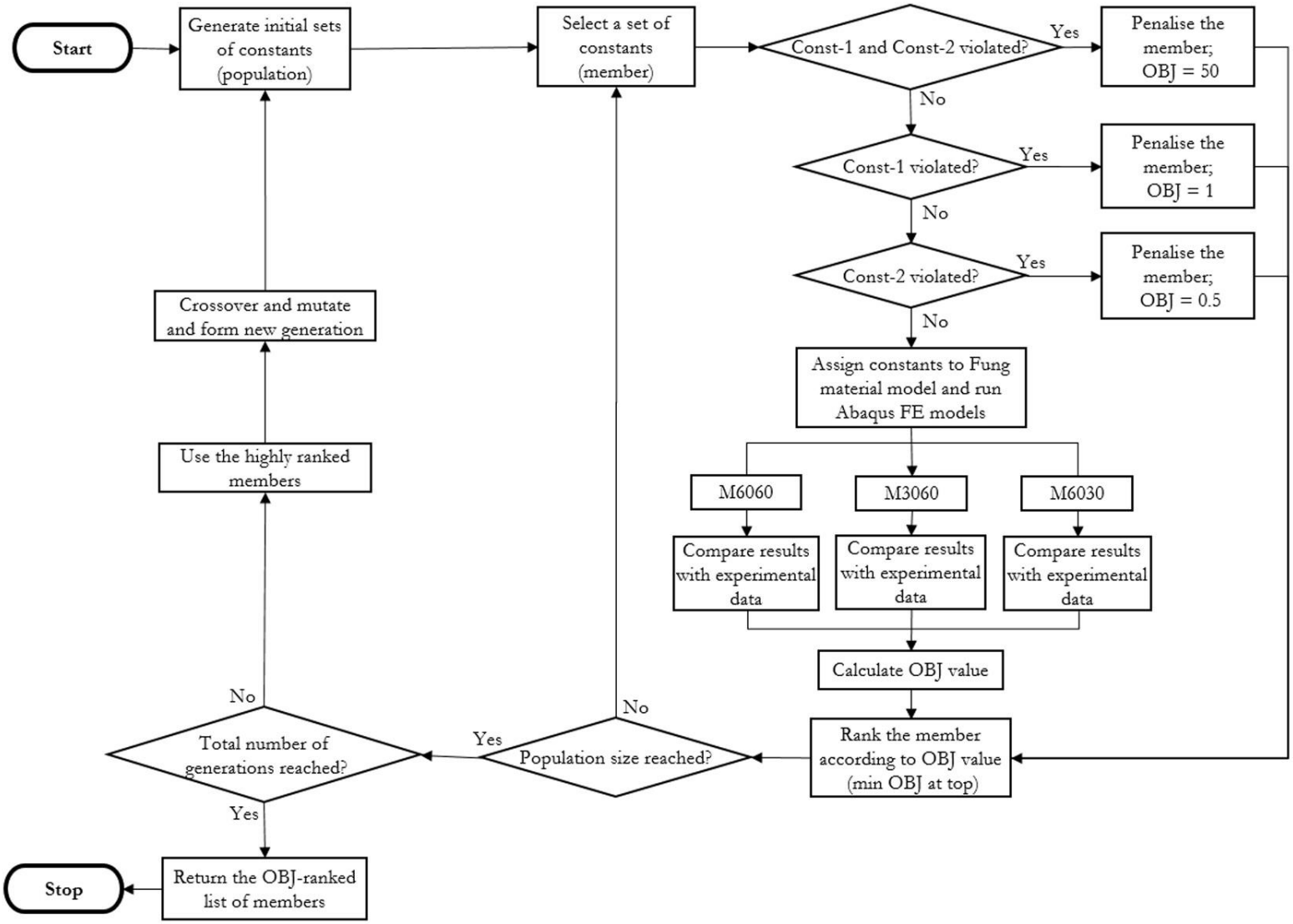

Figure 5.3: Flow chart of the SCILAB script utilized for optimization of material parameter. Const-1 = Constraint 1, Const-2 = Constraint 2. OBJ = objective function.

At completion of FE simulations, computational and experimental stresses were compared and the OBJ value was calculated. After that, the member was ranked in such a way that the lower the OBJ value was, the higher the rank would be. The next member in the population underwent the same process until all members were assigned OBJ value and ranked. Then, a new generation was formed. This was accomplished by subjecting the highly ranked members to crossover and mutation processes to generate new members. Crossover is the exchange of parameter values of two members (couple), while mutations are changes to a parameters value in a member (Yeoman 2004). The members of the new generation were ranked and a third generation was formed. The loop continued until the predefined number of generations was reached at which a list of the OBJ-ranked members was returned. The member with the smallest OBJ demonstrated the best fit. The GA predefined parameters were set as follows:

- Population size = 100; the number of members in a single generation (iteration).
- Number of generations = 10; equivalent to the number of iterations in the traditional optimization methods.
- Mutation probability = 0.5.
- Crossover probability = 0.7.
- Number of couples = 50; the number of member pairs (parents) in a population from which new members are formed through mutation and crossover.

5.2.5 Computation of stress and strain

The biaxial stress and strain were computed in SCILAB environment. Python script was utilized to extract the required results from the model output-database file.

The stress was computed based on the following equations:

$$S_{xx} = \frac{f_x}{l\,T} \tag{5-8}$$

$$S_{yy} = \frac{f_y}{l\,T} \tag{5-9}$$

where S_{xx}, f_x and S_{yy}, f_y are stress and force in the circumferential and longitudinal directions respectively, l is the model length and T is the model thickness. The values of l and T are known for different infarct models (Table 5.1). The values of f_x and f_y were captured from the predicted reaction forces at C7 and C8 (for f_x) and C5 and C6 (for f_y) (Figure 5.2) respectively.

The nodal strain was derived from the biaxial displacement of the four reference points (Figure 5.2). Cartesian coordinates of these points were captured at each increment of the quasi-static simulation. The equations governed the strain calculation was adopted from previous studies (Hoffman and Grigg 1984; Humphrey et al. 1987; Sacks 2000).

The nodal strain calculation is given by:

$$E_{xx} = \frac{\Delta u}{\Delta x} + \frac{1}{2}\left[\left(\frac{\Delta u}{\Delta x}\right)^2 + \left(\frac{\Delta v}{\Delta x}\right)^2\right] \quad 5\text{-}10$$

$$E_{yy} = \frac{\Delta v}{\Delta y} + \frac{1}{2}\left[\left(\frac{\Delta v}{\Delta y}\right)^2 + \left(\frac{\Delta u}{\Delta y}\right)^2\right] \quad 5\text{-}11$$

where E_{xx} and E_{yy} are the nodal strain, Δx and Δy are the change in nodal coordinates, and Δu and Δv are the change in nodal displacement in the circumferential and longitudinal directions, respectively.

5.2.6 Validation of stress-strain computation

The real-time biaxial loading force and displacement (x-y positions) of the optical markers were recorded as raw data by the biaxial device during experiment. These raw data were utilized to validate the stress and strain computing formulas described in section 5.2.5.

Raw data of 3 random samples were obtained. Biaxial stress and strain were computed for each sample using Eqs. 5-8 to 5-11. The validity of these equations was examined by comparing the computed stress-strain curves with the experimental curves.

5.2.7 Mesh refinement verification

The FE model underwent a mesh refinement study to evaluate the convergence of the numerical solution and to determine the optimum mesh density. Using global seeding, eight mesh densities were generated, as shown in Figure 5.4, utilizing linear hexahedral reduced-integration hybrid elements (C3D8RH). Table 5.3 shows the number of elements in each mesh.

Fung orthotropic model and material parameters of healthy myocardium, adopted from Omens et al. (1993), were utilized as shown in Table 5.4. Five transmural layers of fibres were defined; -50° at epicardium to 80° at the endocardium. The model was subjected to 10% equibiaxial stretch. Computational results and simulation time were compared between mesh densities.

Table 5.3: Number of elements generated for mesh convergence study.

Model	Mesh 1	Mesh 2	Mesh 3	Mesh 4	Mesh 5	Mesh 6	Mesh 7	Mesh 8
Number of elements	274	870	1896	2658	5985	10710	16597	29817

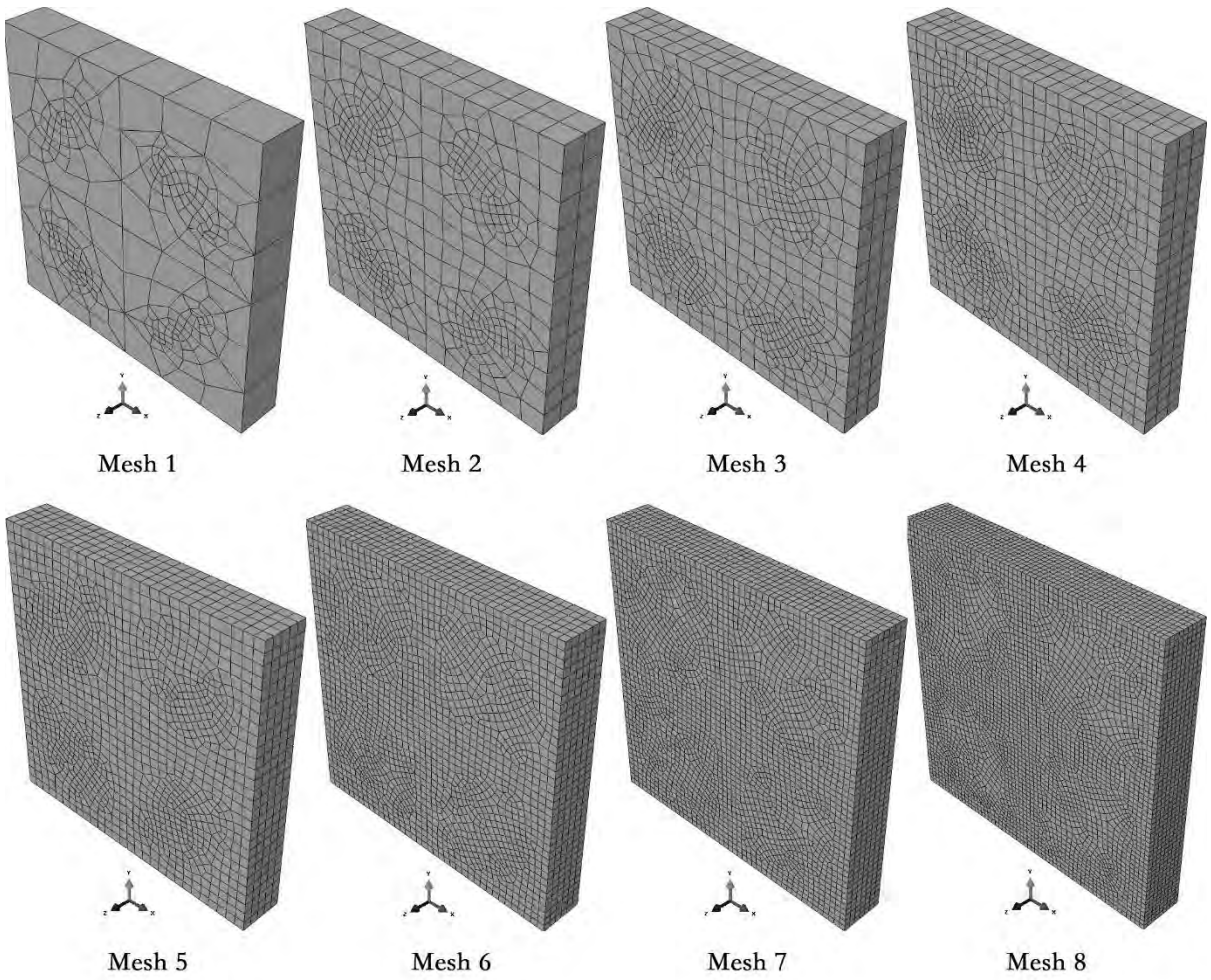

Figure 5.4: Different mesh densities of the biaxial tension model.

Table 5.4: Rat healthy myocardium material parameters, adopted from Omens et al.(1993), for Fung orthotropic model.

Material parameter	Value
b_{1111}	9.2
b_{1122}	0
b_{2222}	2
b_{1133}	0
b_{2233}	0
b_{3333}	2
b_{1212}	3.7
b_{1313}	3.7
b_{2323}	2
c (kPa)	1.1

5.2.8 Element type verification

Aiming at determining the suitable element type, the sensitivity of the FE model to different types of elements was examined. Four models were developed with four different element types and a unique mesh density (Mesh 3 in Figure 5.4). Element types include:

- Linear hexahedral reduced-integration hybrid elements (C3D8RH)
- Linear hexahedral full-integration hybrid elements (C3D8H)
- Quadratic hexahedral reduced-integration hybrid elements (C3D20RH)
- Quadratic hexahedral full-integration hybrid elements (C3D20H)

The material parameters shown in Table 5.4 were utilized. The models were subjected to 10% equibiaxial stretch and assigned 14 transmural layers of fibres. Stress-strain results and simulation time were compared between the models.

5.2.9 Sensitivity to density of fibre layers

The sensitivity of FE model to the density of the transmural fibre layers was studied in order to determine the optimum number of fibre layers to be incorporated in the model. It is important, however, to take into account the mesh density, particularly the number of transmural elements, since fibre angles are defined at element integration points (Abaqus 2012). The optimum FE mesh, as will be discussed later, was found to comprise 3 transmural elements. This mesh was utilized to develop 4 models in which 3, 5, 9 and 14 transmural fibre layers were defined respectively. A fifth

model with a fine mesh (14 transmural elements) and fibre layers (14 layers) was developed. A summary of models is presented in Table 5.5. All models were meshed using C3D8RH elements, assigned material parameters in Table 5.4 and subjected to 10% equibiaxial stretch. Biaxial stress-strain results and simulation time of the 3-element models were compared to the model with the fine mesh.

Table 5.5: Number of transmural elements vs. number of fibre layers in the models developed for evaluating the fibre-layers sensitivity study.

Model name*	No. of transmural elements	No. of fibre layers
3E-3F	3	3
3E-5F	3	5
3E-9F	3	9
3E-14F	3	14
14E-14F	14	14

* "E" and "F" in a model name denote "Element" and "Fibre layer" respectively.

5.3 Results

5.3.1 Validation of stress-strain computation

In Figure 5.5, the experimental biaxial stress-strain data is plotted together with the stress-strain data computed using Eqs. 5-8 to 5-11. The computational data fitted the experimental data very well for samples 1 and 2, Figure 5.5 (a, b). For sample 3, Figure 5.5 (c), a good fit was observed in the circumferential direction, however, the computationally predicted strain slightly underestimated the experimental strain in the longitudinal direction above ~15% of strain.

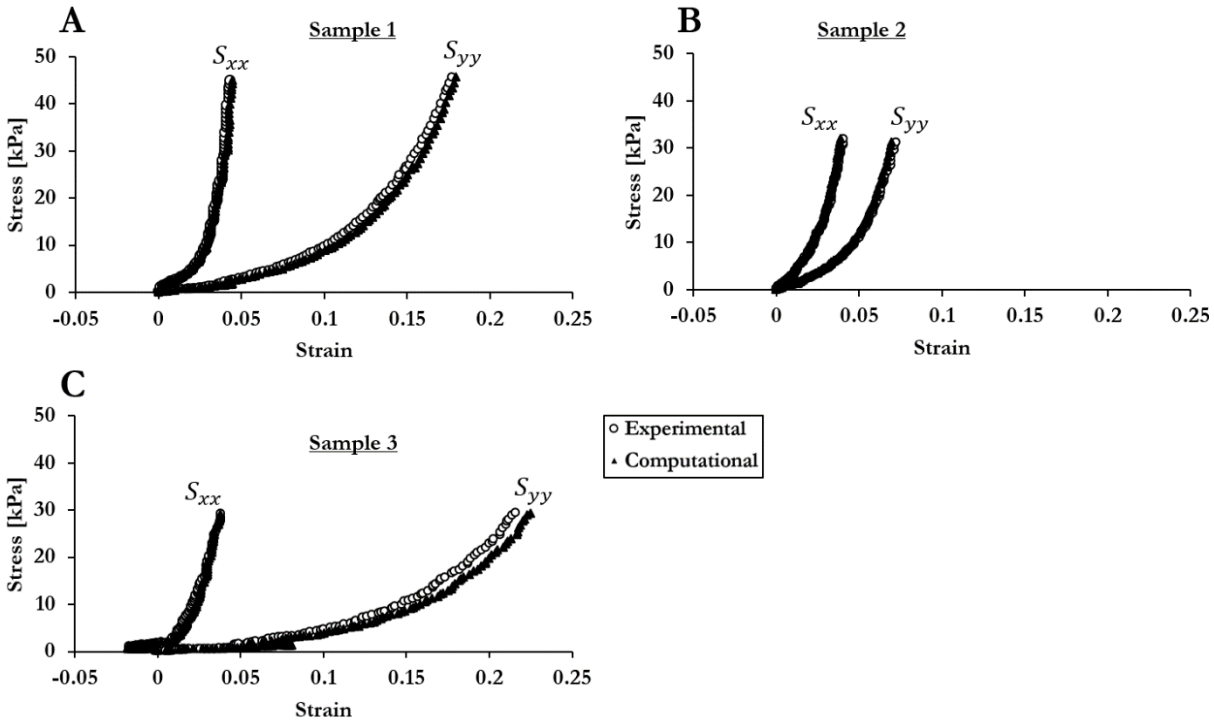

Figure 5.5: Experimental and computational biaxial stress-strain relationship in three samples: (a) Sample 1, (b) Sample 2 and (c) Sample 3. Computational stress and strain was calculated from raw experimental data of force and *x-y* positions of the optical markers.

5.3.2 Mesh refinement

The convergence of biaxial stress and strain with mesh refinement is illustrated in Figure 5.6. The peak numerical solutions from each mesh was normalized by the equivalent value from the coarse mesh (i.e. Mesh 1). The same circumferential strain (E_{xx}) was predicted by all mesh densities. Other numerical results converged at Mesh 3. Biaxial stresses, S_{xx} and S_{yy}, exhibited a slight fluctuation beyond Mesh 3, however, results from the finest mesh (Mesh 8) were comparable to Mesh 3. Comparing the simulation time, Mesh 3 consumed 97% less time than the Mesh 8 as illustrated in Table 5.6. As such, Mesh 3 was considered the optimum mesh density for the biaxial FE model.

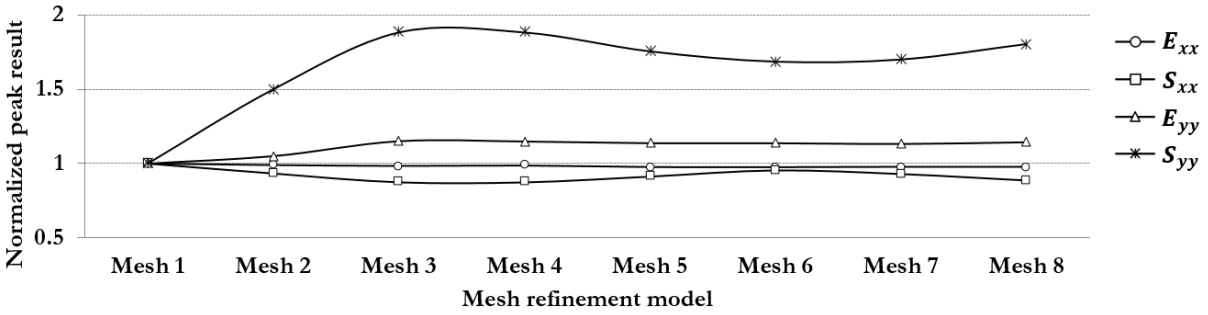

Figure 5.6: Convergence of numerical results with increasing mesh density.

Table 5.6: Simulation time consumed by different meshes.

Model	Mesh 1	Mesh 2	Mesh 3	Mesh 4	Mesh 5	Mesh 6	Mesh 7	Mesh 8
CPU time [sec]	4	16.4	26.6	68.1	94.2	219.7	417.6	785.1

5.3.3 Element type verification

Figure 5.7 shows the biaxial stress-strain relationship predicted by the FE model using different element types. A slight deviation between models was observed at higher strain, however, up to 5% strain all types of element predicted the same stress-strain data. This indicated that the numerical solutions were predictable by different element types within the strain range designated in this study. Comparing the computational cost between different element types, as illustrated in Table 5.7, C3D8RH showed the least simulation time. As such, C3D8RH was considered the optimal element type and utilized in the FE model.

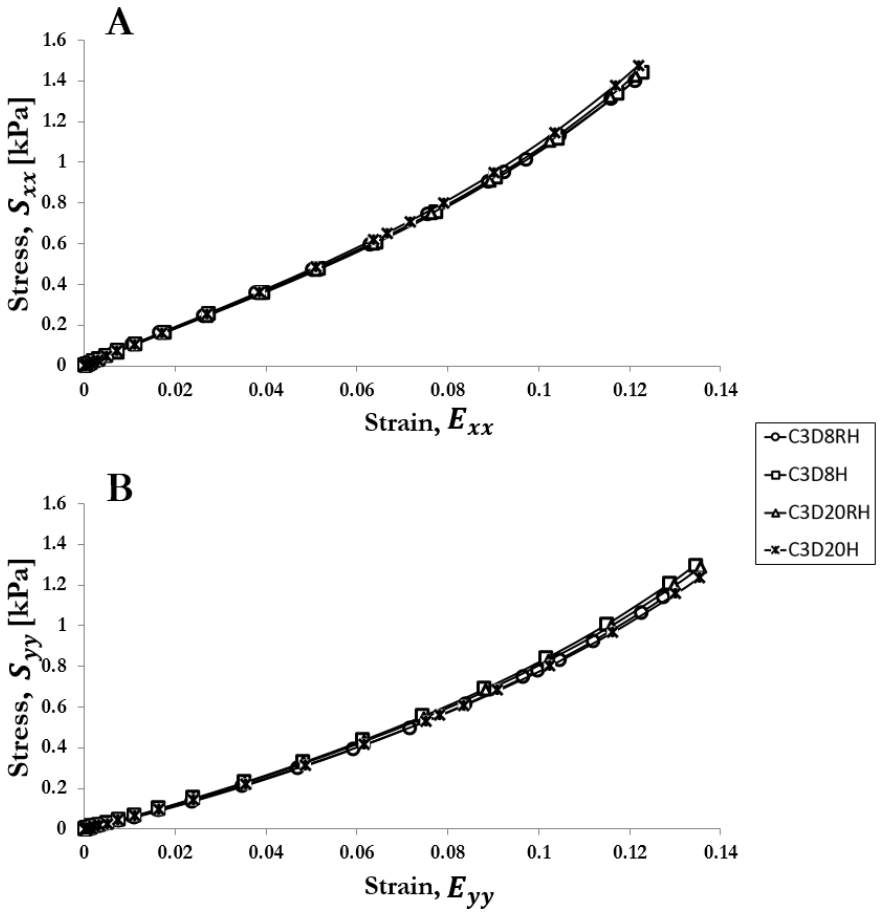

Figure 5.7: Stress-strain relationship in circumferential (a) and longitudinal (b) directions obtained from different types of elements.

Table 5.7: Simulation time of element verification models.

Model	C3D8RH	C3D8H	C3D20RH	C3D20H
CPU time [sec]	47.5	63.5	207.3	414.3

5.3.4 Sensitivity to density of fibre layers

The finest model in terms of the number of fibre layers and elements was 14E-14F. The numerical results predicted by this model were assumed to be the most accurate. Figure 5.8 shows a comparison between the biaxial stress-strain relationships predicted by the 3-element models (i.e. 3E-3F, -5F, -9F and -14F) and the one predicted by 14E-14F. The biaxial data predicted by 3E-3F and 3E-5F was identical and thus represented by a single curve for illustrative purposes. At low strains, the variation between the curves was minimal. As the strain exceeded ~8% the variation between different models became more distinct. The model that best fitted the 14E-14F stress-strain data was 3E-14F. Considering computational cost, changing the number of fibre layers had a small effect on the simulation time when the mesh density remained fixed as illustrated in Table 5.8. The 14E-14F model required 300-fold the time of 3E-14F. Hence, using 14 transmural layers of fibres was considered to be optimal when combined with Mesh 3.

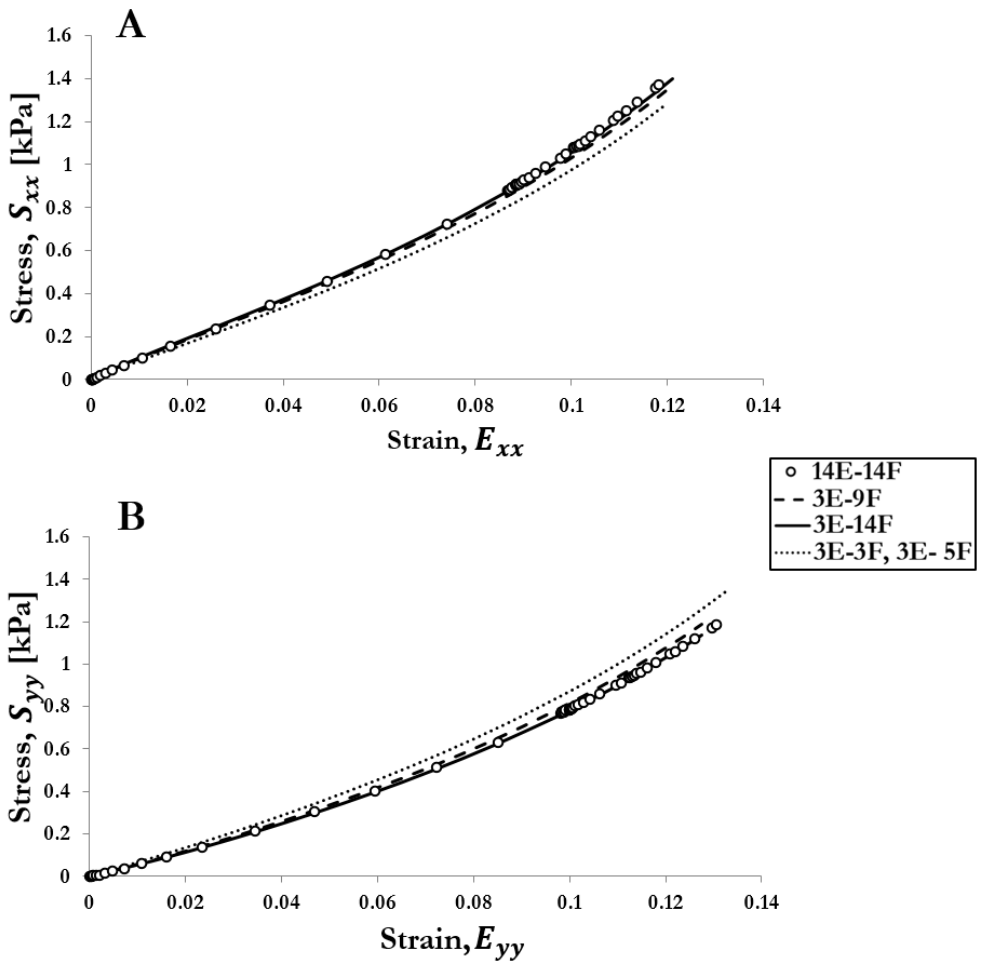

Figure 5.8: Stress-strain relationship in circumferential (a) and longitudinal (b) directions of selected models with different fibre layers and mesh densities.

Table 5.8: Simulation time of models used to study the sensitivity to fibre layers.

Model	3E-3F	3E-5F	3E-9F	3E-14F	14E-14F
CPU time [sec]	68.5	68.1	40	47.5	14221

5.3.5 Identified material parameters of infarcts

The identified Fung orthotropic material parameters for different infarct groups are shown in Table 5.9. The MAPE value represents the error between the experimental and computational data for the relative infarct group. The FE model predictions best approximated the experimental data of the 28d group with 3.0% error. The worst approximation was for the 7d group with 3.6% error.

Table 5.9: Identified Fung orthotropic material parameters for immediate, 7, 14 and 28 day infarcts. The MAPE value represents the mean absolute percentage error between the experimentally measured data and the fitted FE model predictions.

Material parameter	0d	7d	14d	28d
b_{1111}	64.31	176.09	16.38	159.65
b_{1122}	14.08	-70.92	-16.16	-25.52
b_{2222}	48.60	83.95	128.78	38.15
b_{1133}	20.51	81.15	-11.62	1.10
b_{2233}	-39.35	-84.99	-6.94	-31.44
b_{3333}	152.06	175.57	172.58	116.40
b_{1212}	68.31	176.54	77.86	18.56
b_{1313}	111.94	175.11	130.73	127.89
b_{2323}	63.54	158.40	189.56	65.77
c (kPa)	0.201	0.133	0.146	0.695
MAPE	0.032	0.036	0.032	0.030

Comparisons between the experimental data and the best fitted FE model results are shown in Figure 5.9, Figure 5.10, Figure 5.11 and Figure 5.12 for the immediate, 7d, 14d and 28d infarct groups, respectively. Most of the numerical predictions fell within the standard deviation tolerance of the experimental data for different infarcts. Mechanical coupling exhibited by the experimental data, indicated by the negative circumferential strains, at 30:60 loading protocol was well predicted by the FE model for all infarcts as illustrated in Figures 5.9-12 (c). With exception to the 28d group, FE models were not able to closely approximate the circumferential stress-strain data of the 60:30 protocol, Figures 5.9-12 (e).

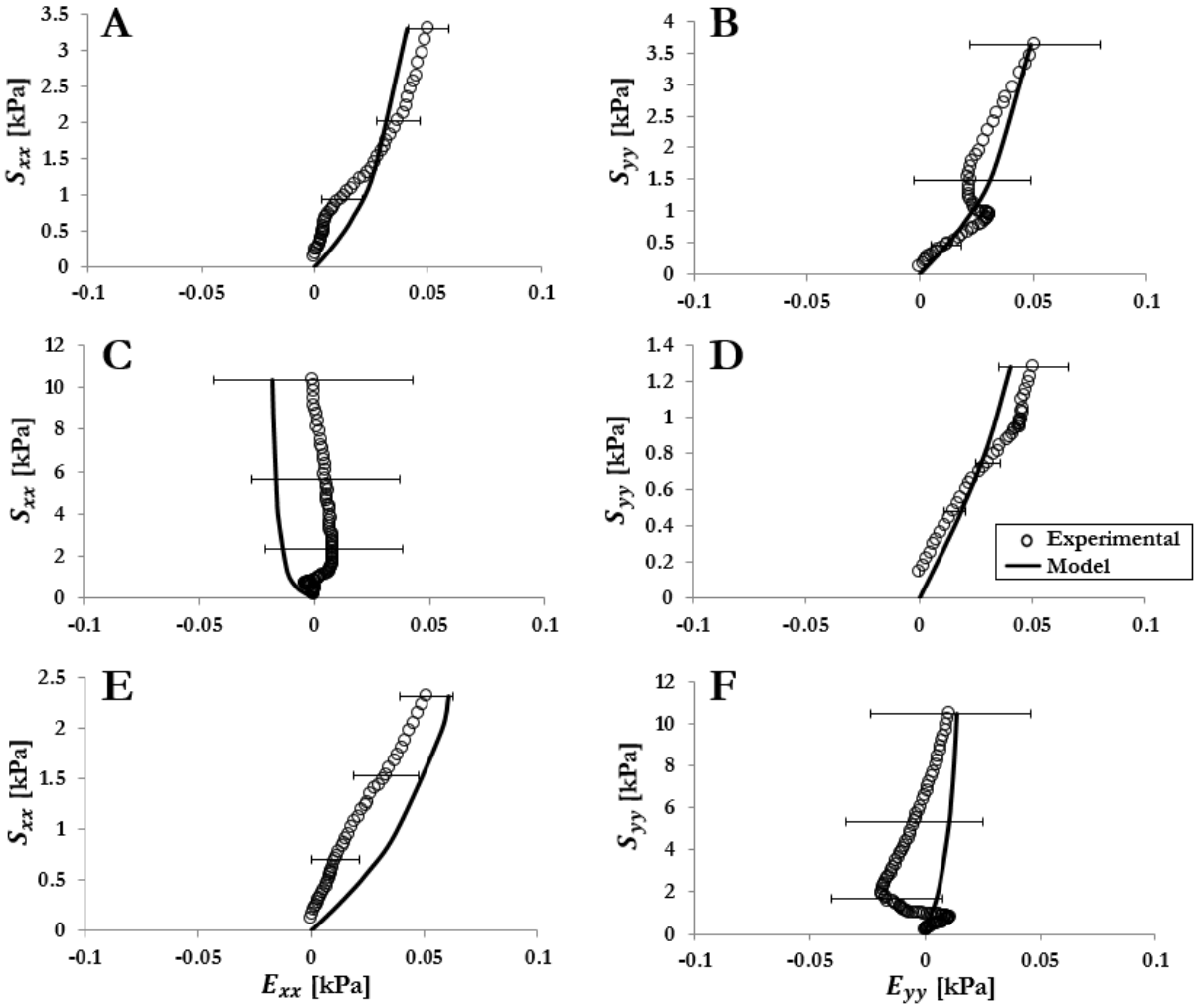

Figure 5.9: Best fit of FE model predictions to the experimental data for the immediate (0d) infarct group in each direction from three loading protocol. Stress axes are shown at variable range. Error bars represent the standard deviation. (a) Circumferential direction from 60:60 N/m protocol. (b) Longitudinal direction from 60:60 N/m protocol. (c) Circumferential direction from 30:60 N/m protocol. (d) Longitudinal direction from 30:60 N/m protocol. (e) Circumferential direction from 60:30 N/m protocol. (f) Longitudinal direction from 60:30 N/m protocol.

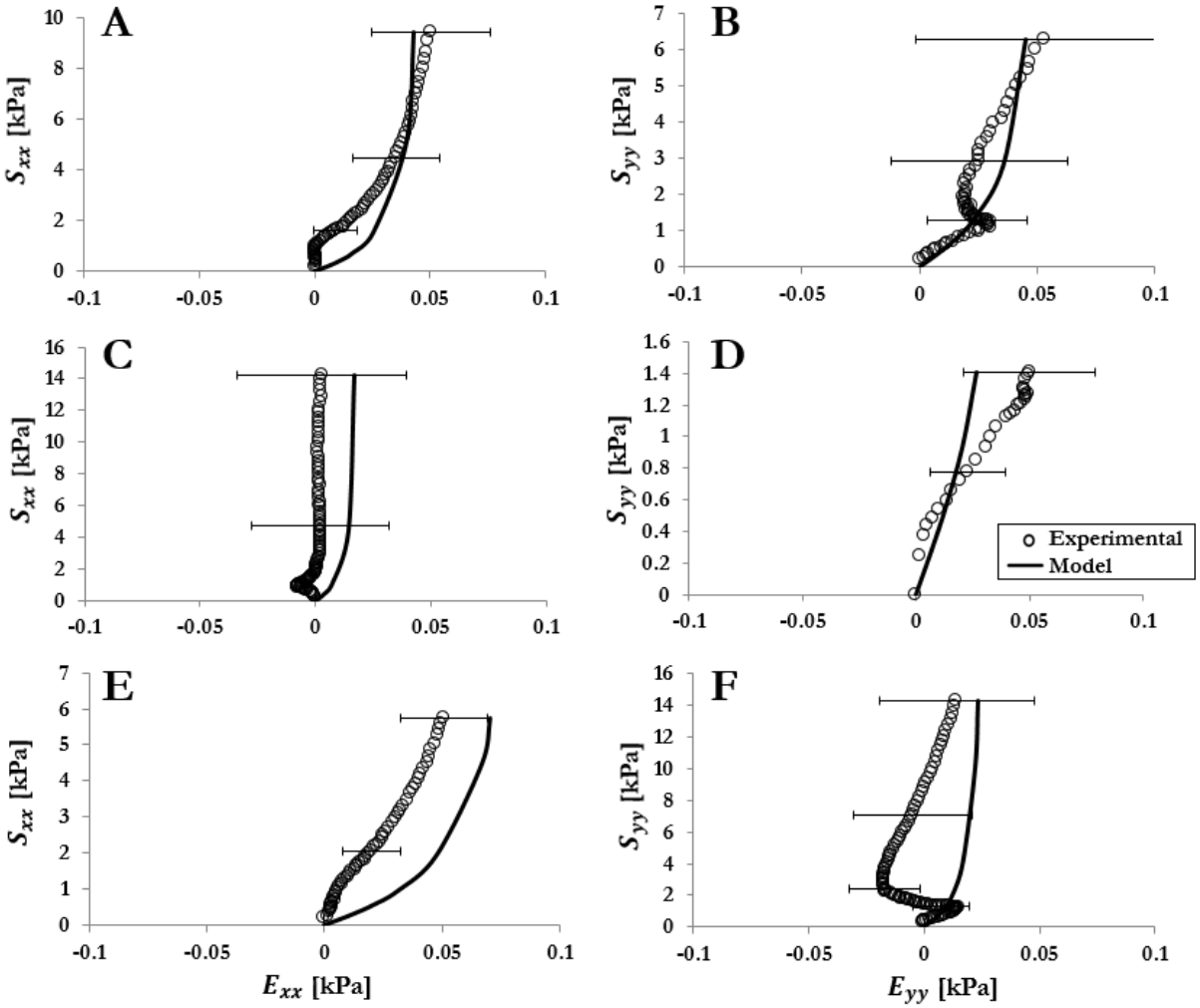

Figure 5.10: Best fit of FE model predictions to the experimental data for the 7d infarct group in each direction from three loading protocol. Stress axes are shown at variable range. Error bars represent the standard deviation. (a) Circumferential direction from 60:60 N/m protocol. (b) Longitudinal direction from 60:60 N/m protocol. (c) Circumferential direction from 30:60 N/m protocol. (d) Longitudinal direction from 30:60 N/m protocol. (e) Circumferential direction from 60:30 N/m protocol. (f) Longitudinal direction from 60:30 N/m protocol.

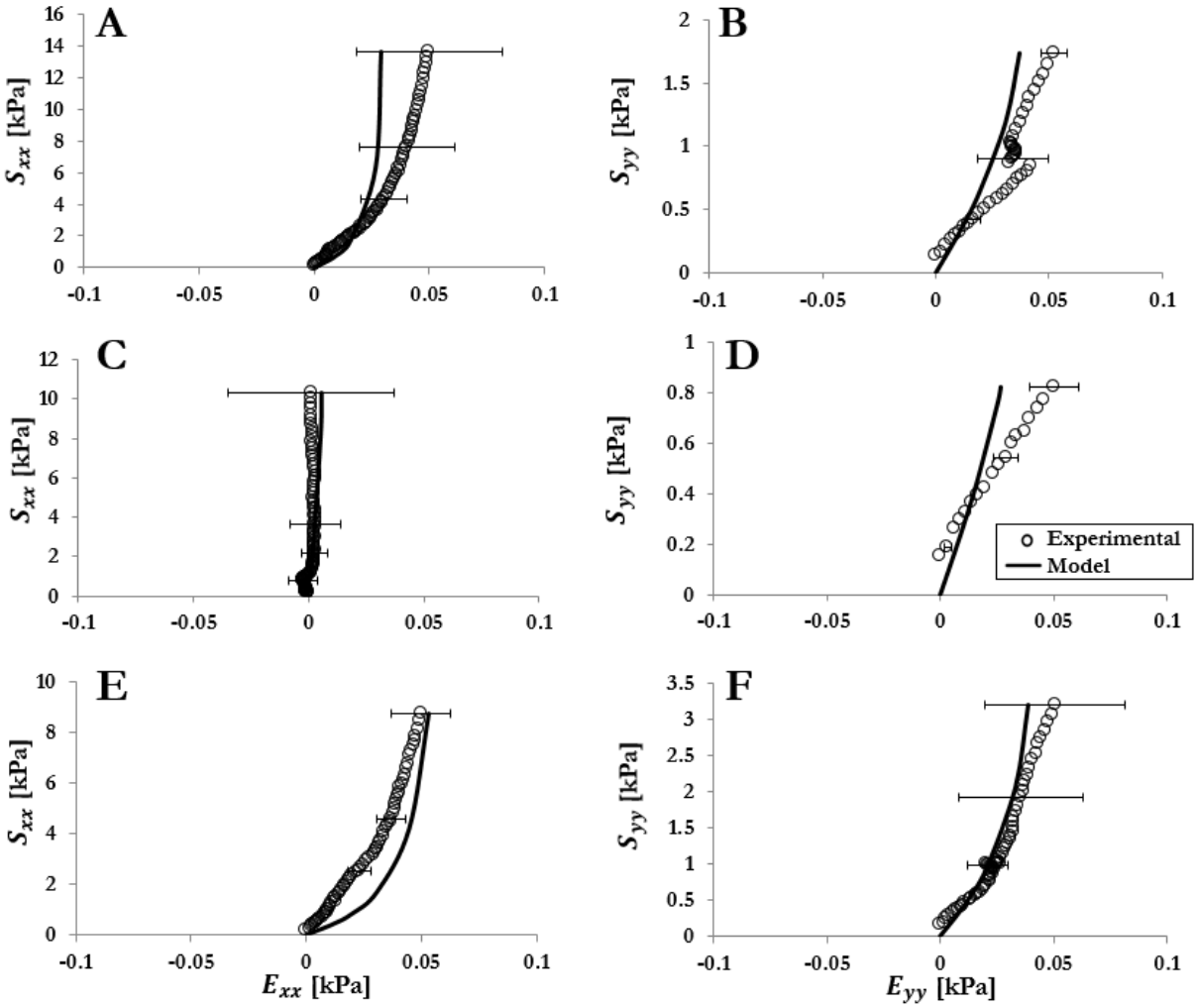

Figure 5.11: Best fit of FE model predictions to the experimental data for the 14d infarct group in each direction from three loading protocol. Stress axes are shown at variable range. Error bars represent the standard deviation. (a) Circumferential direction from 60:60 N/m protocol. (b) Longitudinal direction from 60:60 N/m protocol. (c) Circumferential direction from 30:60 N/m protocol. (d) Longitudinal direction from 30:60 N/m protocol. (e) Circumferential direction from 60:30 N/m protocol. (f) Longitudinal direction from 60:30 N/m protocol.

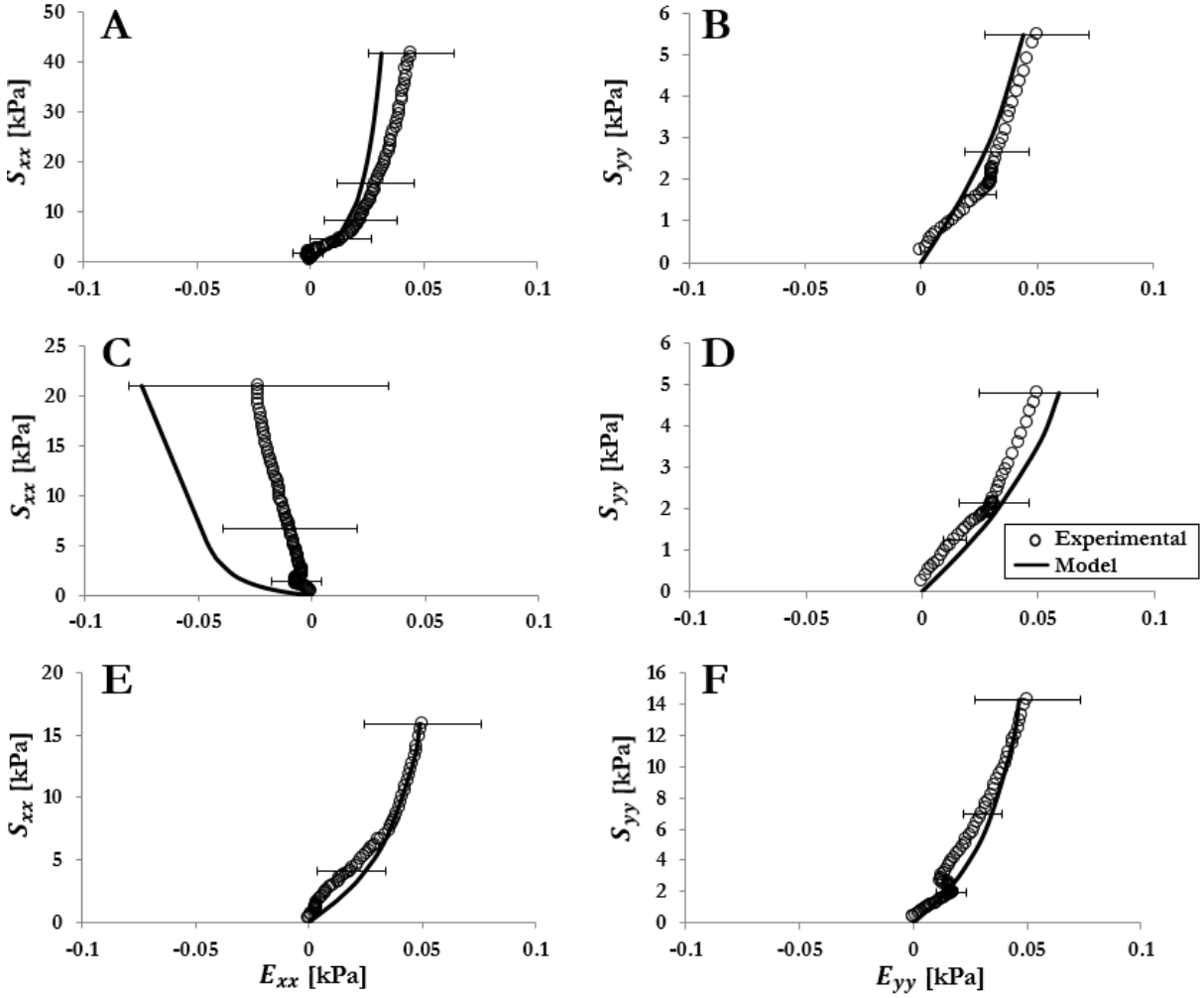

Figure 5.12: Best fit of FE model predictions to the experimental data for the 28d infarct group in each direction from three loading protocol. Stress axes are shown at variable range. Error bars represent the standard deviation. (a) Circumferential direction from 60:60 N/m protocol. (b) Longitudinal direction from 60:60 N/m protocol. (c) Circumferential direction from 30:60 N/m protocol. (d) Longitudinal direction from 30:60 N/m protocol. (e) Circumferential direction from 60:30 N/m protocol. (f) Longitudinal direction from 60:30 N/m protocol.

5.4 Discussion

In this study, an inverse approach was applied to identify material parameters of the orthotropic case of Fung constitutive law for healing infarcts. Utilizing the mechanical data presented in Chapter 4, FE models were developed and numerical solutions were fitted to the experimental data through GA-based optimization of the material parameters. The material parameters identified in this study will provide a new tool for FE investigation of MI mechanics based on rat models.

5.4.1 Model development

The 3D model was developed using the full geometry of the tissue sample. Partial geometries in conjunction with symmetric boundary conditions were not applicable in this study because of the anisotropy of the infarct. Stretching the model using 2 cylinders in each direction while constraining the movement of the 2 opposite cylinders produced uniform stress field in the central target area as illustrated in Figure 5.13. The locations of the reference points (black dots) were far enough from the areas of high stress concentration near the needles. This confirms that the model did not predict false strains due to the improper deformation of the sample (Sun et al. 2005).

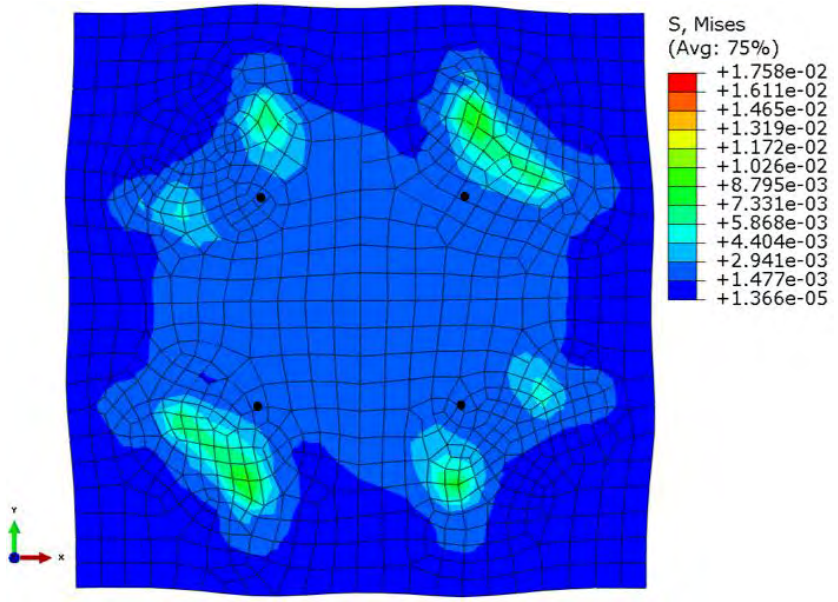

Figure 5.13: Von Mises stress (MPa) distribution in a fully deformed biaxial FE model illustrating the uniform stress field in the central target area. Locations of reference points are indicated by black dots.

5.4.2 Model validation and verification tests

The FE model was validated by examining its capability to computationally reproduce the experimental stress-strain data of three samples utilizing the real-time force and markers displacement recorded by the biaxial testing system. Stress and strain were computed using Eqs. 5-8 to 5-11. The computational data perfectly fitted the experimental data in two samples, Figure 5.5 (a, b). However, the computed longitudinal strain in the third sample underestimated the experimental strain above ~15%. This error was considered minor since the FE model solution was aimed to fit the experimental data for up to 5% of biaxial strain, as described in section 5.2.4. Therefore, it was confirmed that the experimental data obtained from the biaxial testing system and the computational data predicted by the FE model were developed using the same approach.

This was important to prevent possible errors from the mismatch between the two methods which would affect the accuracy of the optimized material parameters.

A single iteration in the optimization process of the material parameters included three simulations; M6060, M3060 and M60:30 (Figure 5.3). The optimization process could reach 1000 loops. As such, the computational cost is an important factor in this study since up to 3000 simulations may run to optimize the material parameters of a single infarct group. The mesh density, element type and fibre orientation are model attributes which influence the predicted numerical solution as well as the computational cost of the model. Therefore, the FE model underwent verification tests to choose the optimum mesh density, element type and density of fibre layers taking into account the computational cost.

Using 1896 elements in Mesh 3 (Figure 5.6) was found to produce, in a significantly less cost, numerical results that are comparable to the finest mesh (Mesh 8) which contained 29817 elements. The model exhibited insensitivity to elements type suggesting that the simulation time was the only considered aspect for choosing the optimal element type.

One limitation of the developed model was the utilization of a generic muscle fibre orientation, obtained from literature (Chen et al. 2003), to model the material orientation in the infarcts. Although this approach can be valid for the immediate (0d) infarct due to the presence of the muscle fibres (Holmes et al. 2005), it may not be appropriate for the other healing stages of infarcts (i.e. 7d, 14d and 28d) since the orientation of collagen fibres is possibly different. Also using unique fibre orientation for all the simulations ignored the change in fibre orientations observed for the different stages of infarct healing. Ideally, the orientations of collagen fibres in different infarct groups should have been measured and incorporated in the model. Since this was not feasible, a generic muscle fibre orientation was employed.

The fibre orientation was defined through 14 transmural layers linearly varied from -50° at the epicardial layer and 80° at the endocardial layer. In a single fibre layer, the fibres were assumed to have a unique angle, i.e. no in-plane change in angle. Reduced integrated elements contain one centroid integration point. The optimum mesh of the model comprised 3 transmural elements indicating that 3 fibre angles will be assigned. The study of refining the fibre layers suggested that the FE model was insensitive to change in fibre density at low biaxial strains. Additionally, combining the computationally inexpensive optimum mesh with 14 fibre layers delivered the same data as obtained with a very fine 14-element mesh. Consequently, the FE model utilized for the optimization of material parameters comprised 14 transmural fibre layers.

5.4.3 Identification of Fung material parameters

It has been discussed that myocardium may have orthotropic structure and that orthotropic constitutive models better describe the mechanical behaviour of myocardium than transversely anisotropic models (Usyk et al. 2000; Costa et al. 2001; LeGrice et al. 2001). In the present study, an orthotropic constitutive law was used to model the mechanical properties of the different infarct stages.

One difficulty in optimizing the material parameters in this model was the positive definiteness condition of the parameter matrix (Eq. 5-3) in the unloaded state. The fulfilment of the constraints described in Eqs. 5-4 and 5-5 adds more complexity to the definition of the optimization process. In the present study, such constraints were not included in the GA. Instead, it was verified that the generated sets of parameters satisfied the positive definiteness condition. A similar approach was applied by Wang et al. (2006). In a generation, random sets of material parameters are defined by the GA. It is required to test these sets for violation of the constraints before they are passed to the model. A pilot study suggested that eliminating an entire violating set was not always a good approach since such violation can sometimes be treated, for example, by adjusting the value of a single parameter in the set. Following several trials, an approach of classifying these sets according to the violation severity was introduced. The set that violates Constraints 1 and 2 is the worst and therefore penalized using a relatively large OBJ value (OBJ=50). If only Const-1 is violated, the set is penalized with less OBJ value (OBJ=1). Similarly, if only Constraint 2 is violated, the set is penalized with OBJ=0.5. Penalizing the undesired sets will rank them at the bottom of the list so that they are not included in the formation of the next generation. This way the GA is biased in the definition of the new generation. As a result, the violation disappeared in most of the newly formed sets of parameters at the 4^{th} or 5^{th} generation. In spite of its simplicity, this approach worked very well for the current study.

A shortcoming of the current study was the employment of biaxial data to fit material parameters of orthotropic material law. The negative values in some of the identified parameters, e.g. b_{1122} and b_{2233}, did not make good physical sense and indicated "overfitting". In other words, the biaxial tests were not able to provide sufficient data to fit all the parameters of the orthotropic constitutive law. Holzapfel and Ogden (2009) discussed the limitation of using biaxial data alone to fit orthotropic constitutive law. They emphasized the need for more comprehensive mechanical

characterization which include shear data at different orientation in order to appropriately capture the orthotropic behaviour of myocardial tissue.

6 Micromechanics of biomaterial injectate and infarcted myocardium during diastole: Finite element investigation

6.1 Introduction

Injection of biomaterial into the infarcted ventricular wall is an evolving therapy for myocardial infarction (MI). Biological (Dai et al. 2005) and synthetic (Kadner et al. 2012) materials have shown beneficial outcomes; preventing the expansion of the infarct and limiting the adverse ventricular remodelling. Such beneficial outcome is attributed to the mechanical support of the damaged tissue by the injected material (Wall et al. 2006). In addition to the mechanical support, biomaterial injectates can be utilized as carriers for the delivery of stem cells and growth factors aiming at restoring the contractility in the injured myocardium (Lu et al. 2009; Ruvinov et al. 2011; Singelyn and Christman 2011) and cardioprotection of the infarcted heart through paracrine signalling (Uemura et al. 2006; Mirotsou et al. 2007).

Preclinical research has been devoted to understand the underlying mechanics of the acellular biomaterial injectate MI therapy. Morita et al. (2011) injected tissue filler material into infarcted sheep hearts. Observing an improved infarct expansion and remodelling at 8 weeks after infarction, they claimed that infarct thickening and stiffening was beneficial and achievable through biomaterial injection. Ifkovits et al. (2010) investigated the impact of injecting two hyaluronic acid hydrogels with 8 and 43 kPa moduli on the remodelling response of ovine MI model. They found that the higher modulus hydrogel was superior in terms of functional outcomes and infarct expansion. Kichula et al. (2014) utilized biaxial testing to demonstrate the anisotropic stiffening of the tissue/hydrogel composite region when hydrogel was injected into ovine hearts in vitro. A finite element (FE) model of acute MI showed a decreasing wall myofibre stresses with increasing composite stiffness. This study revealed the importance of optimizing the injectate properties.

FE approaches have been applied in the investigation of biomaterial injection therapy for MI. Wenk et al. (2009) utilized FE models with analytical approach to estimate the optimum patterns of injections based on minimizing myofibre stresses and maximizing stroke volume. Kortsmit et al. (2013; 2013b) developed FE models of canine hearts to study the effect of the hydrogel injectate on the healing infarct taking into account different hydrogel geometries.

The mechanical investigations of MI biomaterial-injectate therapy presented in literature focused on the "macroscopic" level of the problem. In the current study, an insight is provided into the micromechanics of a hydrogel injectate in the infarct zone during the diastolic filling of a rat left ventricle (LV). A FE end-systolic LV model was developed from cardiac magnetic resonance (CMR) image data. Increasing intraventricular pressure was applied to simulate the passive filling. The deformation of a small hexahedral volume in the anterior midwall region, referred to as block, of the healthy LV was measured. Assuming a block of the same dimensions comprising infarcted tissue and interleaved gel injectate (referred to as composite), the micromechanics of biomaterial injectate and infarcted tissue was investigated. Infarct-gel composites of the same geometrical distribution but different material properties of both tissue and gel were studied utilizing 7 and 28 day infarcts in conjunction with 3 gels of different stiffness. The geometrical model of the infarct-gel composite block was developed from histological micrographs using the approach described in Chapter 3 while utilizing the infarct material parameters identified in Chapter 5.

6.2 Materials and methods

6.2.1 Left ventricular model

A FE model was developed to simulate diastolic filling of a healthy rat LV. This model provided the mechanical domain wherein the micromechanics of biomaterial injectate was aimed to be studied. The diastolic passive filling was modelled by applying an increasing pressure to the endocardium of an end-systolic (ES) LV geometry until a predefined end-diastolic (ED) cavity volume was reached.

An ES geometry of a LV was reconstructed using the approach and CMR image data previously presented in Chapter 3. In brief, CMR image data of a healthy rat heart was obtained using a custom built small animal coil in a 3.0T Magnetic Resonance Imaging (MRI) system. An ES short-axis CMR image stack was imported in Simpleware (Simpleware Ltd., Exeter, UK). A special mask was applied to segment the LV in each slice. By stacking the masks, a 3D geometry of the LV was

developed. The model was meshed using linear tetrahedral reduced-integration hybrid elements (C3D4H) as shown in Figure 6.1 (a).

The model was imported in Abaqus CAE 6.12-2 (Dassault Systèmes, Providence, RI, USA) for FE analysis. Fung orthotropic model and material parameters of healthy myocardium, adopted from Omens et al. (1993), were utilized as shown in Table 6.1.

Table 6.1: Rat healthy myocardium material parameters, adopted from Omens et al.(1993), for Fung orthotropic material model.

Material parameters	Value
b_{1111}	9.2
b_{1122}	0
b_{2222}	2
b_{1133}	0
b_{2233}	0
b_{3333}	2
b_{1212}	3.7
b_{1313}	3.7
b_{2323}	2
c (kPa)	1.1

The orientation of myofibres was incorporated in the LV model using a user-defined material orientation subroutine (ORIENT) in Abaqus. The subroutine was utilized to define fibre orientation through 5 transmural layers of fibre angles. The fibre angles ranged linearly from -50° at the epicardial layer to 80° at the endocardial layer (Chen et al. 2003). At the apex, the fibres were oriented circumferentially i.e. assigned 0° angle. At the interface between the apex and proximal region of the LV, the epicardial and endocardial layers were assigned -25° and 40° respectively. These midpoint angles were introduced to achieve the spiral orientation of fibres observed in a rat heart (Hautemann 2007).

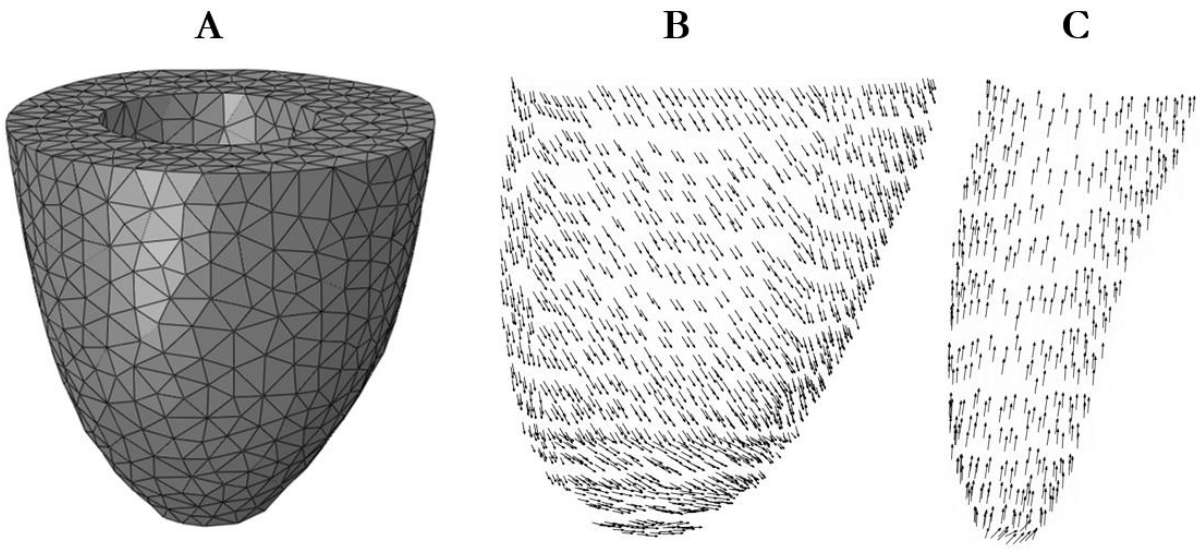

Figure 6.1: Left ventricle end-systolic model. (a) The finite element mesh. (b) Fibre orientation at the epicardial layer. (c) Fibre orientation at the endocardial layer.

To apply boundary conditions, a cylindrical coordinate system (r-θ-z) was introduced in the model where r, θ and z represented the radial, circumferential and longitudinal axes respectively. Displacement boundary conditions were applied to the entire base surface of the LV. The displacement of the surface nodes was constrained in the circumferential and longitudinal directions allowing a movement in the radial direction only.

The ES LV model was loaded by applying a pressure to the endocardial surface. The pressure was linearly increased until the LV cavity volume matched a target value. This target value represented the ED cavity volume which was measured from the CMR data using a specialized cardiovascular image analysis software; Segment v1.8 R1021 (Heiberg et al. 2010). The target ED volume was 170 µl and was obtained by the model at ED pressure of 21 mmHg (2.8 kPa).

6.2.2 Prediction of microscopic deformation in the anterior wall

During diastolic filling of the LV, the deformation of a small anterior midwall tissue volume was recorded and represented in forms of normal and shear strains. This small volume henceforth will be referred to as "block".

A block with dimensions ~300×300×300 µm was developed, meshed using linear hexahedral reduced-integration hybrid elements (C3D8RH) and assigned the healthy myocardium material model in Table 6.1. The block was embedded in the LV midwall as illustrated in Figure 6.2. Embedded region constraint (Abaqus 2012) was applied to the block so that the response of the

LV elements constrained the translational degrees of freedom of the block nodes. The elements were assigned the local fibre orientation based on the position of the block within the LV wall.

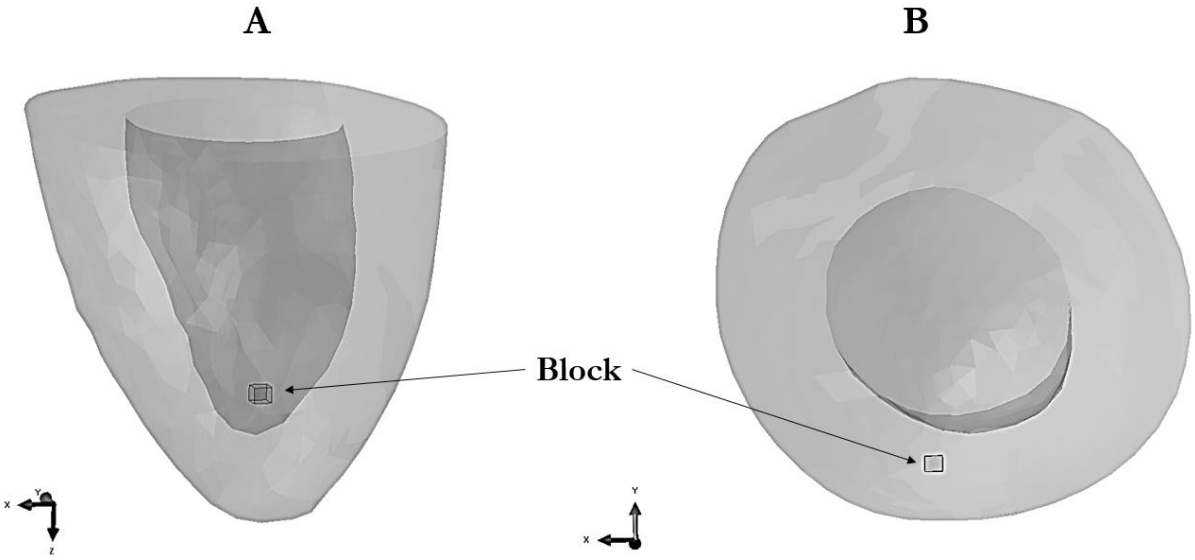

Figure 6.2: Anterior (a) and superior (b) views of the left ventricle model showing the location of the analytical block used to study the microscopic deformation in the anterior wall during diastolic filling. The model is partially translucent for illustration purposes.

The deformation of the block was determined by capturing and analysing the local displacements of its surfaces. This was implemented by defining a reference point in the centre of each face of the block and by defining a local Cartesian coordinate system at one corner as shown in Figure 6.3 (a). The reference points were tied to their surfaces using tie constraints (Abaqus 2012). The local coordinate system was defined as a movable system following the corner so as to omit the rigid body displacement of the block. The coordinate system was oriented so that the positive x, y and z directions were in the circumferential, radial and longitudinal directions of the LV. The x, y and z components of a reference point displacement, and thus the surface, were captured during diastolic filling and analysed to quantify the block deformation. The deformation was represented in form of normal (E_{xx} , E_{yy} , E_{zz}) and shear (E_{xy} , E_{yx} , E_{zx} , E_{xz} , E_{yz} , E_{zy}) strains calculated by normalizing the displacement (Δx , Δy , Δz) by the respective block dimension (x , y , z) as illustrated in Figure 6.3 (b).

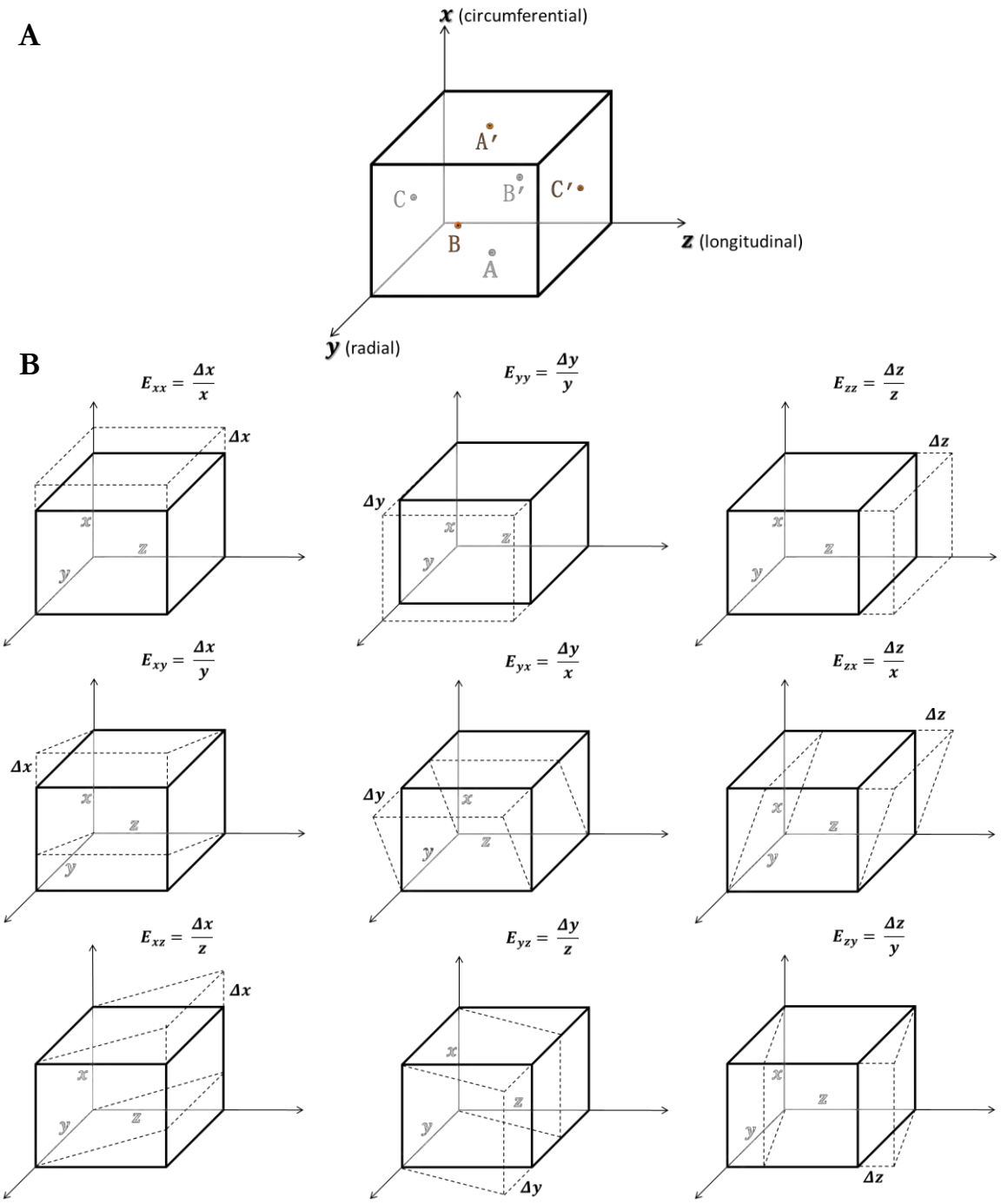

Figure 6.3: (a) Diagram of the block showing the predefined reference points and the local coordinate system. (b) The different forms of strains calculated from surface displacement of the block through normalizing the displacement (Δx, Δy, Δz) by the respective block dimension (x, y, z).

6.2.3 Infarct-gel composite block model

A block model containing a composite of infarcted tissue and hydrogel was developed to study the micromechanics of biomaterial injectate during diastolic filling of the LV. Different infarct-gel composites were studied utilizing 7 and 28 day infarcts in conjunction with 3 gels of different stiffness.

The geometry of the infarct-gel composite block was developed from the histological micrographs of polyethylene glycol (PEG) gel using the approach previously described in Chapter 3. In brief, MI was induced in a rat heart followed by injection of PEG gel. The heart was harvested, sectioned at ~300 μm on a cryostat and mounted using DAPI mount. Images of the sections were acquired using an Eclipse 90i Fluorescent Microscope with digital camera. Assuming a uniform shape of tissue and gel within a longitudinal extension of 300 μm, copies of a single image were imported in Simpleware to reconstruct a 300 μm thick block. As demonstrated in Figure 6.4 (a, b), tissue and gel were segmented within a square field using red and blue spatial masks, respectively. The 3D geometry of the tissue-gel composite was reconstructed and meshed as shown in Figure 6.4 (c). The mesh was composed of a mixture of 5336 linear hexahedral (C3D8RH) and 65467 linear tetrahedral (C3D4H) reduced-integration hybrid elements. The block volume was 0.031 mm^3 (0.0159 mm^3 tissue; 0.0151 mm^3 gel). The tissue and gel sections were identified as separate element sets in the continuum of the block, i.e. allowing no slip between the two materials.

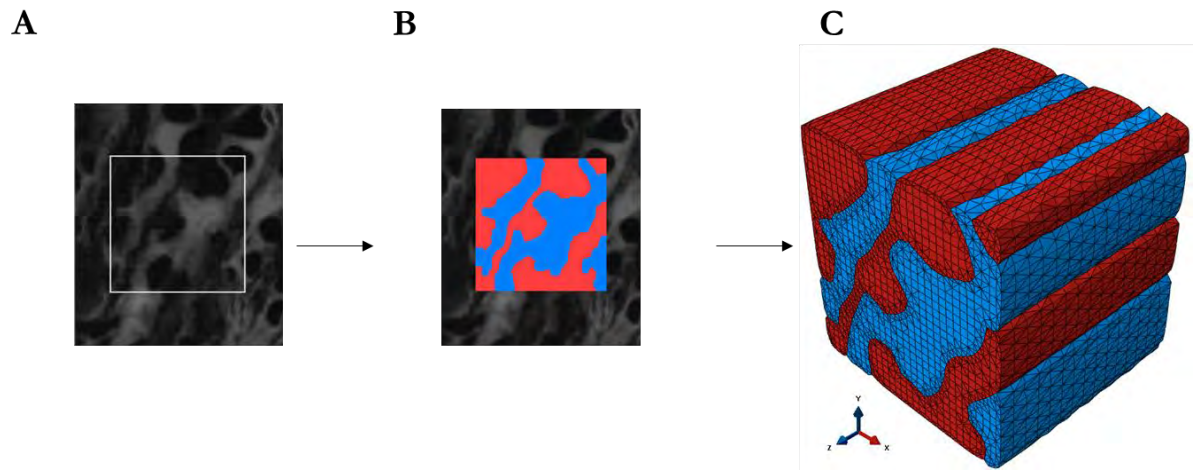

Figure 6.4: Development of tissue-gel composite block model. (a) Greyscale histology image from which tissue and gel were segmented. Gel appears white. Square indicates the segmented field. (b) Segmentation of tissue and gel. Tissue appears red and gel appears blue. (c) 3D developed mesh of the block.

The composite block mesh was imported in Abaqus. Different material models were assigned to element sets representing tissue and gel. Fung orthotropic material model was employed for the

tissue section utilizing material parameters identified in Chapter 5. The gel was modelled as Neo-Hookean isotropic hyperelastic material described in terms of strain energy function (W):

$$W = c_{10}(\bar{I}_1 - 3) \quad 6\text{-}1$$

where c_{10} is the material parameter and $\bar{I}_1$ is the first invariant of the left Cauchy-Green deformation tensor.

Different combinations of infarct and gel materials were utilized based on the 7d and 28d infarct properties and gels of different stiffness. Material parameters of 7d and 28d infarcts are shown in Table 6.2. For PEG hydrogel material, c_{10} was 12.3 kPa (Phelp 2012). Additional softer (c_{10} = 3 kPa) and stiffer (c_{10} = 20 kPa) gel materials were employed, denoted by G03 and G20 respectively. These material properties were chosen in order to account for very early and late phases of infarct healing and the variation in the stiffness of injectable biomaterials (Wall et al. 2006).

Table 6.2: Fung orthotropic material parameters for 7d and 28 day infarcts (adopted from Chapter 5).

Material parameter	7d	28d
b_{1111}	176.09	159.65
b_{1122}	-70.92	-25.52
b_{2222}	83.95	38.15
b_{1133}	81.15	1.10
b_{2233}	-84.99	-31.44
b_{3333}	175.57	116.40
b_{1212}	176.54	18.56
b_{1313}	175.11	127.89
b_{2323}	158.40	65.77
c (kPa)	0.133	0.695

For the purpose of comparison, block models of untreated (without biomaterial injectate) infarcted tissue were developed by assigning a single infarct material model to both sections of the block. However, predicted results were considered only from the element set representing the tissue section so that the comparison between tissue mechanics in different models was based on the same set of elements. Table 6.3 summarizes the different models.

Table 6.3: Summary of different models developed to study the micromechanics of of the biomaterial injectate.

Model Description	Model Symbol	Tissue Section Material	Gel Section Material
7 day infarct (untreated)	I	7d	7d
7 day infarct with soft gel	I-G03	7d	G03 (c_{10}= 3kPa)
7 day infarct with PEG gel	I-PEG	7d	PEG (c_{10}= 12.3kPa)
7 day infarct with stiff gel	I-G20	7d	G20 (c_{10}= 20kPa)
28 day infarct (untreated)	I	28d	28d
28 day infarct with soft gel	I-G03	28d	G03 (c_{10}= 3kPa)
28 day infarct with PEG gel	I-PEG	28d	PEG (c_{10}= 12.3kPa)
28 day infarct with stiff gel	I-G20	28d	G20 (c_{10}= 20kPa)

I = Infarct, G = Gel, d = day.

The deformation of the composite block associated with diastolic filling was simulated using the submodel approach (Abaqus 2012). The submodel is a modelling technique used to study in detail an area of interest in a model. It is based on simulating the deformation of a "global" coarse-mesh model. The output of this global model is then utilized to drive a fine-mesh "submodel" which forms a small region of the global model.

In the present study, the LV model represented the global model whereas the composite block formed the submodel (region of interest). The composite block was virtually positioned in the anterior midwall of the LV, in the fashion illustrated in Figure 6.2, and was assigned the local fibre orientation. The displacement output field from the LV model was utilized to define the displacement of the boundary nodes on the block model shown in Figure 6.5.

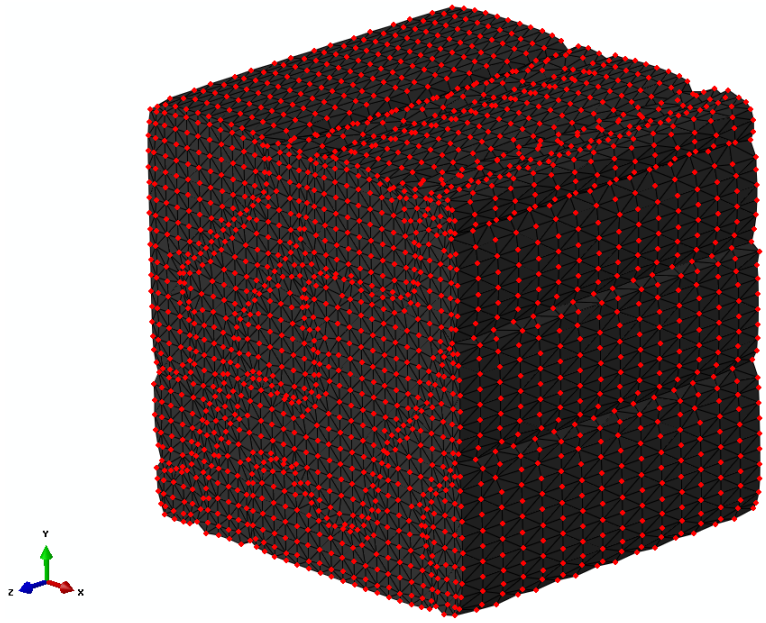

Figure 6.5: The boundary nodes of the composite block model.

Infarcted myocardium is stiffer than healthy myocardium. As such, infarcts deform to a lesser extent during cardiac cycle compared to healthy tissue. In our study, the displacement output field used to define the deformation of the untreated infarct and composite blocks was obtained from diastolic filling of a healthy LV. To account for the attenuation of deformation in infarcts and composites, these blocks were deformed up to 15% only of diastole phase. This fraction was estimated from in vivo strain measurements on healthy and infarcted hearts found in literature. The circumferential strain of rat infarcts could be reduced by up to 80-90% compared to healthy myocardium (Fomovsky and Holmes 2010). MRI tagging measurements on human subjects showed 86% average decrease in the circumferential strain of an infarct compared to healthy control myocardium (Bogaert et al. 2000). In reality, increasing the stiffness of the gel is expected to further decrease the deformation of treated region during cardiac cycle. However, this was not implemented in the current models to ensure consistency necessary in models inter-comparison.

Mean and maximum strain and stress predicted by tissue and gel sections in different models were compared. The calculation of mean and maximum results excluded elements with unrealistically extreme stress values caused by the boundary conditions, e.g. at marginal elements.

6.3 Results

6.3.1 Microstructural deformation in the anterior wall

The surface displacements of the tissue block in x, y and z directions during LV diastolic filling are shown in Figure 6.6. The displacements in y (radial) direction, Figure 6.6 (b), were the largest

compared to the other directions with a maximum ED displacement of 68 μm predicted for surface C`. The block surfaces exhibited relatively small displacements in $z$ (longitudinal) direction, Figure 6.6 (c), with a maximum of 14 μm predicted for surface C`. In x (circumferential) direction, Figure 6.6 (a), a maximum displacement of 40.5 μm was predicted for surface A`.

The strain components calculated from the relative displacement of block surfaces at the ED time point are shown in Table 6.4. Tensile deformation was predicted in the circumferential (i.e. E_{xx}) and longitudinal (i.e. E_{zz}) directions whereas compressive deformation was observed in the radial direction (i.e. E_{yy}). The maximum normal strain was E_{yy} = -10.93 % based on the relative displacement of surface B and B` in the radial direction. Similarly, the maximum shear strain was $E_{yz}$ = 20.46 % based on the relative displacement of surface C and C` in the radial direction. The minimum shear strain was E_{yz} = 0.96 and also predicted for C and C`, however, from their relative displacement in the circumferential direction.

Table 6.4: End-diastolic strain components predicted by analytical block in the anterior midwall of left ventricle.

ED Strain (%)		
E_{xx}	E_{yy}	E_{zz}
8.53	-10.93	4.61
E_{xy}	E_{yx}	E_{zx}
3.86	9.81	-3.54
E_{xz}	E_{yz}	E_{zy}
0.96	20.46	3.29

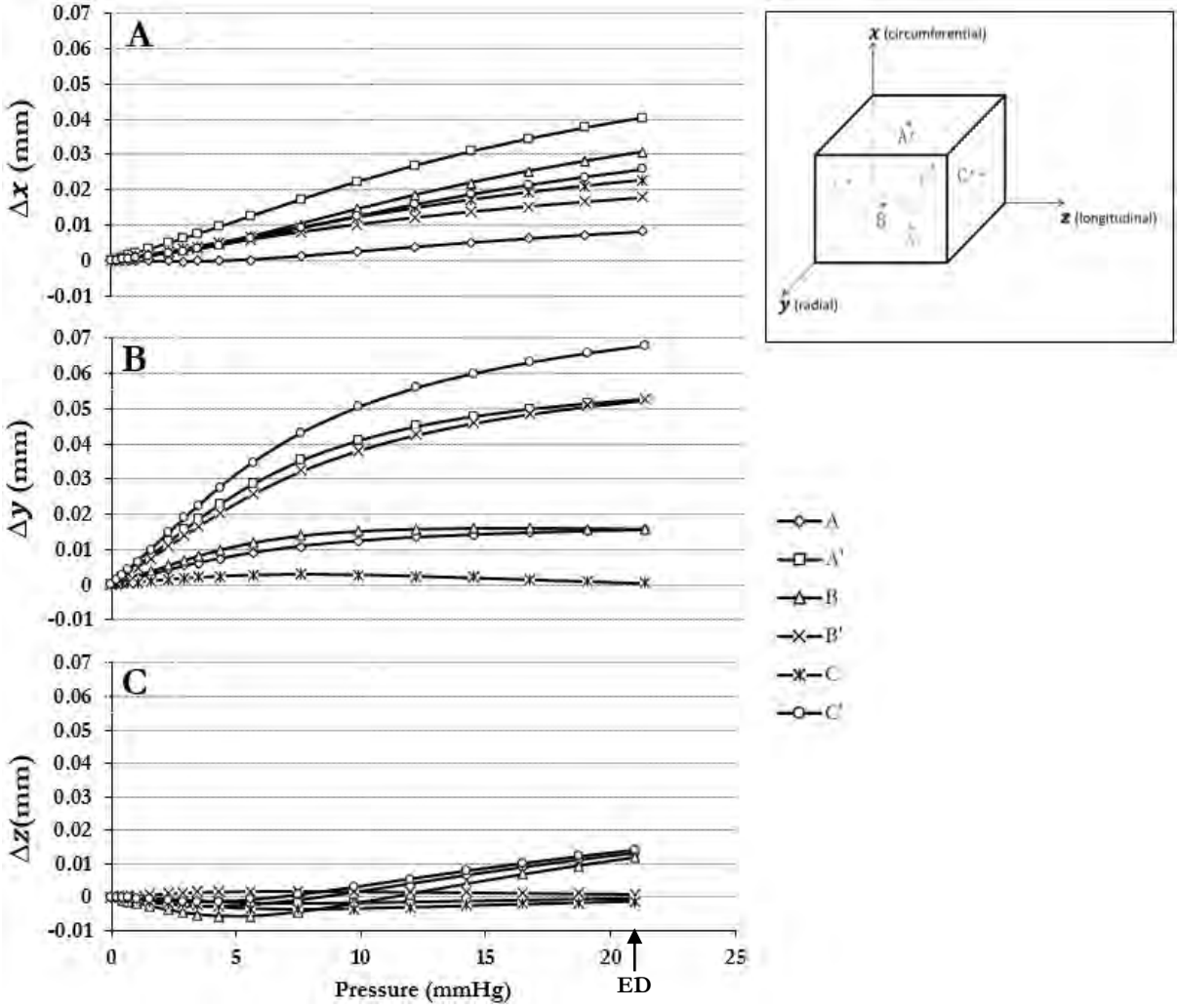

Figure 6.6: Displacement of surfaces of the block model during LV diastolic filling in x (a) y (b) and z (c) directions. The panel in the corner was readopted from Figure 6.3 for illustration. The arrow denotes the end-diastolic pressure.

6.3.2 End-diastolic strain and stress

In Figure 6.7, the mean ED strain and stress predicted in tissue sections are shown for the different models described in Table 6.3. The average strain in fibre direction, Figure 6.7 (a), was 0.009 for 7d and 28d untreated infarcts and decreased to 0.006 and 0.007 in the G03-treated infarcts, respectively. Increasing the gel stiffness in composites resulted in an increase in the infarct strain at both infarct stages. A similar trend was observed in the cross-fibre direction strain, Figure 6.7 (b), with the exception that different tissue sections exhibited negative strains.

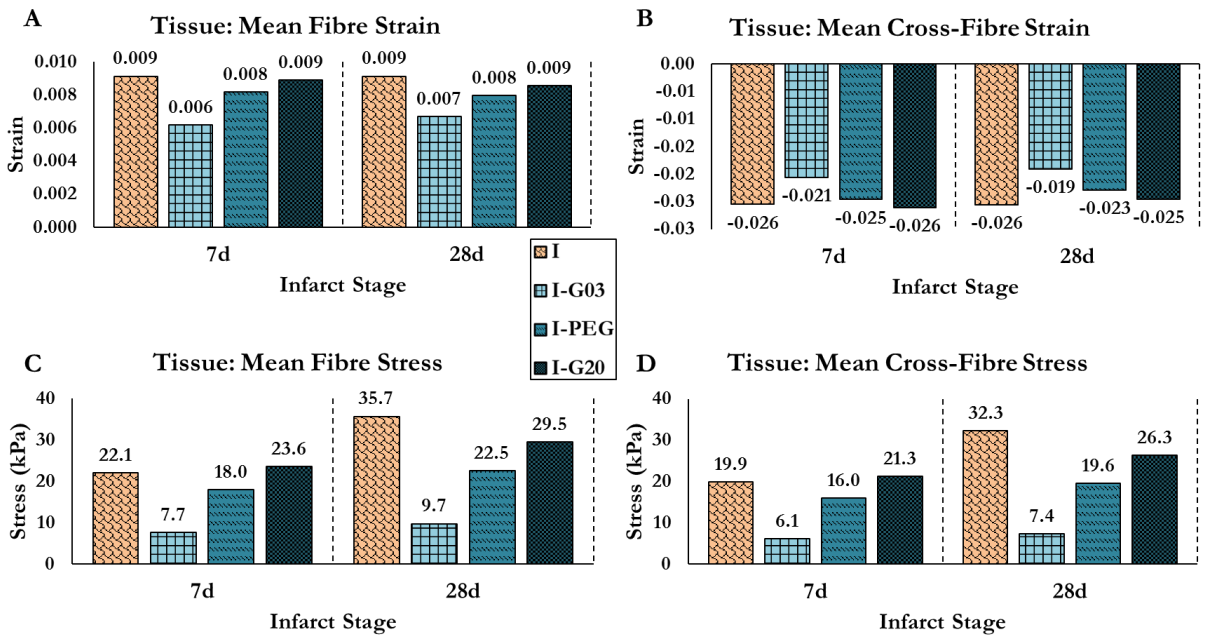

Figure 6.7: Mean end-diastolic fibre and cross-fibre strain and stress predicted in tissue sections of different blocks. (a) Fibre strain. (b) Cross-fibre strain. (c) Fibre stress. (d) Cross-fibre stress.

The stress in the fibre direction, Figure 6.7 (c), was decreased in 7d and 28d infarcts by 65 % and 73 %, respectively, as a result of the soft injectate; G03. An increase in fibre stress was observed in both infarct stages with the increase in gel stiffness. The 7d infarct treated with the stiff injectate, G20, exhibited a fibre stress of 23.6 kPa exceeding the stress exhibited by the untreated infarct (22.1 kPa). As shown in Figure 6.7 (d), the cross-fibre stresses were slightly lower than the fibre stresses with a very comparable trend.

Figure 6.8 illustrates the maximum ED strain and stress in tissue sections of the different models. The maximum fibre strain, Figure 6.8 (a), was equal for all untreated and treated infarcts. Unlike the average data, the maximum cross-fibre strain, Figure 6.8 (b), showed positive values. The treated infarcts exhibited larger cross-fibre strains than the untreated infarcts and the strain level decreased as the injectate stiffness increased. The maximum fibre stress, Figure 6.8 (c), and cross-fibre stress, Figure 6.8 (d), showed a trend similar to the one observed for the average data.

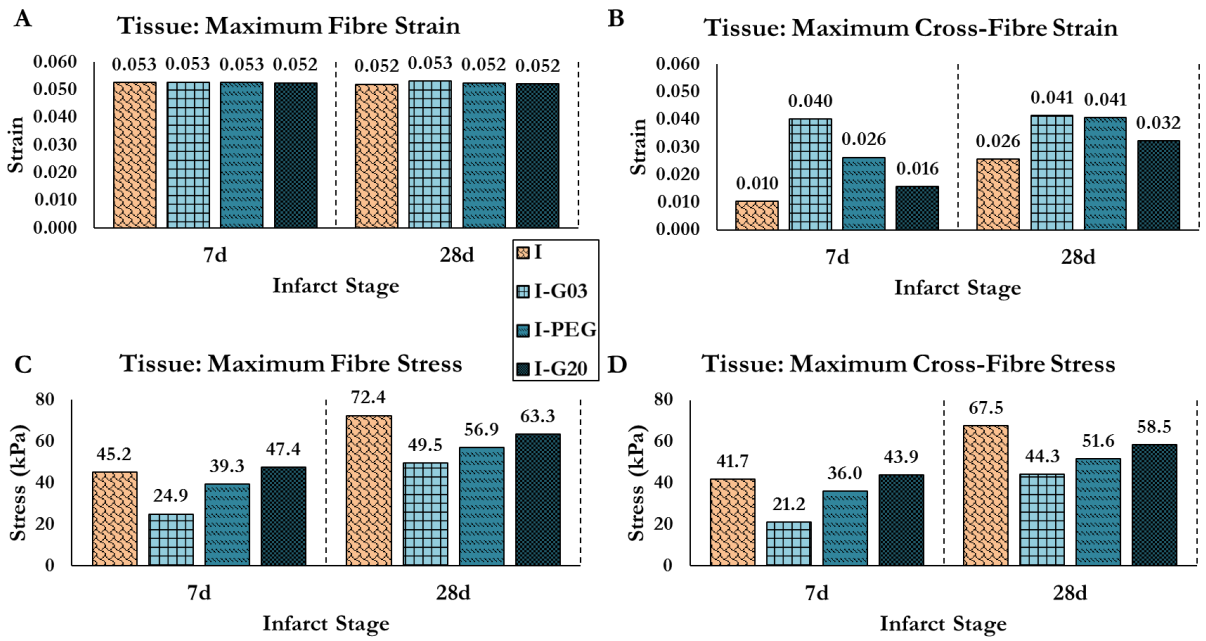

Figure 6.8: Maximum end-diastolic fibre and cross-fibre strain and stress predicted in tissue sections of different block models. (a) Fibre strain. (b) Cross-fibre strain. (c) Fibre stress. (d) Cross-fibre stress.

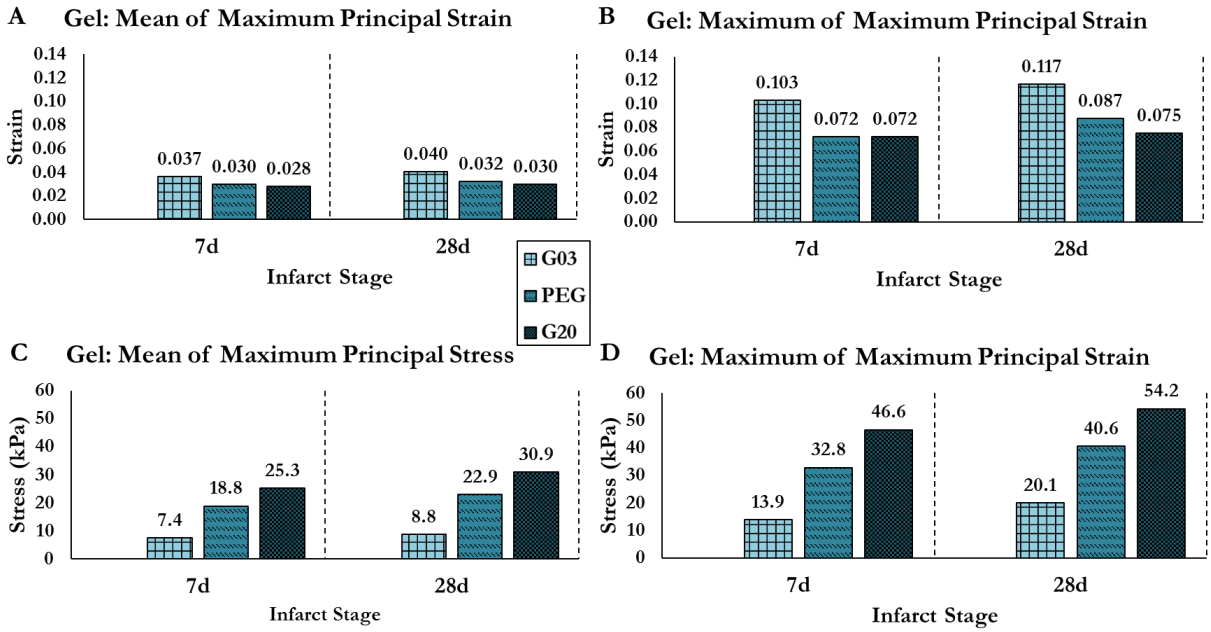

Figure 6.9: Mean and maximum end-diastolic maximum principal strain and stress predicted in gel sections of different composite blocks. (a) Mean strain. (b) Maximum strain. (c) Mean stress. (d) Maximum stress.

Figure 6.9 shows the average and maximum ED maximum principal strain and stress predicted in the gel section of the different infarct-gel composites. As the gel stiffness increased, strain levels

decreased, Figure 6.9 (a, b), and stress levels increased, Figure 6.9 (c, d), irrespective of the infarct stage. With the increase in infarct stiffness from 7d to 28d, the injectate average strain, Figure 6.9 (a), increased by 8 % (G03), 6 % (PEG) and 7% (G20). Similarly, G03, PEG and G20 injectates experienced respectively a 16 %, 18 % and 18 % increase in gel average stress, Figure 6.9 (c), at 28d compared to 7d infarct stage. The largest maximum principal strain and stress, Figure 6.9 (b, d), exhibited similar trends to the average data.

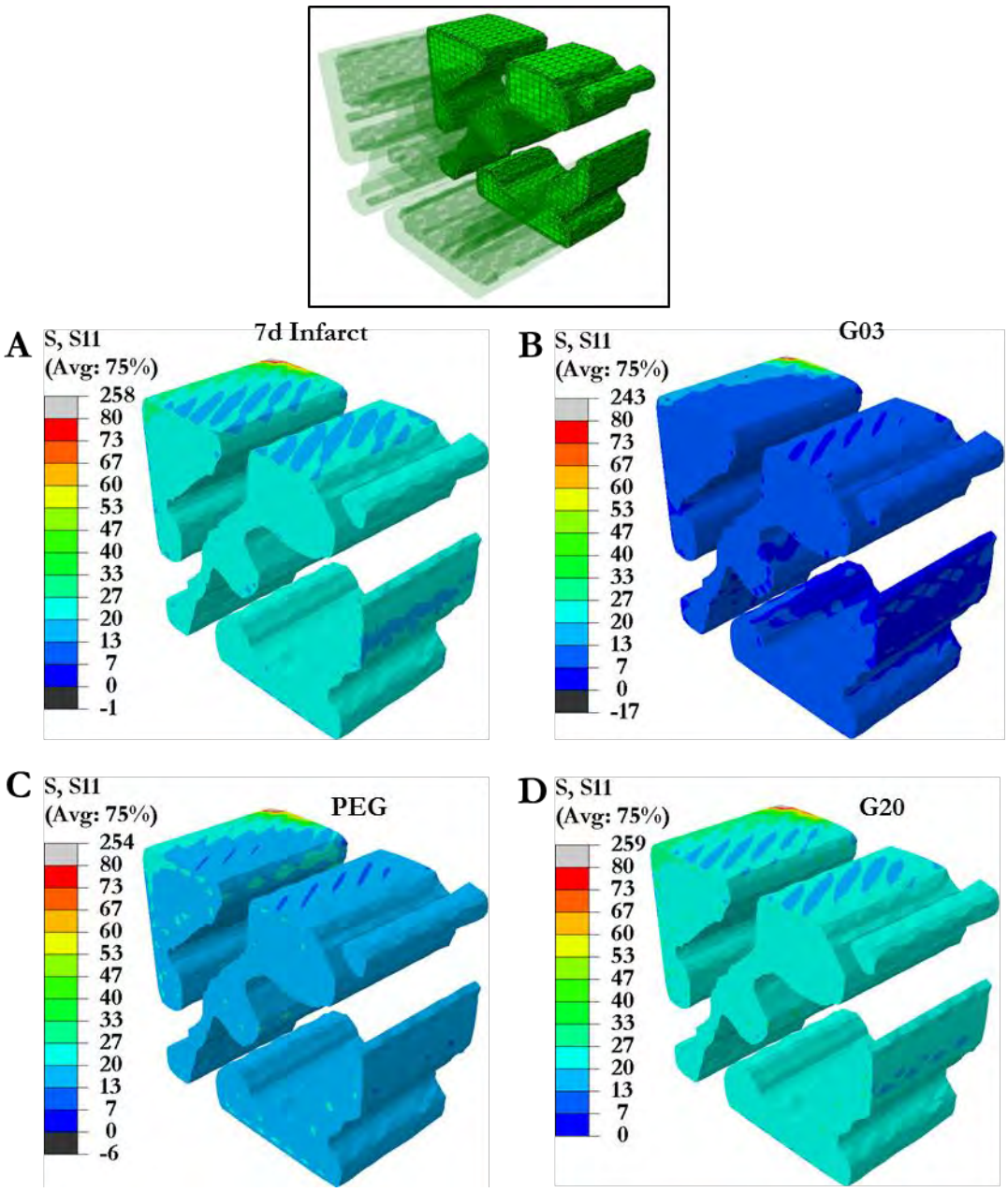

Figure 6.10: Distribution of fibre stress (kPa) in 7d infarct sections from different block models. Sections are shown partially for illustration purposes as indicated in the upper inset. (a) Untreated infarct. (b) G03-treated infarct. (c) PEG-treated infarct. (d) G20-treated infarct. Excluding stress concentrations from boundary conditions, the same stress scale is used for all plots.

Contour plots of fibre stress in the 7d and 28d infarct sections are shown in Figure 6.10 and Figure 6.11, respectively. Contour plots of the maximum principal stress in the gel sections are shown in Figure 6.12. The stress distribution was not uniform in all of the tissue and gel sections wherein spots of stress concentrations were observed.

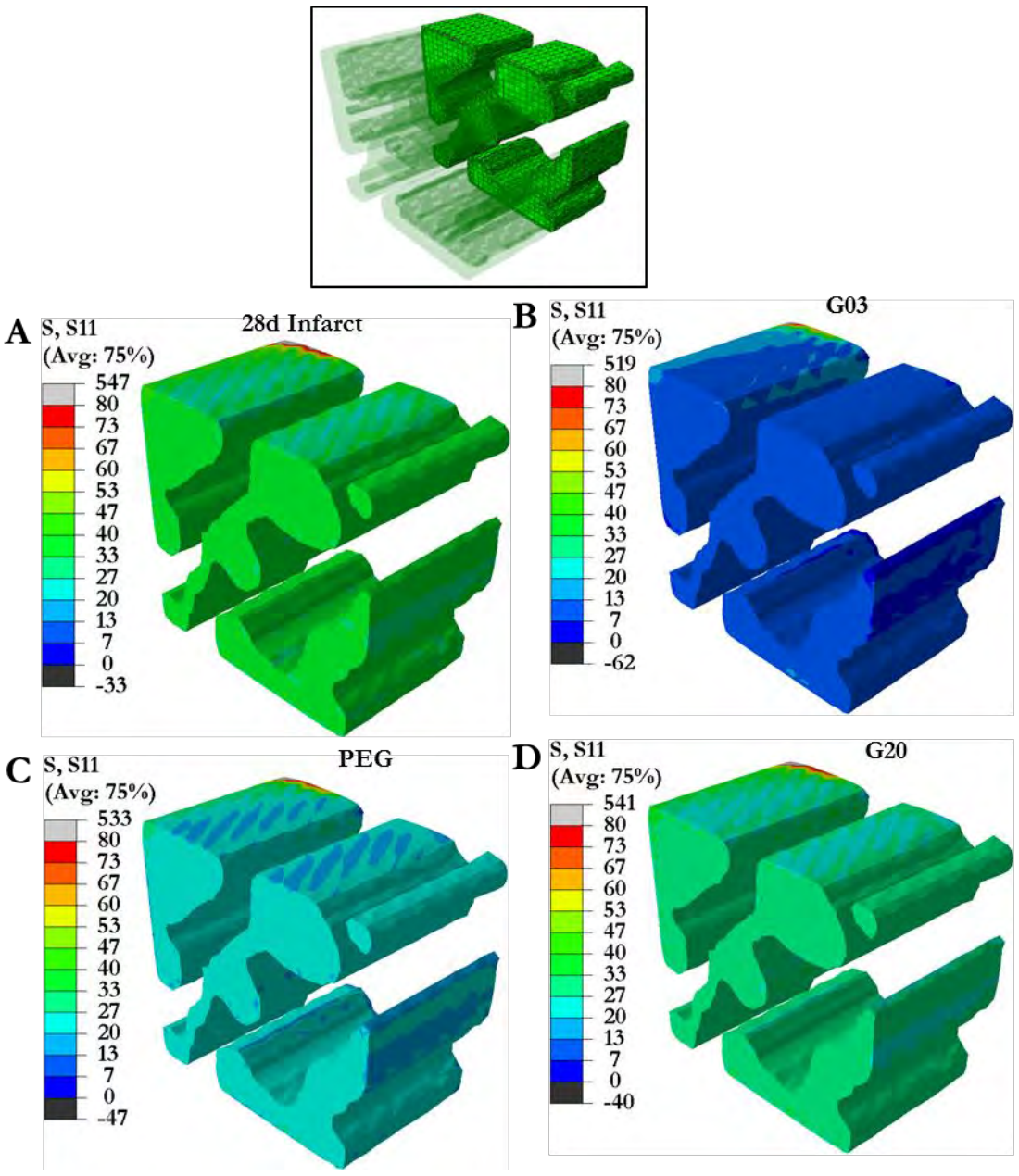

Figure 6.11: Distribution of fibre stress (kPa) in 28d infarct sections from different block models. Sections are shown partially for illustration purposes as indicated in the upper inset. (a) Untreated infarct. (b) G03-treated infarct. (c) PEG-treated infarct. (d) G20-treated infarct. Excluding stress concentrations from boundary conditions, the same stress scale is used for all plots.

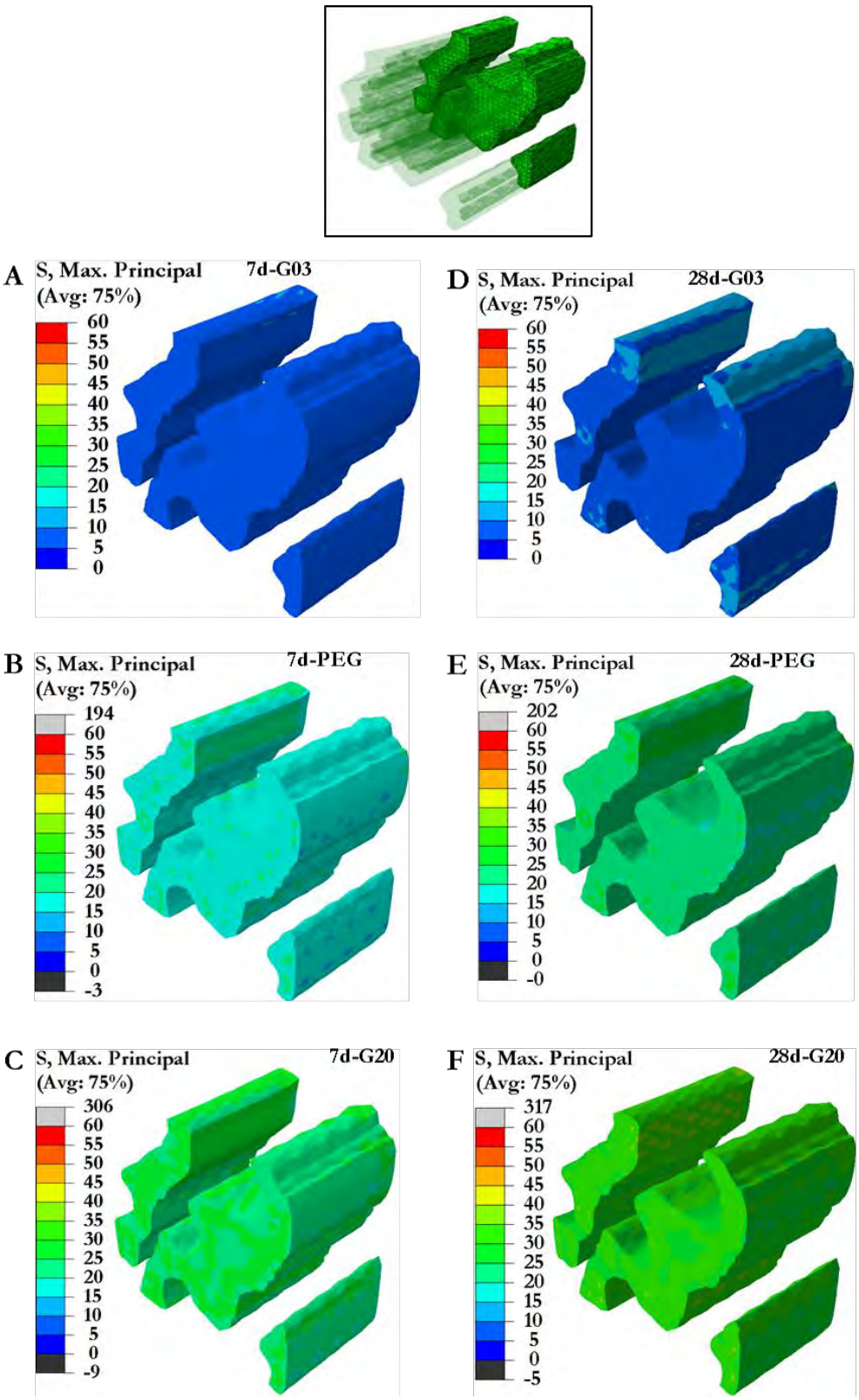

Figure 6.12: Distribution of maximum principal stress (kPa) in gel sections from different composite block models. Sections are shown partially for illustration purposes as indicated in the upper inset. (a) Gel section of 7d-G03 composite. (b) Gel section of 7d-PEG composite. (c) Gel section of 7d-G20 composite. (d) Gel section of 28d-G03 composite. (e) Gel section of 28d-PEG composite. (f) Gel section of 28d-G20 composite. Excluding stress concentrations from boundary conditions, the same stress scale is used for all plots.

6.4 Discussion

The FE studies which previously investigated the mechanics of biomaterial injectates used either of two modelling approaches: 1) homogenised infarct-injectate region (Wall et al. 2006; Wenk et al. 2011b; Wise 2013) or 2) discrete representation of infarct and injectate with approximated geometries for the injectate (Wenk et al. 2009; Kortsmit et al. 2013; Miller et al. 2013; Kortsmit et al. 2013b; Kichula et al. 2014). In this study, a microstructural model of myocardium-injectate composite was utilized to computationally investigate the micromechanics of biomaterial injectates and surrounding infarcted myocardium during the diastolic phase of the cardiac cycle. The developed model realistically represented the microstructural distribution of the injectate observed in situ when delivering PEG hydrogels shown in Figure 3.1 (a) and Figure 3.2 (c).

With this approach, a decrease in the fibre and cross-fibre stresses in the infarct section as a result of the injected biomaterial was demonstrated. This beneficial effect decreased as the stiffness of the biomaterial increased. On the other hand, the micromechanics of the injectate was influenced by the change in infarct stage.

The effect of the injectate on reducing the infarct stress was demonstrated in previous studies (Wenk et al. 2009; Kortsmit et al. 2013; Miller et al. 2013; Kortsmit et al. 2013b; Kichula et al. 2014). In this study, however, a micromechanical mechanism is proposed by which the injectate induces such reduction in the infarct stress during diastolic filling. It is suggested that the gel works as a force attenuating system reducing the force acting on tissue layers during the passive diastolic dilation of the LV and thus reducing the stress induced in these tissue layers.

6.4.1 Microscopic deformation in the anterior wall

The analysis of the surface displacements for the anterior midwall block during diastolic loading (Figure 6.6) revealed a complex deformation. The deformation involved normal and shear strains in the different orthogonal directions (Table 6.4).

The approach of using a block geometry to analyse the local deformation in the ventricle wall has been employed in a study by Bogaert et al. (2000). They utilized cuboids to analyse the normal and shear strains LV deformation through CMR myocardial tagging of human hearts. However, the strains were calculated from the displacement of cuboid corners whereas in the current study the predicted strains were calculated from block surfaces. Bogaert et al. (2000) also reported the complex deformation and quantified such deformation using normal and shear strains. Another study that measured the in vivo strain on rat hearts was conducted by Fomovsky and Holmes

(2010) who measured strains through epicardial sonomicrometer crystals. Table 6.5 compares the predicted normal strains to the in vivo experimental strain measurements from Fomovsky and Holmes (2010) and Bogaert et al. (2000). The in vivo strains adopted from these two studies were measured from ED to ES time points whereas the strains in our study were measured from ES to ED. To account for this difference, the model strains shown in Table 6.5 were recalculated from ED to ES and thus differ from the values previously shown in Table 6.4.

Table 6.5: Comparison between FE predicted strains and in vivo strain measurements reported in other studies.

Strain	Description	Model Prediction* (%)	In vivo Measurements (%)	
			Rat [1]	*Human* [2]
E_{xx}	Circumferential	-7.86	-7±4	-12.8±6.9
E_{yy}	Radial	12.28	—	37.9±20.6
E_{zz}	Longitudinal	-4.41	-5±3	-13.3±7.9

* Calculated from end-diastolic to end-systolic, [1] Fomovsky and Holmes (2010), [2] Bogaert et al. (2000)

The predicted circumferential and longitudinal strain values; -7.86 % and -4.61 %, correlate with the rat in vivo strain; -7±4 % and -5±3 % respectively. However, there is a quantitative difference between model predications and human in vivo strains. This is expected since heart size and loading conditions are different. However, there are qualitative similarities. For example, both the model and the human strain values indicate that the maximum normal strain is in the radial direction and that there is mechanical coupling between the radial and other cardiac directions (i.e. circumferential and longitudinal). Despite these differences, the quantitative and qualitative similarities between the computational and experimental strains validated the LV model and showed that the micromechanical investigations were established using realistic loading conditions.

6.4.2 Micromechanics of biomaterial injectate

The investigation in the current study was based on two extreme infarct healing phases; the 7 and 28 day infarcts. The infarct stiffness considerably increases between these two healing phases as previously discussed in Chapter 4. Therefore, these phases allowed us to evaluate the micromechanical impact of the gel on two distinct infarcts, and vice versa. Introducing three gels with different stiffness in the study was driven by the variety of injectate stiffness (Wall et al. 2006). Another motivation was the findings of a previous study (Ifkovits et al. 2010) which demonstrated

that injecting a hyaluronic acid hydrogel with higher compressive modulus resulted in a reduced infarct expansion and LV dilation and improved function compared to lower modulus hydrogel.

The tissue-gel composite model (Figure 6.4) was developed by extrusion of a 2D masks of tissue and gel from a single histology section. This resulted in 3D model of a uniform longitudinal shape. Since the slice-to-slice distance between histology sections were ~300 μm, there was no information on the change of tissue and/or gel structure between two subsequent sections. Therefore, it was assumed that within such small longitudinal distance the structure of tissue and gel was uniform. The segmented field in the histology image, Figure 6.4 (a), was specified so that the volume ratio between tissue and gel in the composite model was ~1:1. The reason was to reduce possible mechanical effects from predominance of specific material volume (Wise 2013). The composite model was developed as a single continuum structure where tissue and gel sections were identified through different sets of elements. Ideally, one would develop tissue and gel as separate structures and define contact between them. However, this was not feasible since information on the contact between tissue and injectate; such as friction coefficients, was not available. As such, assigning tissue and gel materials to different element sets was the only efficient way. This technique has been used in FE analysis of injectate-based MI therapy (Miller 2012; Kortsmit et al. 2013; Kortsmit et al. 2013b).

The negative mean cross-fibre strains, Figure 6.7 (b), and positive mean cross-fibre stresses, Figure 6.7 (d), exhibited by different tissue sections can be attributed to the mechanical coupling between the tissue fibre and cross-fibre directions. Mechanical coupling between fibre and cross-fibre directions has been reported for healthy myocardium (Ghaemi et al. 2009). In our study (Chapter 4), the mechanical coupling between circumferential and longitudinal directions of infarcted myocardium was observed and discussed.

The deformation of all untreated and treated infarct block models was induced by the displacement of the boundary nodes (Figure 6.5). Although these nodes were displaced equally for all block models, the models exhibited different mean strains in both sections; i.e. the infarct, Figure 6.7 (a), and the gel, Figure 6.9 (a). This is attributed to the difference in the "internal" deformation of infarct and gel sections between the different models. Such internal deformation is illustrated by the distribution of the displacement field in the internal elements of the block sections as shown in Figure 6.13. Although the displacement distribution on the boundary elements was similar for the different models, the internal elements exhibited distinct distribution indicating differences in internal deformation.

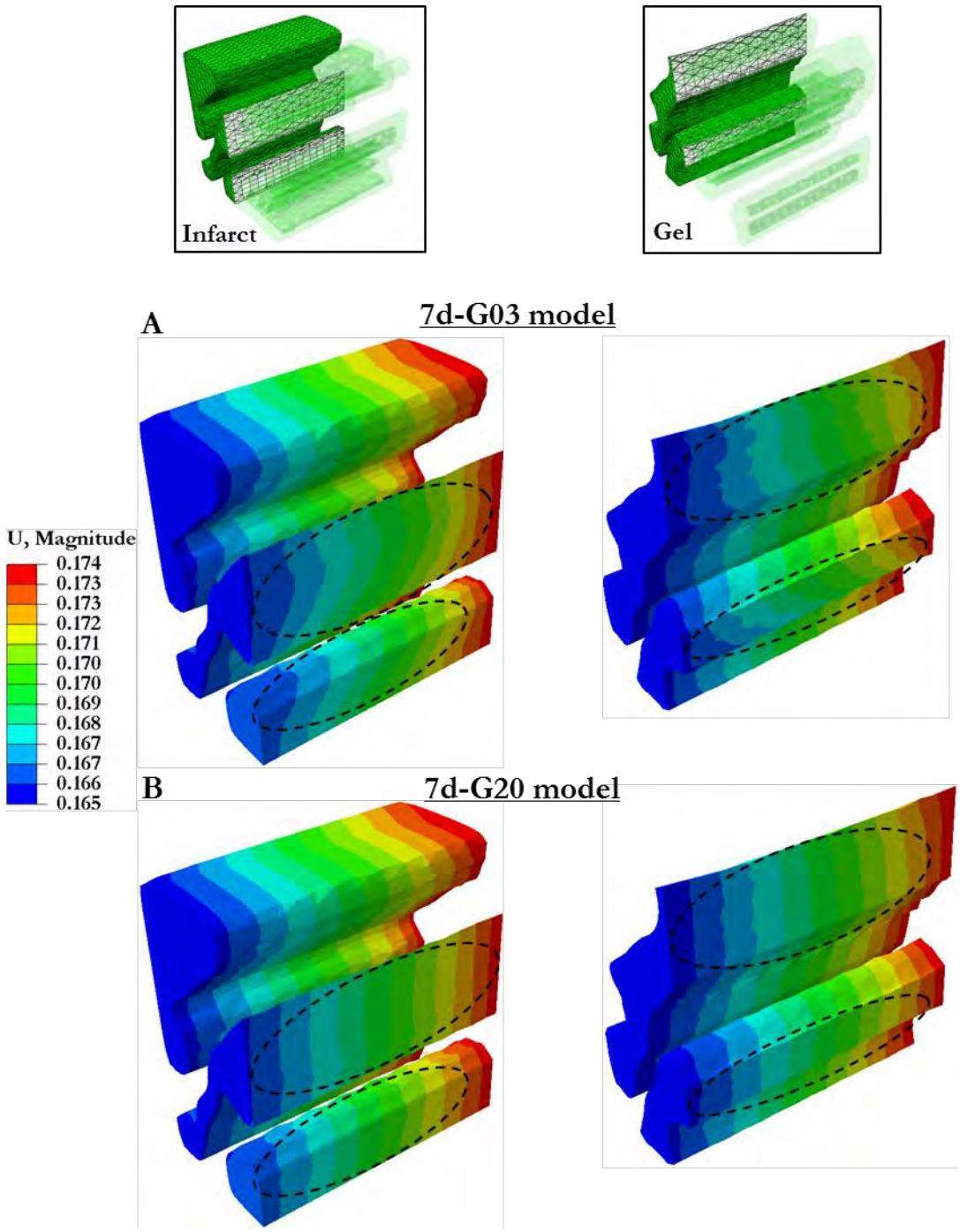

Figure 6.13: Distribution of resultant displacement (mm) in the infarct and gel sections of two block models; 7d infarct treated with G03 and 7d gel infarct treated with G20 gel. Sections are showing partially as illustrated in the panels. Internal elements exhibits different displacements in the same section of two different models (dotted circles). (a) 7d infarct section treated with G03. (b) 7d infarct section treated with G20.

The G03-treated infarcts showed a decrease in mean fibre strain compared to the untreated infarcts, Figure 6.7 (a). The increase in the fibre strains of the treated infarcts was then associated with the increase in the gel stiffness. On the other hand, the mean gel strain decreased with increasing gel stiffness, Figure 6.9 (a). The infarct and gel are organized in layers. Considering that

the deformation in the radial direction E_{yy} is the predominant normal deformation (Table 6.4), such layers can be represented by a system of transmural springs connected in series. These springs have separate stiffness factors; infarct stiffness (k_I) and gel stiffness (k_G). When $k_I = k_G$, extending or compressing this system will result in an equal deformation (strain) in both sections. However, when $k_G < k_I$, applying the same extension/compression will result in an increased deformation in the gel and decreased deformation in the infarct. As k_G increases, the gel strain will decrease and the infarct strain will increase until reaching the state of $k_I \approx k_G$ at which the gel strain will be minimum and infarct strain will be maximum. Hence, it can be argued that stiffness of the G20 gel and the 7d infarct is comparable.

The results illustrated a beneficial reduction of stress levels in infarcts in the presence of gel, Figure 6.7 (c, d) and Figure 6.8 (c, d). Such beneficial impact has been observed in previous studies (Kortsmit et al. 2013; Miller et al. 2013; Kortsmit et al. 2013b; Kichula et al. 2014). However, the variation in gel stiffness induced distinct reactions. For the 7d infarct, only G03 and PEG gels showed beneficial effects. G20 gel slightly increased the fibre and cross-fibre stress in the tissue. For the 28d infarct, stress reduction was observed for all gel types. As discussed earlier, the predominant normal deformation during diastolic filling is in the radial direction and with a compressive nature. As such, a coupling tensile force is induced in the transverse direction which is proportionally related to the radial deformation. Assuming that the fibre stresses are associated with this induced tensile force, the less the radial deformation is (in the presence of gel) the less stress is induced in the fibres. In previous studies, the reduction in stresses after gel injection was attributed to the LV wall thickening (Wall et al. 2006) and/or the increased stiffness of the gel/infarct composite (Kichula et al. 2014). The current results suggest an additional mechanism by which the gel reduces the stress level. It is proposed that the gel attenuates the forces acting on the tissue by limiting the tissue deformation in the transverse direction during the passive diastolic dilation of the LV. For the gel to reduce the force, however, the stiffness of the gel should be less than the infarct. This condition is implied by the elevated stress levels in the 7d infarct when treated with G20. Ifkovits et al. (2010) showed that the high stiffness gels were superior to the low stiffness gels in terms of the long-term infarct expansion and LV function in a sheep infarct model. If we assume that this beneficial effect was associated with the attenuation in wall stresses (Wall et al. 2006), then it is likely that increasing the gel stiffness is beneficial during systole. However, the current study showed that softer gels are superior during diastole.

The stiffness of the gels increase by 4-fold from G03 (c_{10}= 3 kPa) to PEG gel (c_{10}= 12.3 kPa) and by 1.6-fold from PEG to G20 gel (c_{10}= 20 kPa). These ratios were reflected in the predicted

stresses. For example, mean fibre stress, Figure 6.7 (c), in 7d infarct increases by 2.3-fold from G03 to PEG and 1.3-fold from PEG to G20. Similarly for 28d infarct, stress increase by 2.3-fold (G03 to PEG) and 1.3-fold (PEG to G20). As the infarct heals, a particular gel experiences an increase in strain and stress, Figure 6.9 (a, c). These findings may be of interest in specific context. For example, the change in shear stress of the gel may indicate a change in the gel flow. Considering that gels may be utilized as cell carriers or scaffolds for tissue repair, the increase in gel strains alter the mechanical boundary condition which in turn may affect the growth of these cells (Billiar 2011).

6.4.3 Limitation

A major limitation in this study is controlling the deformation of the untreated and treated infarct block models using the deformation of a healthy LV. Attempts were made to correct this conflict by reducing deformation in the composite blocks. A more accurate approach, however, might be necessary through modelling a treated infarct region (homogenised) in the LV for the different gel/tissue combinations and then utilizing this region to drive the deformation of the relative block.

7 Conclusions and recommendations

The aim of this research was the contribution to the understanding and advancement of the emerging therapies for acute myocardial infarction (MI) based on the injection of biomaterials into the ischemic myocardium, by way of studying the biomechanical mechanisms associated with this treatment. The objectives of the research included the following:

1) To establish adequate computational models to simulate myocardial and ventricular mechanics.
2) To investigate the in vivo intramyocardial three-dimensional (3D) microstructural spatial distribution of polymeric biomaterial injectate and utilize this geometric information in computational models.
3) To establish constitutive models for infarcted myocardial tissue through biaxial mechanical testing.
4) To computationally simulate the regional micromechanics of myocardium with interlaced polymeric biomaterial with particular reference to the infarct zone.
5) To computationally investigate novel concepts for material-injection based MI therapy and preventive interventions for heart failure with regard to the biomechanical effects of biomaterial injection, and predict their influence on treatment outcomes.

These objectives were met through a number of studies presented in this thesis. The following sections describe the main conclusions from the work presented in the previous chapters. Recommendations of possible extensions of the current research are proposed at the end.

7.1 Conclusions

7.1.1 Geometrical model of heart and gel injectate

Aiming at establishing computational models based on realistic geometry of gel injectate, we developed a biventricular cardiac rat model in combination with micro-detailed intramyocardial hydrogel injectate. The developed model provides realistic geometries for advanced computational investigations of biomaterial-injectate based MI therapies.

While the reconstructed injectate geometry stemmed from acellular injections in the rat, the high level of geometrical detail not only allows studying of the injectate-myocardium micromechanics. It can also render the geometry suitable for the representation of the physical environment for cells in the cellular biomaterial injectate. Therefore, the developed model also promotes computational studies of cell mechanics and mechanobiology in MI therapies.

7.1.2 Mechanical characterization of infarcted rat myocardium

We comprehensively characterized the mechanical properties of healing infarcts in a rat model. This study revealed that healing infarcts in rat hearts are mechanically anisotropic with the circumferential direction being stiffer than the longitudinal direction. The degree of anisotropy may vary between healing stages according to the amount of directional load and the orientation of the deposited collagen. The latter plays a major role in inducing the in-plane mechanical coupling between the two major axes.

As the infarct healing progresses, the circumferential and compressive stiffness increases more pronouncedly compared to the longitudinal stiffness. The presented data are essential for developing material models for healing infarcts and for setting a baseline for future mechanical assessment of biomaterial injectate impact on infarcted myocardium in rat models.

7.1.3 Identification of material constants for healing infarcts

The biaxial mechanical data were employed to establish constitutive models of healing infarcts in the rat model. Finite element (FE) model and genetic algorithm (GA) were employed to identify the parameters of Fung orthotropic hyperelastic strain energy function for the healing infarcts. GA is a powerful tool for global optimization of complex problems and, when combined with FE modelling, provides an effective approach for solving inverse problems.

Within the physiological range of biaxial strains and when Fung orthotropic model is utilized, FE models of myocardial tissue are insensitive to the density of transmural fibre layers or the element type. The identified material constants provide new platform for FE investigations of mechanical aspects of MI and therapies in particular when using rat models.

7.1.4 Micromechanics of injectate during diastole

A realistic micro-structurally detailed model of tissue and hydrogel developed from histology images was utilized in FE analysis of biomaterial injectate. We demonstrated that the micromechanics of biomaterial injectate can provide important information and help understand the mutual mechanical effect between the infarct tissue and the injected material.

Good correlation was found between the predicted mechanics at such microscopic level with macroscopic finding from other studies. Focusing on the diastolic phase of the cardiac cycle, we found that increasing the stiffness of the injectate had an undesirable effect. We suggest a micromechanical mechanism by which the injectate reduces the infarct stress during the passive diastolic filling; the gel acts as attenuating system reducing the forces exerted on the fibres of the infarcted tissue. The predicted mechanics of gels revealed a sensitivity to change in the infarct properties during healing.

7.2 Recommendations

The work presented in this thesis can possibly be extended in several ways.

7.2.1 Injectate 3D model

Incorporating realistic 3D geometry of biomaterial injectate in FE models is feasible from histology micrographs. Yet, this approach has two limitations: 1) the subjectivity in the alignment of histology images prior to 3D reconstruction, and 2) the relatively low longitudinal (slice-to-slice) resolution. Although obtaining higher longitudinal resolution from histology micrographs may be possible, it is challenging both in the histological workup and in the image reconstruction (in particular image alignment). Therefore, examining other techniques to obtain images of sections from the intact (i.e. non-sectioned) hearts is highly recommended.

The in vivo imaging methods can provide essential data to assess the change in the injectate geometry during cardiac cycle. Ex vivo imaging of the explanted heart is also a possible alternative. Reconstructing the injectate geometry from an explanted heart using micro computed tomography (micro-CT), for example, is a suggested approach although gel visibility in x-rays might be

challenging. Arresting the heart at end-diastole and end-systole and utilizing micro-CT for obtain image data can also allow the assessment of the change in injectate geometry during cardiac cycle.

Kadner et al. (2012) showed that the in situ injectate geometry can vary substantially when delivered at different time points after the infarct induction. The current study focused at the immediate injection whereas injectate geometries for delayed injections can be subject of future research.

7.2.2 Mechanical testing and constitutive modelling

In terms of mechanical testing, examining the infarct mechanical behaviour under shear loading can provide important data. Such data can be incorporated in constitutive modelling of the infarct. It will also help assessing the impact of the gel injectate on shear stress.

Additionally, testing infarct samples using a triaxial (3-axis) testing system is suggested, despite the difficulties related to sample size, such as the one recently proposed by Hill et al. (2014). Triaxial testing of rat infarcts, if feasible, will allow for adequate 3D constitutive modelling for the orthotropic myocardial infarct.

Another interesting extension of the current work includes the quantification of the orientation of collagen fibres in individual samples and the overall orientation for the different infarct groups. Such data may help in understanding the underlying mechanisms leading to the mechanical behaviour observed in the various phases of infarct healing. Also such information can be incorporated in the inverse model which will improve the accuracy of the identified parameters.

7.2.3 Micromechanics of biomaterial injectate in systole

We investigated the micromechanics of biomaterial injectate during the diastolic phase of the cardiac cycle. Implementation of active contraction in the constitutive model and investigation of the infarct-gel composites during systole is a potential extension of the current work. Also instead of modelling the gel and infarct as separate elements set in one model, contact can be applied through finding the friction coefficient of hydrogel on myocardial tissue. Additionally, utilization of LV models with homogenised gel-infarct region to drive the deformation of the block models is suggested.

References

Abaqus (2012). Abaqus 6.12 Documentation. Providence, RI, USA, Dassault Systèmes.

Abarbanell AM, Herrmann JL, Weil BR, Wang Y, Tan J, Moberly SP, Fiege JW, Meldrum DR (2010). Animal models of myocardial and vascular injury. J Surg Res **162**(2): 239-49.

AHA (2005). Part 8: Stabilization of the patient with acute coronary syndromes. Circulation. **112:** IV-89-IV-110.

AHA (2008). Heart disease and stroke statistics: Our guide to current statistics and the supplement to our heart and stroke facts. Dallas, American Heart Association.

Aikawa Y, Rohde L, Plehn J, Greaves SC, Menapace F, Arnold JMO, Rouleau J-L, Pfeffer MA, Lee RT, Solomon SD (2001). Regional wall stress predicts ventricular remodeling after anteroseptal myocardial infarction in the healing and early afterload reducing trial (heart): An echocardiography-based structural analysis. Am Heart J **141**(2): 234-42.

Alonso DR, Scheidt S, Post M, Killip T (1973). Pathophysiology of cardiogenic shock. Quantification of myocardial necrosis, clinical, pathologic and electrocardiographic correlations. Circulation **48**(3): 588-96.

Antman E, Bassand J-P, Klein W, Ohman M, Lopez Sendon JL, Rydén L, Simoons M, Tendera M (2000). Myocardial infarction redefined—a consensus document of the joint european society of cardiology/american college of cardiology committee for the redefinition of myocardial infarction: The joint european society of cardiology/ american college of cardiology committee. J Am Coll Cardiol **36**(3): 959-69.

Arts T, Reneman RS, Veenstra PC (1979). A model of the mechanics of the left ventricle. Ann Biomed Eng **7**(3-4): 299-318.

Arts T, Veenstra PC, Reneman RS (1982). Epicardial deformation and left ventricular wall mechanisms during ejection in the dog. Am J Physiol **243**(3): H379-90.

Atkins BZ, Hueman MT, Meuchel J, Hutcheson KA, Glower DD, Taylor DA (1999). Cellular cardiomyoplasty improves diastolic properties of injured heart. J Surg Res **85**(2): 234-42.

Bates ER (2007). Role of intravenous β-blockers in the treatment of st-elevation myocardial infarction: Of mice (dogs, pigs) and men. Circulation **115**(23): 2904-6.

Bates ER, Menees DS (2012). Acute st-elevation myocardial infarction. Current Opinion in Critical Care **18**(5): 417-23.

Belik ME, Usyk TP, McCulloch AD (2004). Computational methods for cardiac electrophysiology, in: Ayache N, Ed. Computational models for the human body, Elsevier B.V. 129-88.

Bettendorff-Bakman DE, Schmid P, Lunkenheimer PP, Niederer P (2006). A finite element study relating to the rapid filling phase of the human ventricles. J Theor Biol **238**(2): 303-16.

Billiar KL (2011). The mechanical environment of cells in collagen gel models, in: Gefen A, Ed. Cellular and biomolecular mechanics and mechanobiology. Berlin Heidelberg, Springer. 201-45.

Billiar KL, Sacks MS (2000). Biaxial mechanical properties of the natural and glutaraldehyde treated aortic valve cusp--part i: Experimental results. J Biomech Eng **122**(1): 23-30.

Birnbaum Y, Chamoun AJ, Anzuini A, Lick SD, Ahmad M, Uretsky BF (2003). Ventricular free wall rupture following acute myocardial infarction. Coron Artery Dis **14**(6): 463-70.

Boersma E, Maas ACP, Deckers JW, Simoons ML (1996). Early thrombolytic treatment in acute myocardial infarction: Reappraisal of the golden hour. The Lancet **348**(9030): 771-5.

Bogaert J, Bosmans H, Maes A, Suetens P, Marchal G, Rademakers FE (2000). Remote myocardial dysfunction after acute anterior myocardial infarction: Impact of left ventricular shape on regional function: A magnetic resonance myocardial tagging study. J Am Coll Cardiol **35**(6): 1525-34.

Bogen DK, Rabinowitz SA, Needleman A, McMahon TA, Abelmann WH (1980). An analysis of the mechanical disadvantage of myocardial infarction in the canine left ventricle. Circ Res **47**(5): 728-41.

Borade G. (2013). "Blocked arteries: Symptoms and treatment." from buzzle.com.

Bovendeerd PHM, Arts T, Huyghe JM, van Campen DH, Reneman RS (1992). Dependence of local left ventricular wall mechanics on myocardial fiber orientation: A model study. J Biomech **25**(10): 1129-40.

Broemser P, Ranke OF (1930). Uber die messung des schlagvolumens des herzens auf unblutigem weg. Z Biol **90**: 467.

Burkhoff D, Mirsky I, Suga H (2005). Assessment of systolic and diastolic ventricular properties via pressure- volume analysis: A guide for clinical, translational, and basic researchers. American Journal of Physiology: Heart & Circulatory Physiology **58**(2): H501-H12.

Chadwick RS (1982). Mechanics of the left ventricle. Biophys J **39**(3): 279-88.

Chen J, Song S-K, Liu W, McLean M, Allen JS, Tan J, Wickline SA, Yu X (2003). Remodeling of cardiac fiber structure after infarction in rats quantified with diffusion tensor mri. Am J Physiol Heart Circ Physiol **285**(3): H946-H54.

Chew PH, Yin FCP, Zeger SL (1986). Biaxial stress-strain properties of canine pericardium. J Mol Cell Cardiol **18**(6): 567-78.

Christman KL, Lee RJ (2006). Biomaterials for the treatment of myocardial infarction. J Am Coll Cardiol **48**(5): 907-13.

Christman KL, Vardanian AJ, Fang Q, Sievers RE, Fok HH, Lee RJ (2004). Injectable fibrin scaffold improves cell transplant survival, reduces infarct expansion, and induces neovasculature formation in ischemic myocardium. J Am Coll Cardiol **44**(3): 654-60.

Clarke S, Ghanta R, Ailawadi G, Holmes J (2014). Cardiac restraint and support following myocardial infarction, in: Franz T, Ed. Cardiovascular and cardiac therapeutic devices, Springer Berlin Heidelberg. 169-206.

Cleutjens JP, Verluyten MJ, Smiths JF, Daemen MJ (1995). Collagen remodeling after myocardial infarction in the rat heart. Am J Pathol **147**(2): 325-38.

Cleutjens JPM, Blankesteijn WM, Daemen MJAP, Smits JFM (1999). The infarcted myocardium: Simply dead tissue, or a lively target for therapeutic interventions. Cardiovasc Res **44**(2): 232-41.

Costa KD, Holmes JW, McCulloch AD (2001). Modelling cardiac mechanical properties in three dimensions. Royal Society of London Philosophical Transactions Series A **359**: 1233-50.

Costa KD, Hunter PJ, Wayne JS, Waldman LK, Guccione JM, McCulloch AD (1996). A three-dimensional finite element method for large elastic deformations of ventricular myocardium: Ii--prolate spheroidal coordinates. J Biomech Eng **118**(4): 464-72.

Crowley J (1997). A quantitative description of dynamic left ventricular geometry in anaesthetized rats using magnetic resonance imaging. Exp Physiol **82**(5): 887-904.

Dai W, Wold LE, Dow JS, Kloner RA (2005). Thickening of the infarcted wall by collagen injection improves left ventricular function in rats: A novel approach to preserve cardiac function after myocardial infarction. J Am Coll Cardiol **46**(4): 714-9.

Delhaas T, Kroon W, Decaluwe W, Rubbens M, Bovendeerd P, Arts T (2008). Structure and torsion of the normal and situs inversus totalis cardiac left ventricle. I. Experimental data in humans. Am J Physiol Heart Circ Physiol **295**(1): H197-201.

Demer LL, Yin FC (1983). Passive biaxial mechanical properties of isolated canine myocardium. The Journal of Physiology **339**(1): 615-30.

Dobner S, Bezuidenhout D, Govender P, Zilla P, Davies N (2009). A synthetic non-degradable polyethylene glycol hydrogel retards adverse post-infarct left ventricular remodeling. J Card Fail **15**(7): 629-36.

Dorri F, Niederer PF, Lunkenheimer PP (2006). A finite element model of the human left ventricular systole. Comput Methods Biomech Biomed Eng **9**(5): 319 - 41.

Fishbein MC, Maclean D, Maroko PR (1978). Experimental myocardial infarction in the rat. Qualitative and quantitative changes during pathologic evolution. Am J Pathol **90**(1): 57-70.

Fishbein MC, Meerbaum S, Rit J, Lando U, Kanmatsuse K, Mercier JC, Corday E, Ganz W (1981). Early phase acute myocardial infarct size quantification: Validation of the triphenyl tetrazolium chloride tissue enzyme staining technique. Am Heart J **101**(5): 593-600.

FitzHugh R (1961). Impulses and physiological states in theoretical models of nerve membrane. Biophys J **1**(6): 445-66.

Fomovsky GM, Holmes JW (2010). Evolution of scar structure, mechanics, and ventricular function after myocardial infarction in the rat. Am J Physiol Heart Circ Physiol **298**(1): H221-H8.

Fomovsky GM, Rouillard AD, Holmes JW (2012). Regional mechanics determine collagen fiber structure in healing myocardial infarcts. J Mol Cell Cardiol **52**(5): 1083-90.

Fomovsky GM, Thomopoulos S, Holmes JW (2010). Contribution of extracellular matrix to the mechanical properties of the heart. J Mol Cell Cardiol **48**(3): 490-6.

Frank O (1899). Die grundform des arteriellen pulses erste abhandlung: Mathematische analyse. Z Biol **37**: 483-526.

Fuchs S, Baffour R, Zhou YF, Shou M, Pierre A, Tio FO, Weissman NJ, Leon MB, Epstein SE, Kornowski R (2001). Transendocardial delivery of autologous bone marrow enhances collateral perfusion and regional function in pigs with chronic experimental myocardial ischemia. J Am Coll Cardiol **37**(6): 1726-32.

Fung YC (1993). Biomechanics: Mechanical properties of living tissues. New York, Springer.

Fung YC, Fronek K, Patitucci P (1979). Pseudoelasticity of arteries and the choice of its mathematical expression. Am J Physiol **237**(5): H620-H31.

Fuster V, Walsh RA, Harington RA (2011). Hurst's the heart, McGraw-Hill.

Gallagher KP, Gerren RA, Stirling MC, Choy M, Dysko RC, McManimon SP, Dunham WR (1986). The distribution of functional impairment across the lateral border of acutely ischemic myocardium. Circ Res **58**(4): 570-83.

Gaudette GR, Cohen IS (2006). Cardiac regeneration: Materials can improve the passive properties of myocardium, but cell therapy must do more. Circulation **114**(24): 2575-7.

Geselowitz DB, Miller WT, 3rd (1983). A bidomain model for anisotropic cardiac muscle. Ann Biomed Eng **11**(3-4): 191-206.

Ghaemi H, Behdinan K, Spence AD (2009). In vitro technique in estimation of passive mechanical properties of bovine heart: Part i. Experimental techniques and data. Med Eng Phys **31**(1): 76-82.

Gilbert TW, Wognum S, Joyce EM, Freytes DO, Sacks MS, Badylak SF (2008). Collagen fiber alignment and biaxial mechanical behavior of porcine urinary bladder derived extracellular matrix. Biomaterials **29**(36): 4775-82.

Goldman S, Raya TE (1995). Rat infarct model of myocardial infarction and heart failure. J Card Fail **1**(2): 169-77.

Grashow JS, Yoganathan AP, Sacks MS (2006). Biaixal stress-stretch behavior of the mitral valve anterior leaflet at physiologic strain rates. Ann Biomed Eng **34**(2): 315-25.

Grosberg A, Gharib M, Kheradvar A (2009). Effect of fiber geometry on pulsatile pumping and energy expenditure. Bull Math Biol **71**(7): 1580-98.

Grossman W, Jones D, McLaurin LP (1975). Wall stress and patterns of hypertrophy in the human left ventricle. J Clin Invest **56**(1): 56-64.

Guccione JM, Costa KD, McCulloch AD (1995). Finite element stress analysis of left ventricular mechanics in the beating dog heart. J Biomech **28**(10): 1167-77.

Guccione JM, McCulloch AD, Waldman LK (1991). Passive material properties of intact ventricular myocardium determined from a cylindrical model. J Biomech Eng **113**(1): 42-55.

Guccione JM, Moonly SM, Moustakidis P, Costa KD, Moulton MJ, Ratcliffe MB, Pasque MK (2001). Mechanism underlying mechanical dysfunction in the border zone of left ventricular aneurysm: A finite element model study. The Annals of Thoracic Surgery **71**(2): 654-62.

Gundiah N, Chang D, Zhang P, Ratcliffe M, Pruitt L (2004). Structural and mechanical characteristics of healing myocardial scar tissue. ASME International Mechanical Engineering Congress and Exposition. Anaheim, CA, USA**:** 265-6.

Gupta KB, Ratcliffe MB, Fallert MA, Edmunds LH, Jr., Bogen DK (1994). Changes in passive mechanical stiffness of myocardial tissue with aneurysm formation. Circulation **89**(5): 2315-26.

Guyton AC, Hall JE (2006). Textbook of medical physiology. Philadelphia, Elsevier Saunders.

Hautemann DJ (2007). Fiber architecture of the post-mortem rat heart obtained with difusion tensor imaging. Department of Biomedical Engineering. Eindhoven, Eindhoven University of Technology. **MSc**.

Healy SN, McCulloch AD (2005). An ionic model of stretch-activated and stretch-modulated currents in rabbit ventricular myocytes. Europace **7 Suppl 2**: 128-34.

Heiberg E, Sjogren J, Ugander M, Carlsson M, Engblom H, Arheden H (2010). Design and validation of segment - freely available software for cardiovascular image analysis. BMC Medical Imaging **10**(1): 1-13.

Henriquez CS (1993). Simulating the electrical behavior of cardiac tissue using the bidomain model. Crit Rev Biomed Eng **21**(1): 1-77.

Hill MR, Raut SS, Rodriguez A, Weber TV, Chen D, Placeres C, Cheang D, Sacks MS (2014). Triaxial experimental analysis and simulation (texas) system for full 3d modeling of soft biological tissues 7th World Congress of Biomechanics. Boston, MA.

Hochman JS, Bulkley BH (1982). Pathogenesis of left ventricular aneurysms: An experimental study in the rat model. Am J Cardiol **50**(1): 83-8.

Hodgkin A, Huxley A (1990). A quantitative description of membrane current and its application to conduction and excitation in nerve. Bull Math Biol **52**(1): 25-71.

Hodgkin AL, Huxley AF (1952). A quantitative description of membrane current and its application to conduction and excitation in nerve. The Journal of Physiology **117**(4): 500-44.

Hoffman AH, Grigg P (1984). A method for measuring strains in soft tissue. J Biomech **17**(10): 795-800.

Holmes JW (2004). Candidate mechanical stimuli for hypertrophy during volume overload. J Appl Physiol **97**(4): 1453-60.

Holmes JW, Borg TK, Covell JW (2005). Structure and mechanics of healing myocardial infarcts. Annu Rev Biomed Eng **7**: 223-53.

Holmes JW, Nunez JA, Covell JW (1997). Functional implications of myocardial scar structure. Am J Physiol **272**(5 Pt 2): H2123-30.

Holzapfel GA, Ogden RW (2009). Constitutive modelling of passive myocardium: A structurally based framework for material characterization. Philosophical Transactions of the Royal Society a-Mathematical Physical and Engineering Sciences **367**(1902): 3445-75.

Huang NF, Sievers RE, Park JS, Fang Q, Li S, Lee RJ (2006). A rodent model of myocardial infarction for testing the efficacy of cells and polymers for myocardial reconstruction. Nat Protoc **1**: 1596-609.

Humphrey JD (1995). Mechanics of the arterial wall: Review and directions. Crit Rev Biomed Eng **23**(1-2): 1-162.

Humphrey JD, Strumpf RK, Yin FC (1990a). Determination of a constitutive relation for passive myocardium: I. A new functional form. J Biomech Eng **112**(3): 333-9.

Humphrey JD, Strumpf RK, Yin FCP (1990b). Determination of a constitutive relation for passive myocardium: Ii.--- parameter estimation. J Biomech Eng **112**: 340-6.

Humphrey JD, Vawter DL, Vito RP (1987). Quantification of strains in biaxially tested soft tissues. J Biomech **20**(1): 59-65.

Hunter PJ, McCulloch AD, ter Keurs HE (1998). Modelling the mechanical properties of cardiac muscle. Prog Biophys Mol Biol **69**(2-3): 289-331.

Hutchins GM, Bulkley BH (1978). Infarct expansion versus extension: Two different complications of acute myocardial infarction. Am J Cardiol **41**(7): 1127-32.

Ifkovits JL, Tous E, Minakawa M, Morita M, Robb JD, Koomalsingh KJ, Gorman JH, Gorman RC, Burdick JA (2010). Injectable hydrogel properties influence infarct expansion and extent of postinfarction left ventricular remodeling in an ovine model. Proceedings of the National Academy of Sciences **107**(25): 11507-12.

Jafri MS, Rice JJ, Winslow RL (1998). Cardiac ca2+ dynamics: The roles of ryanodine receptor adaptation and sarcoplasmic reticulum load. Biophys J **74**(3): 1149-68.

Janz RF, Waldron RJ (1978). Predicted effect of chronic apical aneurysms on the passive stiffness of the human left ventricle. Circ Res **42**(2): 255-63.

Jiang X-J, Wang T, Li X-Y, Wu D-Q, Zheng Z-B, Zhang J-F, Chen J-L, Peng B, Jiang H, Huang C, Zhang X-Z (2009). Injection of a novel synthetic hydrogel preserves left ventricle function after myocardial infarction. J Biomed Mater Res, Part A **90A**(2): 472-7.

Jugdutt BI, Amy RW (1986). Healing after myocardial infarction in the dog: Changes in infarct hydroxyproline and topography. J Am Coll Cardiol **7**(1): 91-102.

Jugdutt BI, Joljart MJ, Khan MI (1996). Rate of collagen deposition during healing and ventricular remodeling after myocardial infarction in rat and dog models. Circulation **94**(1): 94-101.

Kadner K, Dobner S, Franz T, Bezuidenhout D, Sirry MS, Zilla P, Davies NH (2012). The beneficial effects of deferred delivery on the efficiency of hydrogel therapy post myocardial infarction. Biomaterials **33**(7): 2060-6.

Kawamoto A, Tkebuchava T, Yamaguchi J, Nishimura H, Yoon YS, Milliken C, Uchida S, Masuo O, Iwaguro H, Ma H, Hanley A, Silver M, Kearney M, Losordo DW, Isner JM, Asahara T (2003). Intramyocardial transplantation of autologous endothelial progenitor cells for therapeutic neovascularization of myocardial ischemia. Circulation **107**(3): 461-8.

Kerckhoffs R, Neal M, Gu Q, Bassingthwaighte J, Omens J, McCulloch A (2007). Coupling of a 3d finite element model of cardiac ventricular mechanics to lumped systems models of the systemic and pulmonic circulation. Ann Biomed Eng **35**(1): 1-18.

Kerckhoffs RC, Faris OP, Bovendeerd PH, Prinzen FW, Smits K, McVeigh ER, Arts T (2003). Timing of depolarization and contraction in the paced canine left ventricle: Model and experiment. J Cardiovasc Electrophysiol **14**(10 Suppl): S188-95.

Kerckhoffs RCP, Healy SN, Usyk TP, McCulloch AD (2006). Computational methods for cardiac electromechanics. Proceedings of the IEEE **94**(4): 769-83.

Khalil A, Bouma B, Kaazempur Mofrad M (2006). A combined fem/genetic algorithm for vascular soft tissue elasticity estimation. Cardiovasc Eng **6**(3): 93-102.

Khalil PN, Siebeck M, Huss R, Pollhammer M, Khalil MN, Neuhof C, Fritz H (2006). Histochemical assessment of early myocardial infarction using 2,3,5-triphenyltetrazolium chloride in blood-perfused porcine hearts. J Pharmacol Toxicol Methods **54**(3): 307-12.

Kichula E, Wang H, Dorsey S, Szczesny S, Elliott D, Burdick J, Wenk J (2014). Experimental and computational investigation of altered mechanical properties in myocardium after hydrogel injection. Ann Biomed Eng **42**(7): 1546-56.

Klodell Jr CT, Aranda Jr JM, McGiffin DC, Rayburn BK, Sun B, Abraham WT, Pae Jr WE, Boehmer JP, Klein H, Huth C (2008). Worldwide surgical experience with the paracor heartnet cardiac restraint device. The Journal of Thoracic and Cardiovascular Surgery **135**(1): 188-95.

Kortsmit J, Davies NH, Miller R, Macadangdang JR, Zilla P, Franz T (2013). The effect of hydrogel injection on cardiac function and myocardial mechanics in a computational post-infarction model. Comput Methods Biomech Biomed Eng **16**(11): 1185-95.

Kortsmit J, Davies NH, Miller R, Zilla P, Franz T (2013b). Computational predictions of improved of wall mechanics and function of the infarcted left ventricle at early and late remodelling stages: Comparison of layered and bulk hydrogel injectates. Advances in Biomechanics and Applications: 41-55.

Kroon M, Holzapfel GA (2008). A new constitutive model for multi-layered collagenous tissues. J Biomech **41**(12): 2766-71.

Laird JD, Vellekoop HP (1977). The course of passive elasticity of myocardial tissue following experimental infarction in rabbits and its relation to mechanical dysfunction. Circ Res **41**(5): 715-21.

Landa N, Miller L, Feinberg MS, Holbova R, Shachar M, Freeman I, Cohen S, Leor J (2008). Effect of injectable alginate implant on cardiac remodeling and function after recent and old infarcts in rat. Circulation **117**(11): 1388-96.

Landesberg A, Markhasin VS, Beyar R, Sideman S (1996). Effect of cellular inhomogeneity on cardiac tissue mechanics based on intracellular control mechanisms. Am J Physiol **270**(3 Pt 2): H1101-14.

Landesberg A, Sideman S (1994a). Coupling calcium binding to troponin c and cross-bridge cycling in skinned cardiac cells. Am J Physiol **266**(3): H1260-H71.

Landesberg A, Sideman S (1994b). Mechanical regulation of cardiac muscle by coupling calcium kinetics with cross-bridge cycling: A dynamic model. Am J Physiol **267**(2): H779-H95.

Lassen JF, Botker HE, Terkelsen CJ (2013). Timely and optimal treatment of patients with stemi. Nat Rev Cardiol **10**(1): 41-8.

Lee LC, Wenk JF, Klepach D, Zhang Z, Saloner D, Wallace AW, Ge L, Ratcliffe MB, Guccione JM (2011). A novel method for quantifying in-vivo regional left ventricular myocardial contractility in the border zone of a myocardial infarction. J Biomech Eng **133**(9): 094506-5.

LeGrice I, Hunter P, Young A, Smaill B (2001). The architecture of the heart: A data-based model. Philosophical Transactions of the Royal Society A: Mathematical, Physical and Engineering Sciences **359**(1783): 1217-32.

Leon LJ, Horacek BM (1991). Computer model of excitation and recovery in the anisotropic myocardium. Iii. Arrhythmogenic conditions in the simplified left ventricle. J Electrocardiol **24**(1): 33-41.

Levick JR (2010). An introduction to cardiovascular physiology. UK, Hodder Arnold.

Lin DH, Yin FC (1998). A multiaxial constitutive law for mammalian left ventricular myocardium in steady-state barium contracture or tetanus. J Biomech Eng **120**(4): 504-17.

Liu J, Hu Q, Wang Z, Xu C, Wang X, Gong G, Mansoor A, Lee J, Hou M, Zeng L, Zhang JR, Jerosch-Herold M, Guo T, Bache RJ, Zhang J (2004). Autologous stem cell transplantation for myocardial repair. Am J Physiol **287**(2): H501-H11.

Liu Z, Kastis GA, Stevenson GD, Barrett HH, Furenlid LR, Kupinski MA, Patton DD, Wilson DW (2002). Quantitative analysis of acute myocardial infarct in rat hearts with ischemia-reperfusion using a high-resolution stationary spect system. J Nucl Med **43**(7): 933-9.

Lu W-N, Lèu S-H, Wang H-B, Li D-X, Duan C-M, Liu Z-Q, Hao T, He W-J, Xu B, Fu Q, Song YC, Xie X-H, Wang C-Y (2009). Functional improvement of infarcted heart by co-

injection of embryonic stem cells with temperature-responsive chitosan hydrogel. Tissue Engineering, Part A **15**(6): 1437-47.

Luo CH, Rudy Y (1994a). A dynamic model of the cardiac ventricular action potential. I. Simulations of ionic currents and concentration changes. Circ Res **74**(6): 1071-96.

Luo CH, Rudy Y (1994b). A dynamic model of the cardiac ventricular action potential. Ii. Afterdepolarizations, triggered activity, and potentiation. Circ Res **74**(6): 1097-113.

Lutolf MP, Hubbell JA (2005). Synthetic biomaterials as instructive extracellular microenvironments for morphogenesis in tissue engineering. Nat Biotechnol **23**(1): 47-55.

Mahmarian JJ, Moyé LA, Chinoy DA, Sequeira RF, Habib GB, Henry WJ, Jain A, Chaitman BR, Weng CSW, Morales-Ballejo H, Pratt CM (1998). Transdermal nitroglycerin patch therapy improves left ventricular function and prevents remodeling after acute myocardial infarction: Results of a multicenter prospective randomized, double-blind, placebo-controlled trial. Circulation **97**(20): 2017-24.

Mangi AA, Noiseux N, Kong D, He H, Rezvani M, Ingwall JS, Dzau VJ (2003). Mesenchymal stem cells modified with akt prevent remodeling and restore performance of infarcted hearts. Nat Med **9**(9): 1195-201.

Maroko PR, Kjekshus JK, Sobel BE, Watanabe T, Covell JW, Ross J, Jr., Braunwald E (1971). Factors influencing infarct size following experimental coronary artery occlusions. Circulation **43**(1): 67-82.

Mazhari R, McCulloch AD (2000). Integrative models for understanding the structural basis of regional mechanical dysfunction in ischemic myocardium. Ann Biomed Eng **28**(8): 979-90.

Mazhari R, Omens JH, Covell JW, McCulloch AD (2000). Structural basis of regional dysfunction in acutely ischemic myocardium. Cardiovasc Res **47**(2): 284-93.

Mazhari R, Omens JH, Waldman LK, McCulloch AD (1998). Regional myocardial perfusion and mechanics: A model-based method of analysis. Ann Biomed Eng **26**(5): 743-55.

McCulloch AD (2005). Cardiac biomechanics, in: Bronzino JD, Ed. The biomedical engineering handbook. Boca Raton, FL, CRC Press. 54-1 to -27.

McCulloch AD, Paternostro G (2005). Cardiac systems biology. Ann N Y Acad Sci **1047**: 283-95.

McMurray JJ, Pfeffer MA (2005). Heart failure. Lancet **365**(9474): 1877-89.

Miller R (2012). A computational study of post-infarct mechanical effects of injected biomaterial into ischaemic myocardium, University of Cape Town. **MSc**.

Miller R, Davies NH, Kortsmit J, Zilla P, Franz T (2013). Outcomes of myocardial infarction hydrogel injection therapy in the human left ventricle dependent on injectate distribution. Int J Numer Meth Bio **29**(8): 870-84.

Mirotsou M, Zhang Z, Deb A, Zhang L, Gnecchi M, Noiseux N, Mu H, Pachori A, Dzau V (2007). Secreted frizzled related protein 2 (sfrp2) is the key akt-mesenchymal stem cell-released paracrine factor mediating myocardial survival and repair. Proceedings of the National Academy of Sciences **104**(5): 1643-8.

Morita M, Eckert CE, Matsuzaki K, Noma M, Ryan LP, Burdick JA, Jackson BM, Gorman Iii JH, Sacks MS, Gorman RC (2011). Modification of infarct material properties limits adverse ventricular remodeling. The Annals of Thoracic Surgery **92**(2): 617-24.

Moses KP, Banks JC, Nava PB, Petersen D (2005). Atlas of clinical gross anatomy. Edinburgh, Elsevier Mosby.

Moustakidis P, Maniar HS, Cupps BP, Absi T, Zheng J, Guccione JM, Sundt TM, Pasque MK (2002). Altered left ventricular geometry changes the border zone temporal distribution of stress in an experimental model of left ventricular aneurysm: A finite element model study. Circulation **106**(13 Supplement): I-168-75.

Nagumo J, Arimoto S, Yoshizawa S (1962). An active pulse transmission line simulating nerve axon. Proceedings of the IRE **50**(10): 2061-70.

Nelson DM, Ma Z, Fujimoto KL, Hashizume R, Wagner WR (2011). Intra-myocardial biomaterial injection therapy in the treatment of heart failure: Materials, outcomes and challenges. Acta Biomater **7**(1): 1-15.

Nevo E, Lanir Y (1989). Structural finite deformation model of the left ventricle during diastole and systole. J Biomech Eng **111**(4): 342-9.

Nielsen PM, Le Grice IJ, Smaill BH, Hunter PJ (1991). Mathematical model of geometry and fibrous structure of the heart. Am J Physiol **260**(4 Pt 2): H1365-78.

Noble D, Rudy Y (2001). Models of cardiac ventricular action potentials: Iterative interaction between experiment and simulation. Philosophical Transactions of the Royal Society A: Mathematical, Physical and Engineering Sciences **359**(1783): 1127-42.

Novak VP, Yin FCP, Humphrey JD (1994). Regional mechanical properties of passive myocardium. J Biomech **27**(4): 403-12.

Omens J, May K, McCulloch A (1991). Transmural distribution of three-dimensional strain in the isolated arrested canine left ventricle. Am J Physiol Heart Circ Physiol **261**(3): H918.

Omens JH, MacKenna DA, McCulloch AD (1993). Measurement of strain and analysis of stress in resting rat left ventricular myocardium. J Biomech **26**(6): 665-76.

Page DL, Caulfield JB, Kastor JA, DeSanctis RW, Sanders CA (1971). Myocardial changes associated with cardiogenic shock. N Engl J Med **285**(3): 133-7.

Pandit SV, Clark RB, Giles WR, Demir SS (2001). A mathematical model of action potential heterogeneity in adult rat left ventricular myocytes. Biophys J **81**(6): 3029-51.

Panerai RB (1980). A model of cardiac muscle mechanics and energetics. J Biomech **13**(11): 929-40.

Pao YC, Ritman EL (1998). Comparative characterization of the infarcted and reperfused ventricular wall muscles by finite element analysis and a myocardial muscle-blood composite model. Comput Biomed Res **31**(1): 18-31.

Park SW, Lee SY, Park SJ, Lee S-C, Gwon H-C, Kim D-K (2004). Quantitative assessment of infarct size in vivo by myocardial contrast echocardiography in a murine acute myocardial infarction model. Int J Cardiol **97**(3): 393-8.

Pérez de Prado A, Cuellas-Ramón C, Regueiro-Purriños M, Gonzalo-Orden JM, Pérez-Martínez C, Altónaga JR, García-Iglesias MJ, Orden-Recio MA, García-Marín JF, Fernández-Vázquez F (2009). Closed-chest experimental porcine model of acute myocardial infarction-reperfusion. J Pharmacol Toxicol Methods **60**(3): 301-6.

Pfeffer JM (1991). Progressive ventricular dilation in experimental myocardial infarction and its attenuation by angiotensin-converting enzyme inhibition. The American Journal of Cardiology **68**(14): 17-25.

Pfeffer JM, Pfeffer MA, Fletcher PJ, Braunwald E (1991). Progressive ventricular remodeling in rat with myocardial infarction. Am J Physiol **260**(5 Pt 2): H1406-14.

Pfeffer MA, Braunwald E (1990). Ventricular remodeling after myocardial infarction. Experimental observations and clinical implications. Circulation **81**(4): 1161-72.

Pfeffer MA, Pfeffer JM, Fishbein MC, Fletcher PJ, Spadaro J, Kloner RA, Braunwald E (1979). Myocardial infarct size and ventricular function in rats. Circ Res **44**(4): 503-12.

Phelp B (2012). Identification of the material properties of hydrogel by an inverse method, University of Cape Town. **BSc**.

Piot CA, Padmanaban D, Ursell PC, Sievers RE, Wolfe CL (1997). Ischemic preconditioning decreases apoptosis in rat hearts in vivo. Circulation **96**(5): 1598-604.

Raman J (2008). Management of heart failure. New York, Springer.

Rane AA, Christman KL (2011). Biomaterials for the treatment of myocardial infarction: A 5-year update. J Am Coll Cardiol **58**(25): 2615-29.

Roberts CS, Maclean D, Braunwald E, Maroko PR, Kloner RA (1983). Topographic changes in the left ventricle after experimentally induced myocardial infarction in the rat. Am J Cardiol **51**(5): 872-6.

Rodriguez B, Tice BM, Eason JC, Aguel F, Trayanova N (2004). Cardiac vulnerability to electric shocks during phase 1a of acute global ischemia. Heart Rhythm **1**(6): 695-703.

Rosamond W, Flegal K, Furie K, Go A, Greenlund K, Haase N, Hailpern SM, Ho M, Howard V, Kissela B, Kittner S, Lloyd-Jones D, McDermott M, Meigs J, Moy C, Nichol G, O'Donnell C, Roger V, Sorlie P, Steinberger J, Thom T, Wilson M, Hong Y (2008). Heart disease and stroke statistics--2008 update: A report from the american heart association statistics committee and stroke statistics subcommittee. Circulation **117**(4): e25-146.

Rosolen AM, Ordas S, Vazquez M, Frangi AF (2006). Numerical schemes for the simulation of three-dimensional cardiac electrical propagation in patient-specific ventricular geometries. European Conference on Computational Fluid Dynamics ECCOMAS CFD 2006. Wesseling P, Onate E, Periaux J.

Ruvinov E, Leor J, Cohen S (2011). The promotion of myocardial repair by the sequential delivery of igf-1 and hgf from an injectable alginate biomaterial in a model of acute myocardial infarction. Biomaterials **32**(2): 565-78.

Saavedra WF, Tunin RS, Paolocci N, Mishima T, Suzuki G, Emala CW, Chaudhry PA, Anagnostopoulos P, Gupta RC, Sabbah HN, Kass DA (2002). Reverse remodeling and enhancedadrenergic reserve from passive externalsupport in experimental dilated heart failure. J Am Coll Cardiol **39**(12): 2069-76.

Sacks M (2000). Biaxial mechanical evaluation of planar biological materials. J Elasticity **61**(1): 199-246.

Sacks M, Chuong CJ (1998). Orthotropic mechanical properties of chemically treated bovine pericardium. Ann Biomed Eng **26**(5): 892-902.

Sacks MS, Chuong CJ (1993a). A constitutive relation for passive right-ventricular free wall myocardium. J Biomech **26**(11): 1341-5.

Sacks MS, Chuong CJ (1993b). Biaxial mechanical properties of passive right ventricular free wall myocardium. J Biomech Eng **115**(2): 202-5.

Saleh M, Sharp S-K, Alhamud A, Spottiswoode BS, van der Kouwe AJW, Davies NH, Franz T, Meintjes EM (2012). Long-term left ventricular remodelling in rat model of non-reperfused myocardial infarction: Sequential mr imaging using a 3t clinical scanner. Journal of Biomedicine and Biotechnology **2012**: :10.

Schmid, Niederer, Lunkenheimer, Torrent G (1997). The anisotropic structure of the human left and right ventricles. Technol Health Care **5**(1/2): 29.

Schmitz HJ, Erbel R, Meyer J, von Essen R (1996). Influence of vessel dilatation on restenosis after successful percutaneous transluminal coronary angioplasty. Am Heart J **131**(5): 884-91.

Simpleware (2014). Reference Guide Exeter, UK, Simpleware Ltd.

Singelyn JM, Christman KL (2011). Injectable materials for myocardial tissue engineering, in: Boccaccini AR, Harding SE, Eds. Myocardial tissue engineering. Berlin Heidelberg, Springer. 133-63.

Smith M, Russell RO, Jr., Feild BJ, Rackley CE (1974). Left ventricular compliance and abnormally contracting segments in postmyocardial infarction patients. Chest **65**(4): 368-78.

Stergiopulos N, Westerhof BE, Westerhof N (1999). Total arterial inertance as the fourth element of the windkessel model. Am J Physiol **276**(1 Pt 2): H81-8.

Steyn K, Sliwa K, Hawken S, Commerford P, Onen C, Damasceno A, Ounpuu S, Yusuf S, for the INTERHEART Investigators in Africa (2005). Risk factors associated with myocardial infarction in africa: The interheart africa study. Circulation **112**(23): 3554-61.

Strauer BE, Brehm M, Zeus T, Kostering M, Hernandez A, Sorg RV, Kogler G, Wernet P (2002). Repair of infarcted myocardium by autologous intracoronary mononuclear bone marrow cell transplantation in humans. Circulation **106**(15): 1913-8.

Struck E, Hagl S, Meisner H, Sebening F (1985). Heart transplantation: Limitations and perspectives. Z Kardiol **74 Suppl 6**: 59-63.

Suga H (1990). Energetics of the time-varying elastance model, a visco-elastic model, matches mommaerts' unifying concept of the fenn effect of muscle. Jpn Heart J **31**(3): 341-53.

Suga H, Sagawa K, Shoukas AA (1973). Load independence of the instantaneous pressure-volume ratio of the canine left ventricle and effects of epinephrine and heart rate on the ratio. Circ Res **32**(3): 314-22.

Sun K, Stander N, Jhun C-S, Zhang Z, Suzuki T, Wang G-Y, Saeed M, Wallace AW, Tseng EE, Baker AJ, Saloner D, Einstein DR, Ratcliffe MB, Guccione JM (2009). A computationally efficient formal optimization of regional myocardial contractility in a sheep with left ventricular aneurysm. J Biomech Eng **131**(11): 111001.

Sun W, Sacks MS (2005). Finite element implementation of a generalized fung-elastic constitutive model for planar soft tissues. Biomech Model Mechanobiol **4**(2-3): 190-9.

Sun W, Sacks MS, Scott MJ (2005). Effects of boundary conditions on the estimation of the planar biaxial mechanical properties of soft tissues. J Biomech Eng **127**(4): 709-15.

Taber LA (1991). On a nonlinear theory for muscle shells: Part ii--application to the beating left ventricle. J Biomech Eng **113**(1): 63-71.

Takagawa J, Zhang Y, Wong ML, Sievers RE, Kapasi NK, Wang Y, Yeghiazarians Y, Lee RJ, Grossman W, Springer ML (2007). Myocardial infarct size measurement in the mouse chronic infarction model: Comparison of area- and length-based approaches.

ten Tusscher KH, Noble D, Noble PJ, Panfilov AV (2004). A model for human ventricular tissue. Am J Physiol Heart Circ Physiol **286**(4): H1573-89.

Tendulkar AP, Harken AH (2006). Mechanics of the normal heart. J Card Surg **21**(6): 615-20.

Tomita S, Mickle DA, Weisel RD, Jia ZQ, Tumiati LC, Allidina Y, Liu P, Li RK (2002). Improved heart function with myogenesis and angiogenesis after autologous porcine bone marrow stromal cell transplantation. J Thorac Cardiovasc Surg **123**(6): 1132-40.

Trew M, Le Grice I, Smaill B, Pullan A (2005). A finite volume method for modeling discontinuous electrical activation in cardiac tissue. Ann Biomed Eng **33**(5): 590-602.

Turner GO (2008). Recognizing and surviving heart attacks and strokes. Columbia and London, Univsersity of Missouri Press.

Uemura R, Xu M, Ahmad N, Ashraf M (2006). Bone marrow stem cells prevent left ventricular remodeling of ischemic heart through paracrine signaling. Circ Res **98**(11): 1414-21.

Usyk TP, LeGrice IJ, McCulloch AD (2002). Computational model of three-dimensional cardiac electromechanics. Computing and Visualization in Science **4**(4): 249-57.

Usyk TP, Mazhari R, McCulloch AD (2000). Effect of laminar orthotropic myofiber architecture on regional stress and strain in the canine left ventricle. J Elasticity **61**(1-3): 143-64.

Usyk TP, McCulloch AD (2003). Computational methods for soft tissue biomechanics., in: Holzapfel GA, Ogden RW, Eds. Biomechanics of soft tissue in cardiovascular systems. Wien, Springer. 273-342.

Usyk TP, Omens JH, McCulloch AD (2001). Regional septal dysfunction in a three-dimensional computational model of focal myofiber disarray. Am J Physiol Heart Circ Physiol **281**(2): H506-14.

van Capelle FJ, Durrer D (1980). Computer simulation of arrhythmias in a network of coupled excitable elements. Circ Res **47**(3): 454-66.

Van De Graaff KM (2001). Human anatomy. Boston, McGraw-Hill.

Vetter FJ, McCulloch AD (1998). Three-dimensional analysis of regional cardiac function: A model of rabbit ventricular anatomy. Prog Biophys Mol Biol **69**(2-3): 157-83.

Vetter FJ, McCulloch AD (2000). Three-dimensional stress and strain in passive rabbit left ventricle: A model study. Ann Biomed Eng **28**(7): 781-92.

Viswanathan PC, Rudy Y (1999). Pause induced early afterdepolarizations in the long qt syndrome: A simulation study. Cardiovasc Res **42**(2): 530-42.

Vivaldi MT, Eyre DR, Kloner RA, Schoen FJ (1987). Effects of methylprednisolone on collagen biosynthesis in healing acute myocardial infarction. The American Journal of Cardiology **60**(4): 424-5.

Vracko R, Thorning D, Frederickson RG (1989). Connective tissue cells in healing rat myocardium. A study of cell reactions in rhythmically contracting environment. Am J Pathol **134**(5): 993-1006.

Walker JC, Ratcliffe MB, Zhang P, Wallace AW, Fata B, Hsu EW, Saloner D, Guccione JM (2005). Mri-based finite-element analysis of left ventricular aneurysm. Am J Physiol Heart Circ Physiol **289**(2): H692-700.

Wall ST, Walker JC, Healy KE, Ratcliffe MB, Guccione JM (2006). Theoretical impact of the injection of material into the myocardium - a finite element model simulation. Circulation **114**(24): 2627-35.

Wang C, Garcia M, Lu X, Lanir Y, Kassab GS (2006). Three-dimensional mechanical properties of porcine coronary arteries: A validated two-layer model.

Watanabe H, Sugiura S, Kafuku H, Hisada T (2004). Multiphysics simulation of left ventricular filling dynamics using fluid-structure interaction finite element method. Biophys J **87**(3): 2074-85.

Weaver W, Cerqueira M, Hallstrom AP, et al. (1993). Prehospital-initiated vs hospital-initiated thrombolytic therapy: The myocardial infarction triage and intervention trial. JAMA **270**(10): 1211-6.

Wehrens XH, Doevendans PA (2004). Cardiac rupture complicating myocardial infarction. Int J Cardiol **95**(2-3): 285-92.

Weisman HF, Healy B (1987). Myocardial infarct expansion, infarct extension, and reinfarction: Pathophysiologic concepts. Prog Cardiovasc Dis **30**(2): 73-110.

Wenk JF, Eslami P, Zhang Z, Xu C, Kuhl E, Gorman Iii JH, Robb JD, Ratcliffe MB, Gorman RC, Guccione JM (2011b). A novel method for quantifying the in-vivo mechanical effect of material injected into a myocardial infarction. The Annals of Thoracic Surgery **92**(3): 935-41.

Wenk JF, Klepach D, Lee LC, Zhang Z, Ge L, Tseng EE, Martin A, Kozerke S, Gorman Iii JH, Gorman RC, Guccione JM (2012). First evidence of depressed contractility in the border zone of a human myocardial infarction. The Annals of Thoracic Surgery **93**(4): 1188-93.

Wenk JF, Sun K, Zhang Z, Soleimani M, Ge L, Saloner D, Wallace AW, Ratcliffe MB, Guccione JM (2011a). Regional left ventricular myocardial contractility and stress in a finite element model of posterobasal myocardial infarction. J Biomech Eng **133**(4): 044501.

Wenk JF, Wall ST, Peterson RC, Helgerson SL, Sabbah HN, Burger M, Stander N, Ratcliffe MB, Guccione JM (2009). A method for automatically optimizing medical devices for treating heart failure: Designing polymeric injection patterns. J Biomech Eng **131**(12): 121011.

Westerhof N, Elzinga G, van den Bos GC (1973). Influence of central and peripheral changes on the hydraulic input impedance of the systemic arterial tree. Med Biol Eng **11**(6): 710-23.

Wise P (2013). Optimization of the hydrogel injectate therapy used in the treatment of myocardial infarction, University of Cape Town. **MSc**.

Wise RG, Huang CL, Al-Shafei AI, Carpenter TA, Hall LD (1999). Geometrical models of left ventricular contraction from mri of the normal and spontaneously hypertensive rat heart. Phys Med Biol **44**(10): 2657-76.

Yeoman MS (2004). The design and optimisation of fabric reinforced porous prosthetic grafts using finite element methods and genetic algorithms. Cardiovascular Research Unit. Cape Town, University of Cape Town. **PhD:** 258.

Yeoman MS, Reddy BD, Bowles HC, Zilla P, Bezuidenhout D, Franz T (2009). The use of finite element methods and genetic algorithms in search of an optimal fabric reinforced porous graft system. Ann Biomed Eng **37**(11): 2266-87.

Yin FCP, Chew PH, Zeger SL (1986). An approach to quantification of biaxial tissue stress-strain data. J Biomech **19**(1): 27-37.

Yin FCP, Strumpf RK, Chew PH, Zeger SL (1987). Quantification of the mechanical properties of noncontracting canine myocardium under simultaneous biaxial loading. J Biomech **20**(6): 577-89.

Zimmer H-G, Gerdes AM, Lortet S, Mall G (1990). Changes in heart function and cardiac cell size in rats with chronic myocardial infarction. J Mol Cell Cardiol **22**(11): 1231-43.

Zisch AH, Lutolf MP, Hubbell JA (2003). Biopolymeric delivery matrices for angiogenic growth factors. Cardiovasc Pathol **12**(6): 295-310.